

REPORT DOCUMENTATION PAGE			Form Approved OMB No. 0704-0188	
<p>Public reporting burden for this collection of information is estimated to average 1 hour per response, including the time for reviewing instructions, searching existing data sources, gathering and maintaining the data needed, and completing and reviewing the collection of information. Send comments regarding this burden estimate or any other aspect of this collection of information, including suggestions for reducing this burden, to Washington Headquarters Services, Directorate for Information Operations and Reports, 1215 Jefferson Davis Highway, Suite 1204, Arlington, VA 22202-4302, and to the Office of Management and Budget, Paperwork Reduction Project (0704-0188), Washington, DC 20503</p>				
1. AGENCY USE ONLY (Leave blank)	2. REPORT DATE 7 November 97	3. REPORT TYPE AND DATES COVERED Final Report		
4. TITLE AND SUBTITLE The Portability of Regional Seismic Discriminants Using Wavetrain Energy Ratios, and $m_b:M_0$ to Various Tectonic Regions		5. FUNDING NUMBERS Contract No.: F49620-94-C-0046		
6. AUTHOR(S) B.B. Woods C.K. Saikia		AFOSRTR 97-0659		
7. PERFORMING ORGANIZATION NAME(S) AND ADDRESS(ES) Woodward-Clyde Federal Services 566 El Dorado Street, Suite 100 Pasadena CA 91101-2560		8. PERFORMING ORGANIZATION REPORT NUMBER WCFS-F-97-01		
9. SPONSORING/MONITORING AGENCY NAME(S) AND ADDRESS(ES) Air Force Office of Scientific Research/PKC 110 Duncan Avenue, Suite B115 Bolling AFB DC 20332-8080 Technical Monitor: Dr. Stanley Dickinson		10. SPONSORING/MONITORING AGENCY REPORT NUMBER		
11. SUPPLEMENTARY NOTES				
12a. DISTRIBUTION/AVAILABILITY STATEMENT Approved for public release; distribution unlimited. DTIC QUALITY INSPECTED 2			12b. DISTRIBUTION CODE	
13. ABSTRACT (Maximum 200 words) We have examined broadband regional waveforms of recent (1988+) NTS underground explosions and earthquakes throughout the Southwestern U.S. and Baja, Mexico recorded by TERRAScope and other IRIS stations in order to characterize seismic sources for the purposes of event identification. We have developed several seismic discriminants based on our observations. The most promising discriminant is the ratio of short-period, vertical component, regional P-wave energy to long-period, three component, surface-wave energy (SP:LP). For this ratio explosions tend to have a higher value than do earthquakes. This discriminant works on the same premise as the difference between the teleseismic body-wave and surface-wave magnitude measurements for which earthquakes are richer in long-period surface-wave energy relative to explosions with the same body-wave magnitude. Another potential discriminant examined is the ratio of P-wave to S-wave energy in the short-period, vertical-component of regional seismograms (SP-P:S). We find that this criterion only yields marginal separation of the source populations but becomes more effective at higher frequency bands or when comparing observations from a single station. However, network-averaged values improve the performance as well. Using regional				
14. SUBJECT TERMS Discrimination Seismic Moment Regional Propagation Energy Ratios			15. NUMBER OF PAGES	
			16. PRICE CODE	
17. SECURITY CLASSIFICATION OF REPORT Unclassified	18. SECURITY CLASSIFICATION OF THIS PAGE Unclassified	19. SECURITY CLASSIFICATION OF ABSTRACT Unclassified	20. LIMITATION OF ABSTRACT	

Unclassified

SECURITY CLASSIFICATION OF THIS PAGE

CLASSIFIED BY:

DECLASSIFY ON:

13. Abstract (Continued)

stations for sources 200 to 1300 km away, the magnitude threshold for the SP:LP discriminant is roughly magnitude 4.0, the limiting factor being the signal level of the Airy phase, while that for the SP-P:S discriminant is roughly magnitude 3.0 for the same distance ranges. We investigate the portability of regional seismic discriminants, which were developed using this southwestern U.S. earthquake and NTS explosion data, by applying them to data from other geographic regions. Specifically, the U.S. PNE's GASBUGGY and RULISON, Semipalatinsk and Lop Nor test site explosions, earthquakes near these source regions, and earthquakes in Southwestern Asia comprise the data set for this study. Also, the discrimination criterion can be changed to peak amplitudes, making them applicable to historical analog records. We have taken this latter approach to the older (analog) data in this study. We find these discriminants do distinguish between earthquakes and underground nuclear explosions. In addition, we examine the portability of the difference between local magnitude and seismic moment, which has already been shown to separate NTS explosions from intra-regional earthquakes, to these other regions as well.

SECURITY CLASSIFICATION OF THIS PAGE

Unclassified

**THE PORTABILITY OF REGIONAL SEISMIC DISCRIMINANTS
USING WAVETRAIN ENERGY RATIOS, AND $m_b:M_0$ TO VARIOUS
TECTONIC REGIONS**

AFOSR CONTRACT NO. F49620-94-C-0046

**B.B. Woods
C.K. Saikia**

**Woodward-Clyde Federal Services
566 El Dorado Street, Suite 100
Pasadena CA 91101-2560**

7 Nov 1997

Final Report

Approved for public release; distribution unlimited

**AIR FORCE OFFICE OF SCIENTIFIC RESEARCH/PKC
110 DUNCAN AVENUE, SUITE B115
BOLLING AIR FORCE BASE DC 20332-8080**

19971203 242

PREFACE

This research was conducted under Contract F49620-94-C-0046, sponsored by Air Force Office of Scientific Research, Bolling AFB DC. The technical monitor was Dr. Stanley Dickinson.

The authors wish to thank the following persons who contributed to this work: H. K. Thio at the WCFS Pasadena Office for his assistance in data acquisition and production of maps, and D. V. Helmberger for his helpful discussions and reviews of the manuscript.

Table of Contents

1	Introduction.....	1
2	Regional Seismic Discriminants Using Wavetrain Energy Ratios.....	3
3	Application of the Regional Seismic Discriminants to the Colorado Plateau and Western Cordillera.....	27
4	Application of the Regional Seismic Discriminants to Central and Southwest Asia.....	38
5	Refinement of the Regional Short-period:Long-period Integrated Energy Ratio Discriminant with Results for Several Tectonic Regions.....	46
	References.....	51

1 Introduction

We are investigating the applicability and portability of regional seismic discriminants, which were developed using Southwestern United States earthquake and NTS explosion data (Woods and Helmberger, 1997), to events from other geographic, as well as tectonic, regions. The areas covered include the Colorado Plateau and Western Cordillera region, central Asia -- that is the region centered about the Semipalatinsk and Lop Nor test sites, and Southwest Asia -- centered about the Hindu-Kush region of Pakistan and extending westward into Iran and eastwards to the Lop Nor test site.

The discriminants being examined include the ratio of integrated short-period vertical component energy in the P and S wavetrains ($spP_z:spS_z$), and the ratio of integrated energy in the vertical component short-period P-wave to that of the long-period (predominantly surface wave) energy summed over the three components ($spP_z:lp_3$). These discriminants involve simple time-domain computations, making them attractive for operational monitoring purposes. Also the discrimination criterion can be changed to use peak amplitudes instead, making it applicable to historical analog records. We have taken this latter approach to the older (analog) data in this study.

The other discrimination criterion examined is regional $m_b:M_s$, which came out of previous work using $M_L:M_0$ (Woods *et al.*, 1993). This criterion has also been investigated by Patton and Walter (1993).

The $spP_z:lp_3$ and $m_b:M_s$ discriminants work on the same premises as teleseismic $m_b:M_s$, for which earthquakes are richer in long-period surface-wave energy relative to explosions with the same body-wave magnitude. The $spP_z:spS_z$ energy ratio is a variation of the short-period P:S discriminant (Evernden *et al.*, 1971).

Chapter 2 reviews the development of the energy ratio discriminants with the TERRAscope data. Some refinements to the methods are discussed and tested.

Chapter 3 examines these discriminants applied to events in the Colorado Plateau and the Western Cordillera. This region is the site of four U. S. peaceful nuclear explosions (PNE's) and a fair amount of natural seismicity. To study the PNE's requires using historical analog data which required modifying the energy ratios to peak amplitude estimates. This, in itself, is a worthwhile exercise to test the usefulness of such data, as for many regions of the world with sparse seismicity it will otherwise require some time -- say 20 years to record a sufficient number of events to calibrate these discriminants, with the current generation of digital seismometers that only in the past several years have begun to be deployed on a nearly world wide basis.

Chapter 4 examines the applicability of these discriminants to central and Southwest Asia. Here central Asia is defined as the region about the Semipalatinsk and Lop Nor test sites, and Southwest Asia extends southwest of there, through the Hindu-Kush Region and into Iran. Observations from the stations WMQ and GAR comprise most of the data for the central Asia energy-ratio discriminants, while the Southwest Asia data set consists of observations from the broadband stations NIL, AAK, and ABKT, and from KNET and PAKN array data. Although for some of these latter stations no observations of nuclear explosions are known to exist, the earthquake data can still be compared to those from other regions. The fact that the Hindu-Kush region has considerable deep seismicity, makes the earthquake data alone worthwhile to analyze in order to determine how these discriminants behave with respect to deep, mantle earthquakes.

Chapter 5 concerns the refinement of the $spP_z:lp_3$ (also called SP:LP) discriminant by incorporating a distance correction which provides a distant independent SP:LP measure that can be used to directly compare data from one region to another, as well as to events at disparate distances. This distance corrected log SP:LP energy ratio is essentially a regional equivalent to $m_b:M_s$. As the long-period signal measuring threshold is lower for regional observations than for teleseismic ones, this regional energy ratio can provide a $m_b:M_s$ -analog for events which would otherwise be too small, or too remote (with respect to receivers) to

measure M_s .

2 Regional Seismic Discriminants Using Wavetrain Energy Ratios

2.1 Introduction

Recent studies of regional seismic data (Woods *et al.*, 1993; Patton and Walter, 1993; and Taylor *et al.*, 1989) support teleseismic observations that explosive sources tend to be significantly richer in short-period (≈ 1 Hz) P-wave energy than earthquakes, relative to their long-period (0.05–0.167 Hz) surface wave energy, as manifested in the $m_b:M_s$ discriminant (Basham, 1969; Lieberman and Pomeroy, 1969; Marshall *et al.*, 1971; and Stevens and Day, 1985). Extending such short-period:long-period (SP:LP) measures to regional distances lowers the effective discrimination magnitude threshold, thus making this type of discriminant more useful.

From visual inspection of broadband displacement recordings of regional earthquakes and explosions, it is apparent that these two source types show distinctly different spectral content as is shown in Figure 1 which compares records from the Joint Verification Experiment KEARSARGE and the Lee Vining and Little Skull Mountain earthquakes. The three events, all recorded at Pasadena, California (PAS), are at roughly equal epicentral distances (KEARSARGE: 388 km, Little Skull Mtn: 321 km, Lee Vining: 442 km). Their locations are shown in the shaded inset in Figure 2. Source information is given for them in Table 1. The three-component averaged-ratio of peak short-period (WA) to long-period (PE) amplitude is 0.405 for the explosion. For the earthquakes it is lower, being 0.195 for Lee Vining and 0.0585 for Little Skull Mountain. This measurement reflects the relative strength of body wave to surface wave generation. Should the peak short-period amplitude be measured solely in the P-wavetrain window, this ratio would be lower still for earthquakes, thus separating them further from explosions. This feature is consistent with other observations that earthquakes tend to be long-period rich relative to explosions with similar short-period energy

levels.

There are a number of factors which contribute to this difference in waveform characteristics between earthquakes and explosions. This contrast can be explained, in part, by the differences in characteristic source-time functions and spatial source dimensions between earthquakes and explosions. Savino *et al.* (1971), Aki *et al.* (1974), and Müller (1973) find that explosions exhibit characteristics, in part, of an impulsive source and are, in any case, impulsive and compact sources relative to earthquakes (Walter *et al.*, 1995). Empirical explosion source models developed by Haskell (1967), and Mueller and Murphy (1971) yield source time functions with rise times which are only fractions of second in length. These source time functions are step-like in nature, with over-shoot giving the explosion source an impulse-like character. Aki (1967), Brune (1970) and Marshall (1970) find that earthquake source functions, on the other hand, are best-modeled as ramps or step-functions with combined duration and rise times greater than one second. Dreger and Helmberger (1991) found that even moderate-sized earthquakes ($M_L \approx 5.2$) have source durations greater than a second. Thus differences in the source processes and dimensions between earthquakes and explosions helps to explain the differences in their observed spectra.

Stevens and Day (1985) conclude from numerical modeling experiments that the difference between earthquake and explosion source spectra is only partially responsible for explaining $m_b:M_s$ observations, as at lower magnitudes ($m_b \leq 4.5$), the source spectral characteristics converge. They also cite focal mechanism, near-source elastic properties and pP interference effects as contributing factors to the separation of populations with this type of discriminant. The effect of earthquake focal mechanism upon the relative excitation of P-waves and surface waves can, of course, be significant, but it is also highly variable; in their study they found that the effect of earthquake focal mechanism on P-wave and Rayleigh wave amplitude does, on average, help to separate them from explosions, but that the scatter due to fault orientation is even larger. In a theoretical study of regional $m_b:M_s$, Lilwall (1988) found that earthquakes with a large dip-slip component do show some separation from explosions, but that strike-slip

events, on average, do not.

The two above studies found that the primary explanation for the difference in relative excitement of P-waves and Rayleigh waves between earthquakes and explosions is due to the low velocity source medium for explosions. Stevens and Day show that the difference between m_b - M_s of an explosion and earthquake involves the factors $(\rho_q \alpha_q^3 / \rho_x \alpha_x^3)^{1/2}$ and α_x^2 / β_x^2 , where the subscript q denotes earthquake and x denotes explosion. The effect of the first term can be considered a depth-related phenomenon, whereby shallow sources in low velocity material (usually explosions) generate relatively larger body-wave to surface-wave amplitude ratios than do deeper events. By their nature earthquakes tend to occur at greater depth in higher velocity material, thus yielding this contrast in apparent source characteristics. The second term implies that explosions detonated in high Poisson ratio material will have relatively larger m_b - M_s offsets as well.

An obvious phenomenon related to mechanism is the type of wave generated. Barring tectonic release and collapse, explosions do not directly generate shear waves or, at longer periods, Love waves. Hence explosions will generally be depleted in such energy relative to earthquakes, particularly small explosions ($m_b \leq 4.5$) which generally don't exhibit significant tectonic release. Earthquakes commonly have prominent Love waves down to $m_b = 3.5$, so in this respect (the SH wave field) small earthquake and explosion long-period source spectra are significantly different. Of course there will be exceptions to this for particular fault orientations and source-receiver geometries.

Spall effects may also be a cause of the observed short-period ($0.15 \text{ Hz} < f < 2.0 \text{ Hz}$) enrichment of explosion source spectra relative to that of earthquakes. Theoretical results (Day and McLaughlin, 1991) and various observational studies (Viecelli, 1973; Stump, 1985; and Taylor and Randall, 1989) conclude that spallation can be a significant contributor to short-period energy, while Day *et al.* (1983) and Patton (1988) find no appreciable spall energy at periods greater than 8 secs.

As with all body-wave/surface-wave discriminants the limiting measurement is that of the

surface-wave amplitude. Lieberman and Pomeroy (1969) found the surface-wave detection level for earthquakes to be $m_b > 4.3$ and for explosions to be $m_b > 4.8$ for far-regional distances ($d \geq 1000$ km), but found that the two populations converged below $m_b = 5.0$ for discrimination purposes. Below these threshold levels the teleseismic surface-wave signals are within the noise level and analogous discriminants using regional phases must be employed. Evernden *et al.* (1971), Lambert and Alexander (1971), and Peppin and McEvelly (1974) found that they could distinguish between earthquakes and explosions on the basis of the amplitude ratio of regional P_n to Airy-phase Rayleigh waves. The latter study found separation by source type for events down to magnitude (M_L) 3.6 for explosions and 3.3 for earthquakes. Taylor *et al.* (1989) found similar long-period measurement threshold levels ($m_{b(Pn)} > 3.8$ for explosions and $m_{b(Pn)} > 3.3$ for earthquakes) in this region. The Western U.S. is known to be a region of low Q (Patton and Taylor, 1984). It is expected that regions with high Q will have lower magnitude thresholds for measuring surface waves.

Woods *et al.* (1993) employed local magnitude (M_L) and seismic moment (M_0) as regional analogs to m_b and M_s measurements, respectively, and found that explosion and earthquake populations separate at all observed magnitude ranges. Patton and Walter (1993) obtained similar results using $m_{b(Pn)}$ as the short-period measurement and M_0 as the long-period measurement. Moment tensor estimates, however, require reasonably accurate Green's functions (Zhao and Helmberger, 1994; Thio and Kanamori, 1995). At low magnitudes, moment estimates are susceptible to noise effects, although this problem can be minimized using phase-matched filtering (Herrin and Goforth, 1977). Such moment calculating procedures are, however, fairly involved and would be difficult to implement for an automated monitoring system. Moment tensor solutions assume an {*a priori*} source type (double-couple or isotropic source) which make it a less than ideal discrimination parameter. Stevens and McLaughlin (1988) approached this problem by treating all events as explosions, however the events did not separate by source type below $m_b = 5$, and explosions below this magnitude did not have observable surface waves and maximum likely-hood moments were

determined for them from their noise level. Even simple low-frequency spectral level methods (Vidal and Munguia, 1991) require estimates of source media properties for accurate moment calculations and unless there are multiple observations at different azimuths, radiation pattern effects won't be adequately accounted for.

Taylor *et al.* (1989) investigated a number of regional discriminants involving long-period measurements: m_b vs. M_s and m_b vs. long-period surface wave energy density and found both to be effective at separating explosions from earthquakes. However, these methods still require path calibration and the energy density method used is even more susceptible to signal to noise level thresholds than peak amplitudes or magnitude ratio measurements.

In this paper we use a more empirical approach to the SP:LP discrimination problem. As such it avoids the problems noted above for moment calculation techniques, in that it requires no waveform modeling and all events are processed in the same fashion. The analysis is simple and performed in the time-domain, so that it would be very easy to implement operationally. Further, unlike other methods discussed, this one utilizes all three long-period components, so that the long-period measurements are less susceptible to radiation pattern effects, *i.e.* should an observation for an earthquake be at a Rayleigh wave node, there should still be appreciable Love wave signal. Also, as mentioned before, incorporating Love wave measurements should enhance the contrast in waveform spectral content between earthquakes and explosions because of the fundamental difference in source radiation, *i.e.* explosions do not generate Love waves unless accompanied by tectonic release.

The $E_{spPz}:E_{spSz}$ ratio, the other discrimination criterion studied, is essentially a measure of P/Lg, a review of which is given in Pomeroy *et al.* (1980). On the basis of previous work they strongly suggest that the ratio of P to Lg is not a reliable discriminant, although explosions generally do have higher values than do earthquakes. Murphy and Bennett (1982) come to the same conclusion using amplitude ratios and a data set consisting of NTS explosions and nearby earthquakes recorded at TFO. However, they only address smaller explosions, thus limiting their data set to Rainier and Yucca shots, for which strong near-

source scattering can complicate the spectra of phases of interest as is discussed later in this paper.

With the advent of broadband digital stations coming online in the late 80's, a new series of studies have been conducted. In their study of various regional discriminants applied to LLNL data, Taylor *et al.* (1989) found that network-averaged values of peak P/Lg ratios yielded misclassification rates between 30 and 50 percent, but noted that these phases did have the lowest magnitude thresholds, and thus had the most observations. Baumgardt and Young (1990) found that for regional NORESS data both P_n/S_n and P_n/Lg amplitude ratios consistently separated mine blasts and earthquakes. Lynnes *et al.* (1990), in another study of NTS explosions and regional earthquakes (recorded at JAS), found that the spectral amplitude ratio of P_g/Lg in the 2-4 Hz range was fairly successful at differentiating events, but performed more poorly at lower frequencies. Above this bandwidth SNR problems resulted. Further, they noted that the ratios for the explosions increased with magnitude and depth. Kim *et al.* (1993) found that P/Lg spectral ratios measured in a multivariate scheme between 5 and 25 Hz were quite successful at distinguishing earthquakes from quarry blasts in New England.

Walter *et al.* (1995) extend the study of Taylor *et al.* (1989) by applying P_n/Lg and P_g/Lg amplitude ratios to a comprehensive data set consisting of explosions from the three testing sub-regions and earthquakes lying within or very near to the Test Site, thus minimizing path effects. However, only two LLNL stations were used. They found that network-averaged P_n/Lg amplitude ratios (6-8 Hz) plotted vs. magnitude ($M_L(\text{coda})$) fairly well separated events above $M_L(\text{coda})=3.5$, barring one significant outlying shallow earthquake. At lower magnitudes the two populations begin to merge. P_g/Lg results are similar but there is more overlap in the two populations.

We apply our version of this discriminant, which is essentially a measure of the root mean-square P_z/S_z wavetrain particle velocity ratio, to TERRAscope and other Western U.S. IRIS stations. Besides giving the results for the aggregate data set, we will show results for 8

individual stations -- a significantly larger number of stations than in these aforementioned studies. Again we take a simple, empirical approach to the problem and do not attempt to introduce receiver or path corrections.

2.2 Method

The source properties that we want to quantify are the short-period ($f \geq 1.0$ Hz) P-wave and long-period ($0.167 \leq f \leq 0.05$ Hz) surface-wave energy levels, the ratio of which is used as the discrimination criterion. The short-period bandpass is similar to that used to measure teleseismic P-wave amplitudes for the $m_b:M_s$ discriminant. The long-period bandpass represents the predominant frequency range of the fundamental-mode Airy phase at regional distances (Alewine, 1972). This short-period vs. long-period energy ratio ($E_{spPz}:E_{lp-3}$) is defined as:

$$E_{spPz}:E_{lp-3} = \frac{\int_{t_p}^{t_s} v_{sp}(t)^2 dt}{\sum_{i=1}^3 \int_{t_1}^{t_2} v_{lp}(t)^2 dt} \quad (1)$$

with the summation being for the three components and t_i denoting the windowing times determined from travel path length and the wavetrain of interest: t_p corresponds to the time before the onset of the P-wave and t_s the time prior to the S-wave onset -- usually 5 to 10 secs beforehand, and t_1 and t_2 bracket the time window of the fundamental Rayleigh and Love waves. The short-period and long-period ground velocities are respectively v_{sp} and v_{lp} . The velocities are squared in order to obtain units of energy; the term for the unit mass of the particle of motion cancel-out in the numerator and denominator. Essentially we are quantifying the energy in specific wavetrains and bandwidths. Kanamori *et al.* (1993) used the same methodology to quantify the energy in the broadband S-wavetrain as a regional measure of energy magnitude.

Summation of the three long-period components is done in order to account for both the Rayleigh and Love wave energy as discussed above. Should only the vertical component data be available, this discriminant measure would be no more effective than the conventional regional $m_b:M_s$ method. Should one component be down, an ersatz modification can be made to the method in order to obtain useful information from the remaining components: the 2-component sum can be multiplied by a factor of 1.5, thereby assuming the energy on the missing component to be an average of the other two components. However, if the tangential component primarily comprises this missing component, one is again confronted with the situation of only measuring the P-SV system, thus being potentially susceptible to radiation pattern effects of earthquakes, and it would be best to throw-out the observation.

In developing this discrimination criterion we found that the long-period energy is best measured by applying a narrow band-pass filter (between 7 and 20 secs) to isolate the regional fundamental-mode surface wave. Because explosions are relatively shallow sources, they generate large Rg waves as well as scattered, large amplitude, surface-wave coda with periods of 6 secs or less. This feature is observed in Figure 1. Note that on both the broad-band displacement and PE traces for KEARSARGE there is sizable Rayleigh-wave coda after the Airy phase. In comparison, the long-period Lee Vining and Little Skull Mountain earthquake records show very little or no Rayleigh-wave coda, rather they each primarily display a fundamental-mode Airy phase and some earlier arriving higher-mode waves.

These coda-like surface waves generated by NTS events are believed to be generated preferentially by shallow sources. Kafka (1990) found a similar correspondence between shallow events and coda energy in a study of New England earthquakes and quarry blasts. Mayeda and Walter (1996) found that shallow earthquakes ($D \leq 5$ km), collapses and explosions show anomalous spectral peaking in the 0.2-0.4 Hz frequency range of coda waves relative to normal depth earthquakes. They suggest that this may be related to the strongly depth-dependent phase Rg which scatters into the coda. Filtering out the short-period coda surface waves improves this discriminant as such energy would increase the measured long-period energy

level, causing any shallow source to appear to be an earthquake.

As with other short-period:long-period discriminants, the limiting measurement is still the long-period signal. For this study observations with signal to noise levels as low as unity are used. More accurate estimates of the long-period signal can be made if the effect of noise is removed. One method to improve the long-period signal measure at these lower magnitude thresholds is to remove the effects of ambient noise by taking a portion of the integrated energy outside the arrival window of the transient signal and normalizing this sum (E_N) to the length of the time window of interest and obtaining a modified integrated energy for the signal, E'_S :

$$E'_S = E_S \times \frac{E_S}{(E_S + E_N)}, \quad (2)$$

for which E'_S would near E_S for high SNR records and $E_S/2$ for the case $E_N = E_S$. However this technique was not applied in this study.

The short-period P:S ratio ($E_{spPz}:E_{spSz}$) is defined similarly to (1), except the denominator is replaced by the integrated short-period vertical component energy in the S/Lg wavetrain. Using these short-period phases the SNR only becomes an issue for $M_L \leq 3.1$ events.

2.3 Data Analysis and Results

Broadband, regional recordings of 131 earthquakes in western North America and 32 Nevada Test Site (NTS) underground explosions occurring between 1988 and 1994, and having $M_L \geq 3.5$, comprise the data set. The data comes from the TERRAscope array as well as other IRIS dial-up stations, with the more recent events having better station coverage. Altogether there are 107 event-station pairs for explosions and 650 for earthquakes. Figure 2 displays the study area and events used in this study. This region is unique in that there is a large amount of seismicity, both natural and man-made, which is well recorded by various broadband networks.

All data were processed in the same fashion. The analysis process described above is quite

simple to automate, so as a first run all events were done this way. The time interval chosen was determined from the distance-velocity relationship:

$$r/v_1 - T_0 \leq T_{\text{window}} \leq r/v_2 + T_0 \quad (3)$$

where r is the path distance, v_1 and v_2 are the maximum and minimum wavetrain velocities respectively, and T_0 is an additional margin of time. After some experimentation it was found that most suitable velocities for windowing the short-period P-wavetrain were $v_1 = 7.9$ and $v_2 = 4.7$, and for the long-period surface wave and short-period S-wave (Lg) trains $v_1 = 4.6$ and $v_2 = 2.5$ best windowed these phases. The windows were chosen to include the onset and the majority (roughly 85 or more) of the wavetrain of interest. $T_0 = 5$ secs for both cases.

Inspection of the energy curves indicates that high SNR events have sharp jumps in their energy curves. Primarily, the time windows were only set-up so as to automatically process a large number events, *i.e.* to make sure that the time window encompasses the entire wavetrain of interest. However, for the most consistent measurements it is best to use as narrow a time window as possible -- particularly for low SNR events, for which cases the integrated energy is primarily a function of window length.

We now provide examples of observed waveforms, their respective integrated energy curves, and the time windows used for the energy measurements for the closest four stations GSC, ISA, PAS and PFO. They are for a suite of typical regional events -- both explosions from the three NTS sub-regions and for earthquakes near NTS (from the Little Skull Mountain sequence). A catalog which lists these events is given Table 1. Their locations are shown in the blown-up inset of Figure 2.

Figure 3 displays vertical component velocity records of NTS shots recorded at GSC ($160 < r < 220$ km). At this station the long-period fundamental-mode Rayleigh wave energy is evident for all events, although in the case of Hunter's Trophy the Rayleigh wavetrain is within the noise level. We will address this problem later. In the short-period band the

explosions exhibit waveform characteristics which are site specific in that they are observed to be self-similar to other events from the same Test Site sub-region. This holds true for all TERRAScope records gathered to date; Pahute Mesa events tend to generate very little S-wave (or Lg) energy, while Yucca Flat events have strong S-waves which are often larger than the P-waves, and Rainier shots are intermediate in character with shear wave arrivals which rival the peak P_g wave in amplitude. The characterizations are based on visual inspection of the entire waveform database.

It should also be noted that the short-period waveforms for the Non-Proliferation Experiment (NPE) (Denny and Zucca, 1993) and the other Rainier shot, Hunters' Trophy, are very similar. In all cases the S-wavetrain for the explosions does not have a sharp onset, but rather is dispersive. This behavior also is born-out in the energy curves. The short-period integrated energy curve for Pahute resembles a step function produced by the very prominent P-wave arrival. The Yucca curve is more ramp-like with a second prominent ramp for the S-wave. Again the Rainier events are intermediate in character. The earthquakes all have their most pronounced jump in energy at the S-wave arrival.

Also note that in the broadband traces the $T \leq 7$ sec. dispersed Rg and short-period surface wave coda are the predominant phases on the Yucca Flat and Rainier Mesa events and that the Pahute shot also generates considerable energy of this sort, whereas the earthquakes exhibit little such energy with the exception of aftershock 3, the bottom record. This event is actually from Rock Valley, a zone of very shallow seismicity ($1 \leq D \leq 3$ km). (Smith and Brune, 1993). Walter *et al.* (1995) found this sequence to exhibit anomalous behavior characteristic of explosions using their discriminants. This shallow of an earthquake is expected to generate large Rg waves (Kafka, 1990). Note that this event did fall within the earthquake population with respect to the SP:LP discriminant.

In making comparisons between events it should be noted that the Pahute shot is larger than the others, so that it has a higher SNR. There are no distinguishing features on the long-period recordings between the three test sub-regions or for the NPE explosion.

Figure 4 plots the waveforms for the same suite of events recorded at ISA ($230 < r < 270$ km). Once again the explosions tend to exhibit more Rg energy than do the earthquakes with the exception of aftershock 3 which is thought to be shallower than the other earthquakes. In the short-period passband the explosions exhibit very little Lg energy, even for the Yucca shot, thus yielding step-like energy curves at the P-wave arrival, but with no significant jump at the S-wave arrival. We attribute this lack of Lg to blockage caused by propagation across the Sierra Nevada block and Death Valley, as at the other stations there is always a prominent S-wave or Lg phase for Yucca shots. This observation becomes more apparent after viewing the PAS and PFO records. The earthquakes all have sharp, prominent S-wave arrivals which are due to direct body waves as well as to trapped, shallow crustal Lg energy.

For the long-period passband (middle column) the signal to noise level becomes an issue. The two Rainier events' (the 3rd and 4th rows of seismograms) surface waves have SNR's approaching unity, as are those for the bottom two earthquakes. The integrated energy for these low SNR records correspondingly is primarily a function of the window length, as the noise dominates the contributions to the curve, showing only small rises at best at the surface wave arrival. $E_{spPz}:E_{lp-3}$ measurements for such cases should be considered ratio minimums, for the actual long-period surface signal contribution is less than the apparent signal. Consequently the discriminant was applied to records for all events with $M_L > 3.5$, in part to ascertain its performance at its measuring threshold. Constraining the time window used to be as narrow as possible also mitigates this problem somewhat. We did re-apply narrower time windows (than those described earlier, which were used for the entire data set) to calculate the long-period energy for individual low SNR records.

These recordings are at fairly near distances ($160 < r < 270$ km), so that propagation effects are minimal. An extension of these comparisons to the more distant ($330 < r < 400$ km) stations PAS and PFO is given in Figures 5 and 6, respectively.

Again the explosions exhibit more late arriving energy due to the Rg phase and scattered phases than do the earthquakes; the exception being aftershock 3 or the Rock Valley earth-

quake. The late arriving energy seen in the aftershock 2 records is due to a separate local event that can be seen more clearly in the short-period play-out. At these distances the long-period surface wave signals begin to merge with the seismic noise, however these records suggest that the long-period portion of the source spectra doesn't discontinuously drop-off, but rather decreases below the SNR of the recording site. For events with comparable long-period amplitude events, the short-period records of the explosions have larger amplitudes than the earthquakes, also supporting the $E_{spPz}:E_{lp-3}$ discrimination criterion.

At these more distant stations Pahute recordings still retain their strong, prominent P-wave arrivals, with only small amounts of energy in the expected shear wave time window, whereas the other explosions more closely resemble earthquake waveforms in that they have comparable amounts of S-wave energy. Divider, the Yucca event, in fact has larger amplitude S-waves than P-waves and its S-wave energy is greater than the P-wave's as well. One can see this visually in the integrated energy curves. Still, for earthquakes, the S-wavetrain arrival is more distinct and generally larger than the P-wave arrival. This general observation does not hold for case of the PFO recording of the explosion Divider, however, which has a very sharp S-wave arrival more than twice as large as anything in the P-wavetrain and looks very much like a typical short-period earthquake record. It should be noted that these waveforms for the NTS events tend to be very characteristic of each sub-region; for instance, this sharp S-wave is observed at all PFO recordings of Yucca shots.

This increase in S-wave/Lg energy in the more distant explosion records is believed to be due to propagational scattering effects of already converted P to SV phases. Such energy is absent from most recordings of Pahute events, whereas there is evidence of significant conversion to S-wave energy for Rainier and Yucca recordings. We have examined all available explosion records and found that in the short-period bandwidth, all explosions recorded at any one station and from one specific NTS sub-site are quite similar.

Visual inspection of each station-event pair energy curve was performed in order to insure that the time windows encompassed the appropriate wavetrains for the energy measurements.

An estimated 10 or fewer of the records needed their time windows modified. For the purposes of an operational monitoring system, a regionalized velocity map could be implemented as part of a calibration process in order to fully automate such an analysis.

A plot of the ratio of $E_{spPz}:E_{lp-3}$ vs. distance for all events above $M_L=3.5$ is displayed in Figure 7a. The explosions tend to have higher value ratios than do the earthquakes at all distances. Although there is not complete separation of the two populations, overlap is small with 8 of the earthquakes and 5 of the explosions being misclassified. It appears that separation is greatest at longer distances ($r \geq 900$ km) and least at distances less than 400 km. This effect may have to do with the sampling populations, however. Earthquake datum points at larger distances are usually from larger events ($M_L \geq 5.0$), for which the difference in relative short-period to long-period energy levels between earthquakes and explosions is already firmly established.

There is significantly more scatter in the earthquake population than in the explosion population. Several factors are believed to be responsible for this effect: (1) large azimuthal variation for earthquakes due to mechanism whereas explosions are predominantly isotropic sources, (2) paths are more varied for earthquakes, and (3) explosions have a extremely regular source depth of less than 1 km, whereas earthquakes within this geographic region range between 1.0 and 15 km in depth, with most earthquakes being between 5 and 12 km (Zhu and Helmberger, 1996). Another quality of the earthquake energy ratio data is that population outliers are skewed, with the upper boundary having an abrupt end, while the lower boundary is more diffuse. It is interesting to note in that the energy ratios for the NPE chemical explosion are similar in value to those of the nuclear ones.

Often discriminant parameters are plotted vs. magnitude in order to remove source scaling effects, *i.e.* Mayeda and Walter (1996) and Taylor *et al.* (1989). As we have not removed propagation effects, which are significant, it is not possible to directly compare the energy ratio values to magnitude. However we did investigate the effect of normalizing the energy ratio values with respect to magnitude. From our $E_{spPz}:E_{lp-3}$ observations it was evident that

the larger events (particularly earthquakes) usually had lower energy ratios, thus we applied a normalization of the form:

$$E_{spPz}:E'_{lp-3} = E_{spPz}:E_{lp-3} \times 10^{(m-m_0)}, \quad (4)$$

where m is the event's magnitude (m_b or an equivalent scale) and m_0 is a reference magnitude we chose as 5, as it is around the median magnitude of events being analyzed. Figure 7b plots this normalized energy ratio vs. distance. Far better separation with respect to event type is obtained at the shorter distances, while the more distant datum points show no improvement in separation. This effect may be due to the signal level of the records. At greater distances most of the available explosion data are for small events ($M \leq 4.5$) whereas larger events ($M \geq 5$) comprise most of the earthquake data. The larger events' energy ratios will increase more than the smaller ones when normalized, so consequently in this case the normalized earthquake energy ratios will rise relative to those of the lower magnitude explosions.

How well the $E_{spPz}:E_{lp-3}$ discriminant performs at individual stations is of interest in order to ascertain whether or not there is significant station bias in these measurements. Also individual station performance is an important aspect of operational considerations, since sparse station coverage and low magnitude threshold monitoring requirements will often require that identification be made with single station observations.

The data recorded at the four longest running TERRAscope stations are plotted in Figure 8 a-d. These four stations (GSC, ISA, PAS and PFO) are the closest stations to NTS and they have recorded the largest number of events. As in the complete data set plot there is some overlap in earthquake and explosion populations, but all explosions still plot higher than most earthquakes. Also note that there are not significant differences between the test sub-regions, rather all explosion datum points tend to cluster. The largest scatter in explosion values is for PAS, which also had the most data. However the scatter shows no correlation with test area. As for station site effects, these four stations all have earthquakes in the same distance range

and their energy ratios plot in the same range implying that receiver effects are relatively small.

Plots of the $E_{spPz}:E_{lp-3}$ ratio for the stations ANMO, TUC, COR, and BKS (along with STAN) are displayed in Figure 9 a-d, respectively. No station related patterns are found, implying that receiver effects are fairly insignificant.

Besides comparing integrated energy ratios, SP:LP peak ground velocity amplitude ratios were also determined for all data, the results of which are shown in Figure 10. The long-period value is the sum of the three component peak values. This method separates the two populations about as well as the integrated energy ratio method. There are two advantages to using peak amplitude measurements. As peak amplitudes are used, better measurements can be made of very low SNR records and analog data (such as historical analog seismograms) can be used as well.

As mentioned earlier, we also examined the potential of a short-period P to S (or Lg) discriminant ($E_{spPz}:E_{spSz}$). This measure is potentially useful for smaller events which radiate little or no observable long-period surface wave energy. This measurement is quantified similarly to $E_{spPz}:E_{lp-3}$, except that the denominator now is an integral of the short-period squared-velocity over the S-wave (including Lg) time window. The velocities used to window the data are 7.9 km/s and 4.7 km/s for the Pnl wavetrain, and 4.6 km/s and 2.5 for the S/Lg wavetrain. As this method only requires short-period data, the measuring threshold is lowered to $M_L \geq 3.0$. At closer distances ($r \leq 200$ km) this threshold can be extended to even lower magnitudes.

$E_{spPz}:E_{spSz}$ ratios for the data set, which includes all the events previously studied as well as others collected in the $3.0 \leq M_L \leq 3.5$ range, are displayed in Figure 11. At this threshold it was possible to include several quarry blasts from Southern California as well as shots from the Southern Sierra Continental Dynamics (SSCD) Project (Fliedner and Ruppert, 1994) to the data set. These shots are marked by squares in the figure. The separation of populations is poorer using this method, with overlap being estimated at 50, however the explosions popula-

tion does, on average, have higher P:S energy ratios than does the earthquake population.

Several observations to note are that small chemical blasts do tend to have relatively high P to S energy ratios, while the larger NPE blast, on the other hand, yields relatively low energy ratios compared to nuclear explosions. However at these short periods, receiver (as well as path) effects are likely to be significant. Visual comparisons of event waveforms at different stations provided examples of this. Some stations, such as BKS, PFO, SBC, and STAN, exhibited considerably more S-wave and Lg wavetrain energy than other stations for the same events.

In an attempt to remove receiver effects, the $E_{spPz}:E_{spSz}$ data for GSC, ISA, PAS, and PFO were sorted by station and plotted in Figure 12a-d, respectively. Binning by receiver yields some improvement in separating the populations, however there is still considerable overlap between the earthquake and explosion populations. It is clear that the NTS sub-sites do display different trends, with Yucca and Rainier shots having more shear-wave energy than Pahute tests. This is particularly true for PAS which has the largest number of observations. Again the NPE shot plots low relative to most of the nuclear explosions.

$E_{spPz}:E_{spSz}$ ratios for the stations ANMO, TUC, COR, and BKS (along with STAN) are displayed in Figure 13 a-d, respectively. Again NTS explosions have been plotted by sub-region. Similar separation of source types is obtained, with Pahute events having the highest $E_{spPz}:E_{spSz}$ ratios.

Reviewing these short-period $E_{spPz}:E_{spSz}$ plots in Figures 12 and 13, it is apparent that the energy ratio levels do vary somewhat between stations, thus suggesting station bias. This is not surprising since this ratio is a product of two short-period measurements which are susceptible to relatively small-scale waveguide features. Thus this discriminant should either be applied on an individual station basis or would require station corrections.

The $E_{spPz}:E_{spSz}$ values also were normalized with respect to magnitude. This did not improve the separation between earthquakes and explosions as it had in the case of the $E_{spPz}:E_{lp-3}$ experiments, however it did increase the separation between explosions at Pahute

and those at Yucca and Rainier. This result implies that near-source effects play a crucial part in the conversion of P or Rg energy to S-wave energy.

Other studies of short-period phase ratios (Taylor *et al.*, 1989; and Lynnes *et al.*, 1990; and Walter *et al.*, 1995) have found that spectral amplitude ratios are magnitude dependent. To examine this effect we plot the unmodified $E_{spPz}:E_{spSz}$ values against M_L without correcting for distance. The results for the entire data set are shown in Figure 14; NTS events have been binned by sub-site for plotting. Little or magnitude dependence is apparent for the earthquakes. Taken in aggregate, explosions appear to show some dependence between $E_{spPz}:E_{spSz}$ and magnitude. However if the individual sub-sites are examined, no such dependence is observed. The Pahute events do have significantly higher $E_{spPz}:E_{spSz}$ ratios than do the other two sub-sites, which quantifies our visual observations that Pahute events generate "clean" explosion records with a prominent P-wave and little or no S/Lg wavetrain. However, as the Pahute shots are generally the largest from NTS, and consequently buried the deepest, this effect could also be due to depth and/or source medium.

Since we incorporate no receiver corrections, it is worthwhile to examine the discriminant at individual stations. Figure 15 plots this for the four closest and longest-running stations. No apparent magnitude dependence is observed for the $E_{spPz}:E_{spSz}$ values, although as magnitude is also a function of shot site, it is difficult to clearly ascertain. Also, no better separation of earthquakes and explosions is achieved than when plotted vs. distance (see Figure 12 for comparison). Similar results were obtained for the other stations, but are not plotted here.

Some studies of regional short-period discriminants have found better discrimination at higher frequencies (Kim and Richards, 1993; and Walter *et al.*, 1995) whereas Taylor *et al.* (1989) found no such effect. Consequently, we also examined the effect of applying a higher frequency band on the $E_{spPz}:E_{spSz}$ ratio. Figure 16 compares $E_{spPz}:E_{spSz}$ ratios for records convolved with a Wood-Anderson short-period (similar to high-passing at 1.0 Hz) instrument (open symbols) to those which have been further high-pass filtered at 4 Hz (filled symbols). The events used are those for which waveforms were shown in Figures 3-6. This subset of

events was used in order to minimize path effects for this comparison. The effect of taking the P:S energy ratio to higher frequencies increases the ratio value in general, but is greatest for the explosions. This result implies that explosions, compared to earthquakes, are relatively more deficient in S-wave (or Lg) energy at higher frequencies.

2.4 Discussion

There are several explanations for the observed difference in short-period:long-period spectral character between earthquakes and explosions. Source mechanism, no doubt, plays a significant role for earthquakes, however this effect is highly variable, which the large scatter in the $E_{spPz}:E_{spSz}$ earthquake population bears out.

The theoretical argument by Stevens and Day (1986) that source medium properties are a significant factor in accounting for the off-set in m_b-M_s between earthquakes and explosions is quite compelling, especially since earthquakes are almost always deeper than explosions and thereby have different source regimes. Shallow ($D > 5$ km) earthquakes, when they do happen, tend to be very low stress-drop events which are relatively enriched in long-period energy.

As for the source spectrum itself, earthquakes tend to be distributed sources with corresponding considerable rise times, as opposed to explosions which have relatively short rise times more aptly modeled as step-function point-sources at long-periods with an impulsive component (overshoot) at shorter periods. Dreger and Helmberger (1991) showed that broadband seismograms from small local earthquakes ($4.0 < M_L < 5.0$) can be modeled as distributed finite sources rather than as point-sources. Such distributed slip time functions will generally result in reduced short-period spectra relative to a point-source step moment. It is possible that even very small earthquakes ($M_L < 4$) behave similarly.

Consider the extreme case of a $M_L = 3.5$ earthquake for which the source radius is upwards of 1 km (Peppin and McEvelly, 1974; and Vidal and Munguia, 1991) and the rise time is a function of the shear velocity. The corner frequency of such an event is on the order of 1 or

2 Hz, following the method of Hanks and Wyss (1972). For a comparable magnitude explosion ($Y \approx 0.5$ kt), we obtain from the appropriate source-scaling curves (Denny and Johnson, 1991) a source radius less than a tenth this size and a corner frequency which is upwards of 4 Hz. Further, the rise time is dependent on the compressional velocity. Thus even at these low magnitudes, differences in source spectrum should be observable on the TERRAScope and IRIS broadband systems which have a flat velocity response up to 7 Hz.

It seems reasonable that a combination of these factors is responsible for the difference in short-period:long-period energy level between earthquakes and explosions.

The reason for the poor performance of the $E_{spPz}:E_{spSz}$ discriminant is that some explosions do exhibit strong S-wave and Lg wavetrains at short-periods which yield low P/S energy ratio values. This effect is strongly source-site dependent. For TERRAScope observations, such shear-wave rich explosions are without exception ones from Yucca and Rainier, with Yucca shots generally exhibiting the most shear-wave energy -- often it is the most prominent arrival, as can be seen in Figures 3-6. Pahute, on the other hand, has more deterministic waveforms which are similar to Kazakh and Lop Nor explosion waveforms at similar distances (Woods and Saikia, 1994).

Near-source scattering effects are a likely explanation for these waveform differences, as the travel paths from the three NTS sub-sites to the TERRAScope stations are not drastically different. We hypothesize that the basin structure of Yucca Flat, the irregular cavity geometries due to tunneling (Zhao and Harkrider, 1992), and perhaps even the topography of Rainier Mesa are the causes of P- to S-wave scattering at these two sites.

The results of Walter *et al.* (1995) imply that the P_g/Lg ratio is dependent on source medium properties such as gas porosity, with shallow, high gas porosity shots being enriched in Lg. As the shallower shots all tend to be lower magnitude ones from Yucca Flat and Rainier Mesa, it is not clear whether source medium or near-source scattering is the predominant factor in these depressed explosion P/Lg ratios. The fact that Rainier shot sites are in a perched aquifer, which is corroborated by the low gas porosity values for Rainier events in

the Walter *et al.* (1995) study, and yet these explosions still generate considerable S/Lg waves suggests that source medium is not the sole or even primary contributor to such effects.

The fact that the character of the short-period SLg phases or wavetrains is consistent for explosions from the same test area (Pahute, Yucca, or Rainier) -- particularly when comparing records from one station, but varies between sites suggests that the short-period shear wave energy is indeed due to near-source scattering effects such as conversion of Rg to Lg (Jih, 1995; Gupta *et al.* 1992; Jih and McLaughlin, 1988; and Stead and Helmberger, 1988). We suspect that the alluvial basin structure of Yucca Flat and the tunnel shots in the side of a mountain at Rainier Mesa are responsible for these scattering effects. The NPE records closely resemble their nuclear shot counterpart at Rainier (Hunter's Trophy), further suggesting that the shear wave energy level is predominantly due to near-source scattering effects.

This site-specific scattering for explosions may explain the results of some NTS discrimination studies, such as that of Murphy and Bennet (1982), which found poor separation on the basis of temporal P/Lg ratios. For their study only explosions $m_b < 4.8$, and consequently only ones from Yucca and Rainier, were examined. We infer from our observations that strikingly different results would be yielded for a population of Pahute explosions.

The difference in character of short-period S-wave arrivals between GSC and PFO recordings of Yucca Flat explosions is curious because their great circle paths vary by less than 15 degrees. However, this scattering of locally generated surface waves in the crustal waveguide can easily be a ray parameter dependent phenomenon which would allow complex patterns of wave packets to occur along the same azimuth, but at different distances, thus explaining the difference in S-wave arrivals between the two stations. As the prominent S arrival at PFO is only seen for Yucca events, it is not likely that the effect is caused by scattering along the path between GSC and PFO, otherwise it would be expected to be seen for the other explosion source areas.

There is also considerable scatter amongst the earthquakes short-period energy ratios. This is believed to be due to mechanism and propagation effects. As the vast majority (95) of

earthquakes studied occurred at depths greater than 5 km, assuming the seismic depth distribution and using the actual values from waveform modeling (Zhu and Helmberger, 1996) when possible, the crust is fairly homogeneous relative to that of the very shallow ($d < 1$ km) explosions, and scattering due to lateral variations near the source should be minimal in comparison. There were also several cases of earthquakes which had distinctly explosion-like waveform character with their P-wavetrain being the most prominent phase.

2.5 Conclusions

We have examined the performance of two empirical seismic discriminants, which use regional broadband waveforms, by applying them to a large data set of regional explosion and earthquake records from the Southwestern U.S and Baja, Mexico. Both of these methods are based on energy integral measurements of particular wavetrains in the time domain, which make them ideal to implement in an automated monitoring system.

The more promising discriminant is the $E_{spPz}:E_{lp-3}$ energy ratio, for which explosions tend to exhibit higher values than earthquakes. This method can be considered a variation of the $m_b:M_s$ discriminant applied to regional data. Although there is some overlap between the explosion and earthquake populations, the two source types do display significantly different overall trends with mean $E_{spPz}:E_{lp-3}$ ratios at a given distance being larger for explosions than for earthquakes. Misclassification rates are 8 and 5 for earthquakes and explosions respectively. This discriminant then could be applied to screen-out events that are easily identified, or as part of some multivariate discriminant scheme.

Because this ($E_{spPz}:E_{lp-3}$) discriminant is applicable to a sparse broadband network, it is ideal to be implemented in a global monitoring scheme such as the IDC's International Monitoring System (IMS). For an active tectonic region the threshold for the discriminant is $M_L = 3.5$ for earthquakes and $M_L = 4.0$ for explosions for epicentral distances up to 800 km, which correspond to teleseismic m_b threshold estimates (assuming the $M_L:m_b$ relationship obtained by Chung and Bernreuter, 1981) of $m_b=3.1$ and $m_b=3.6$, respectively. As observa-

tions suggest that the long-period signals decrease below the SNL for smaller events rather than discontinuously dropping off, schemes to lower the long-period measuring threshold further, such as phase-matched filtering or the use of deep bore hole instruments (with corresponding low noise levels) should be quite useful for this discriminant.

The $E_{spPz}:E_{spSz}$ ratio does not separate the source types as well as the $E_{spPz}:E_{lp-3}$ ratio, with an estimated 50 of the earthquake population overlapping with that of the explosions. Individual station performance is better with less than 30 overlap. From the time series and energy curves shown (Figures 3-6) it is clear why the $E_{spPz}:E_{spSz}$ energy ratio is not effective at identifying explosions from earthquakes. Near-source scattering and path effects can generate significant scattered shear wave energy which masks the short-period S-wave character of a source; our observations indicate that near-source scattering is the primary factor. The $E_{spPz}:E_{lp-3}$ ratio on the other hand is not as sensitive to such short-period effects, as the scattered energy shows up predominantly in the shear wavetrain and surface wave coda ($T < 6$ sec), and least in the short-period P_{nl} and long-period ($T > 8$ sec) surface wavetrains.

Better separation for the short-period P:S ratio is possible, however, when comparing data recorded at only one station. Also small chemical explosions ($M_L = 3.0$) can be distinguished from most earthquakes using this method, but only at nearer ($D < 200$ km) distances. No better separation of event types was obtained by plotting $E_{spPz}:E_{spSz}$ vs. magnitude.

The scattering effects discussed here directly effect the phases presently used for regional seismic discrimination (P, S and Lg). Consequently this issue should be addressed in future related regional discrimination studies.

Although such scattered energy is problematic for time-domain or spectral discriminants which use short-period phases since it will possibly mask the source character, it can be useful in identifying shallow events. TERRAscope observations of local earthquake sequences clearly show that shallow earthquakes ($5 \text{ km} < D$) generate far more scattered phases and coda wavetrains than do deeper events, which tend to look very "clean", *i.e.* contain mostly distinct, modelable phases. It may be possible to use such information as a depth discrim-

inant for seismic monitoring purposes.

Further investigations/modifications of this discriminant may well improve it further. Applying the $E_{spPz}:E_{spSz}$ ratio at higher frequencies ($f \geq 4$ Hz) has been shown to improve its performance (Figure 16). We are currently investigating the suitability of applying path corrections developed from broadband waveform modeling (Green's functions). Zhao and Helmberger (1994) have applied this technique for the purposes developing a regional discriminant based on the deterministic modeling of seismic sources and propagation effects at broadband and short-periods. Accounting for path effects also will make more direct comparisons of events possible, for example similar magnitude events, thereby removing source scaling effects which may be inherent to these discriminants.

Once broadband Green's functions are obtained it will be worthwhile to determine whether or not theoretical seismograms can produce similar energy ratio results. If so, these integrated wavetrain energy curves can be calibrated from broadband waveform modeling. Thus in a new geographic/tectonic region to be monitored, it will be possible to predict the behavior of earthquake and explosion energy ratios, thereby making it possible to identify potential first blasts.

3 Application of Regional Seismic Discriminants to the Colorado Plateau and Western Cordillera

3.1 Introduction

The aim of this study is to examine the applicability and portability of the energy ratio and $M_L:M_0$ seismic discriminants to other tectonic provinces. The specific region studied is that centered on the Colorado Plateau and including parts of the Western Cordillera. Besides containing significant natural seismicity, the region also is the site of four peaceful nuclear explosions (PNE's) from the Plowshare Program (Carder, 1962) as well as numerous large chemical blasts. Thus events from this region yield one of the most comprehensive data sets for discrimination studies.

We used data primarily from the World Wide Seismic Network (WWSN) stations in the Western U.S. The LRSM (long-range seismic monitoring) data set was also investigated, but very few usable records were found for the pertinent PNE's. As we wanted to use a consistent set of stations and instruments, we tried to use only WWSN records, along with the addition of PAS (Pasadena, CA) records. This station, which recorded during the same period as the WWSN, also has similar short-period and long-period bandwidth recording channels, so seismograms from it were included in the study. A map of the study area showing the stations and events used is shown in Figure 17. Many of the explosions examined are located near recorded earthquakes, thus providing good data for comparisons. For these stations both long-period and short-period data channels were usually available. Since all instrument responses were the same, except for gain (with the exception of PAS, noted above) it was decided to measure the gain corrected peak amplitude of the phase of interest from the appropriate passband instrument channels. P and S waves were measured from the short-period records and surface waves were measured from the long-period records.

The drawback to these data is that for the period covering the PNE's and chemical

explosions, the available are in analog format. This requires a simplified measure of energy by measuring peak amplitudes. This method was shown to yield similar results to those employing integrated energy measures as shown in Figures 7 and 10. Although in this example peak velocity amplitude was measured, we also found that peak displacement amplitude measurements behaved similarly.

3.2 Data Analysis

The earthquakes used are given in Table 1 and Table 2 lists the explosions used, with the first four events listed (GNOME, RIO-BLANCO, RULISON, and GASBUGGY) being PNE's. PNE yields were obtained from Springer and Kinnaman (1971 and 1975). Chemical explosions yields were obtained from BSSA's *Seismological Notes*.

As GNOME was detonated before the establishment of the WWSN, data available for this event were limited. Our search of LRSN microfilm data provided no useful recordings. Consequently, for this event, we made use of published data from then extant seismic stations. These consisted mostly of measurements of peak short-period amplitude for the primary P and S waves observations (Romney *et al.*, 1962) and, in one case, a 4 sec. surface wave measurement at ALQ (Hankins, 1962). Although this latter measurement was at a shorter period than the phase normally measured, which is an 8-14 sec. Airy phase, it was taken as an estimate of the longer-period maximum, thus providing a conservative estimate of the long-period portion of the SP:LP discriminant for an explosion. All amplitudes were given in instrument-gain corrected displacement, so a direct determination of the SP:LP ratio could be made for ALQ.

The results of the short-period:long-period (SP:LP) peak amplitude ratio (PAR) for the Southwestern United States are plotted in figure 18a. Although there is overlap in the earthquake and explosion populations, the majority of earthquakes lie below explosion data points at a given distance. The quality of the analog data were often poor, particularly for the short-period records, so our results have inherent errors which should be considered when interpreting the results.

Given the short-period and long-period WWSN instrument gains, it was difficult to find events for which the long-period signals were observable above the noise level and for which the short-period records were not off-scale. Further, the short-period traces were often not visible, except for peak marks, for nearly off-scale events. The error is also considerable for near noise-level long-period measurements, for which the amplitudes are comparable in magnitude to the measurement errors. Consequently peak amplitude measurement errors are estimated to be as large as 25% for both instruments (short and long period). The available data are much sparser than those of the TERRAscope study of NTS shots and Californian and Basin and Range earthquakes, necessitating the use of data having considerable measurement error.

The SP:LP data were also magnitude normalized as was done in the previous chapter, *i.e.* $E'_{sp:lp} = E_{sp:lp} \times 10^{(M_i - M_0)}$, where M_i is the body-wave magnitude of the event and M_0 is a normalizing magnitude chosen to be $M_0 = 5.0$. with the results show in Figure 18b. This has the effect of increasing $E_{SP:LP}$ ratios of nuclear explosions relative to earthquakes while earthquakes and chemical explosion ratios become more intermixed. Thus the magnitude normalization tends to improve the separation of earthquakes from nuclear explosions, whereas in either case the chemical explosions tend to fall within the earthquake population. Most of these chemical explosions are mine blasts which are likely to have distributed source of charges, as was the Pre-Gondola III experiment which consisted of seven (30 ton) row charges simultaneously detonated (Lander, 1969).

We next examined the short-period P:S ratio (S-P P:S) in terms of peak displacement amplitudes (again because it was not possible to accurately digitize and then integrate the short-period data). Figure 19a is a plot of this ratio vs. distance. The PNE S-P P:S ratios are generally all near or above unity, whereas the earthquake amplitude ratios fall below unity. The one exception was an earthquake datum point at 1535 km which has a ratio of nearly 2. This particular datum is for the BKS recording of the 1967 Colorado earthquake. The other 6 observations of this event all have significantly lower ratios, with LON at 1575 km being the

second highest at 1.14, while all the others have values below unity.

It is suspected that the small S-wave observations for earthquakes which are the cause of the high P:S ratios are due to Lg blockage (Kadinsky-Cade *et al.*, 1981), as the paths to BKS and LON cross the Sierra Nevada and Cascade ranges, respectively. These are both very prominent tectonic features which can strongly affect propagation. The arrival time of the S waves for these stations are indicative of Lg waves. However, since these are amongst the longest paths studied, the waves could be S-waves turning in the upper mantle. In this case the depleted S-waves may be due to the strong shear-wave attenuation known to exist under Western North America (Marshall *et al.* (1979). Unfortunately, usable data was not available for any explosions at station BKS. However LON did record RULISON at a comparable distance (1390 km) and it also has a relatively high P:S ratio even for explosions suggesting that these paths do preferentially attenuate S waves relative to P waves.

The chemical explosion data are scattered throughout both the PNE and earthquake populations, so this discriminant in its current form cannot be used to positively identify chemical explosions.

Another observation of note is that there appears to be little or no distance dependence to this ratio. Thus the S-P P:S ratio can be directly compared among all such data. Consequently one can reasonably average these values for an event and obtain a network average which should give more robust and reliable measure of the P:S ratio. The results of this procedure are shown in Figure 19b where the average P:S ratio is plotted vs. m_b . No magnitude dependence is observed, but both the nuclear and chemical explosions have higher ratios than earthquakes, with the PNE's showing the greater separation. The improvement of this short-period discriminant using a network average is similar to that found by Walter *et. al* (1995).

We next examined available digitally recorded seismograms for events in this region. Figure 20 is a map showing the events studied. Table 3 lists these events. Most of the events are within the same general region of the older analog data set (see Figure 1). No explosion data were available for comparison, but one mine collapse was well recorded and used here.

Without explosion data, the primary usefulness of this data is for directly comparing the peak displacement amplitude ratio to the integrated energy ratio.

Figure 21 (a,b) display SP:LP ratio vs. distance for the peak amplitude and integrated energy methods, respectively. The integrated energy plot has less scatter, indicating a more robust measurement, which is expected. These integrated energy earthquake data also fall within the TERRAScope earthquake population (see Figure 7a). The mine collapse is more distinct from the earthquake population in the peak amplitude plot, whereas in the integrated energy ratio plot, the two populations overlap more. This result is similar to another mine collapse in the Ural mountains which will be discussed in the next chapter.

Figure 22 (a, b) display S-P P:S ratio vs. distance for the peak amplitude and integrated energy methods, respectively. Again, the mine collapse data fall within the earthquake population in the integrated energy ratio whereas in the peak amplitude ratio plot, they tend to have higher ratios than the earthquake data. The integrated energy ratio earthquake data also fall within the same range as the TERRAScope earthquake population as shown in Figure 11.

Next, the peak amplitude ratios of the digital and analog earthquake data were directly compared in Figures 23 (a, b) for the SP:LP and S-P P:S ratios, respectively. In both cases the populations directly overlay. This implies that we have developed consistent measures of these quantities for both the analog and digital data. Further, regression between peak amplitude and integrated energy ratios for the digital records would allow empirical corrections to analog data for a region in which digital data are also available.

The third regional discrimination criterion we applied to events in the Colorado Plateau/Cordillera region was $m_b:M_0$, or the ratio of teleseismic P-wave magnitude to seismic moment (determined from regional surface wave or broadband waveforms). The events so analyzed are provided in Table 4 and shown on a map of the region in Figure 24. PDE m_b 's were used for all events in conjunction with M_0 's determined from several earthquake source studies (Doser and Smith, 1982 and 1989; Patton and Zandt, 1991; Herrmann, Dewey and Park, 1980; Fan and Wallace, 1991; Zhao and Helmberger, 1994; Everhart-Phillips *et al.*,

1981; Mayeda and Walter, 1996; and the Berkeley Moment-Tensor Catalog). Explosion moments, as well that of the 8/9/67 Colorado earthquake, were determined from peak to trough amplitudes of analog long-period records using the method of Woods and Harkrider (1995). Many of these events (earthquakes and explosions) were used in the integrated energy and peak amplitude ratio analyses.

Explosion moments for RULISON and GASBUGGY were taken from Burdick *et al.* (1992). These and all other explosion moments were determined by measuring the peak amplitudes of the regional Airy phases, which have been calibrated by waveform and dispersion modeling of regional Rayleigh waves (Woods and Harkrider, 1995). Analysis of RIO BLANCO used the same source region model and paths as RULISON (Burdick *et al.*, 1992). The Green's function to ALQ for GNOME was determined using the eastern New Mexico model of Stewart and Pakiser (1962). Smaller chemical explosion moment estimates were made using the appropriate path (and source region) model for the northern Colorado Plateau or Middle Rocky Mountains of Keller *et al.* (1976) to generate Green's functions.

Initially we intended to study $M_L:M_0$ (after Woods *et al.*, 1993). However, few, if any, of these events have M_L attributed to them, and since many events had few, if any, adequate short-period near-regional ($D < 600$ km) records, we chose to use $m_b:M_0$ instead. Teleseismic m_b has the advantage that there are usually multiple observations of it for any event of m_b 4.0 or larger, so that mechanism radiation pattern effects are minimized, whereas it may only be possible to observe an event regionally at one or two stations for smaller events in sparsely instrumented regions. Further, Patton and Walter (1993) have developed a theoretically based explanation for the $m_b:M_0$ differential between explosions and earthquakes.

Since explosions are not expected to generate S-waves except due to non-isotropic source contributions, non-isotropic medium, and propagation effects, M_L is not the ideal measure of its size, as M_L is usually measured on the P-wave for explosions and in the S-wave train for earthquakes. Thus two different phases, with different source characteristics are being measured. To investigate this effect we have analyzed the relationship of M_L to m_b in the Western

U.S. for explosions and earthquakes using several data sets. If an adequate empirical relationship between M_L and m_b can be established, then one can convert between the two for which ever discriminant ($m_b:M_0$ or $M_L:M_0$) is desired.

Chung and Bernreuter (1981), using the data collected by Nuttli *et al.* (1979), obtained the following regression relationships for Western U.S earthquakes:

$$m_b = 0.99M_L - 0.39, \quad (5)$$

where M_L is assumed error free, and

$$M_L = 0.83m_b + 1.28, \quad (6)$$

where m_b is error free. The actual relationship is somewhere between these two, which they estimate to be:

$$M_L = 0.92m_b + 0.85. \quad (7)$$

When they used NEIC m_b 's for the same events, they obtained:

$$m_b = 0.95M_L + 0.30 \quad (8)$$

and

$$M_L = 0.74m_b + 1.25, \quad (9)$$

respectively, with an estimated actual relationship of:

$$M_L = 0.88m_b + 0.54. \quad (10)$$

These results suggest that the magnitude scaling relationship between M_L and m_b is not best described by equation (5), as suggested by Herrmann and Nuttli (1982) in deriving the correction to teleseismic m_b between the Western and Eastern U.S., but rather having an appreciably different slope closer to 0.9. Thus the difference between the two magnitude

scales is not just a matter of a constant offset.

We performed the same regression analysis on an augmented data set which includes the older (Pre-WWSN) earthquake data of Nuttli *et al.* (1979). The results for M_L regressed vs. m_b (which is error free) are shown in Figure 25a. The dashed lines represent the 2σ (standard deviation) confidence levels to the regression line. This relationship

$$M_L = 0.91m_b + 0.86, \quad (11)$$

is very similar to equation (7). Most importantly, the slope is 0.91, appreciably less than unity. Regressing m_b vs. M_L yields:

$$m_b = 0.94M_L - 0.05, \quad (12)$$

which is nearer in slope to the inverse relationship, equation (11) than are equations (5) and (6). Thus it is strongly suspected that a scaling relationship with a slope near 0.9 best describes the data. Since in our case we have m_b and wish to determine M_L , we perform all further regression analysis making M_L the dependent variable.

We next applied the same regression analysis to NTS explosions using teleseismic m_b and the average M_L for Pasadena and Berkeley, which is the same as that used by Nuttli *et al.* (1979). The results are shown in Figure 25b. The magnitude scaling relationship is:

$$M_L = 0.95m_b + 0.01. \quad (13)$$

The slope, 0.95, is again less than unity. When events with m_b greater than 6.0 are excluded from the analysis (as it appears that the M_L scale may be saturating at this point), the relationship becomes

$$M_L = 0.91m_b + 0.23 \quad (14)$$

which is consistent with our earthquake data regression, equation (11), although its offset is 0.63 M_L units.

As another check, we examined modern events recorded by TERRAScope, from which M_L was determined (Kanamori *et al.*, 1993). The regression results are given in Figure 26 and yield the relationship:

$$M_L = 0.83m_b + 1.23 \quad (15)$$

It seems that the $M_L:m_b$ relationships for all the data lie about a line with slope = 0.9. However, one cannot rule out a relationship with a slope nearer to unity within the 2σ confidence intervals. If we perform a fixed-slope regression, we obtain the following results for

$$M_L = 0.9m_b + b:$$

$b = 0.91, 0.72, 0.30$ for the Nuttli *et al.*, TERRAScope, and NTS data, respectively. The difference in offset between the two earthquake data sets is small and within the data variance, however the offset for the explosion data relative to the earthquake data is quite significant. If a slope of unity is assumed, the offsets (b) are respectively 0.41, 0.28, and -0.24.

Clearly, the relationship between M_L and m_b is different for earthquakes and explosions, with explosions having M_L 's approximately 0.5 magnitude units lower than earthquakes with the same m_b . This should be of no surprise as it is really a variation of the P:S discriminant with the improvement of a network-averaged P:S ratio which provides a more robust measure.

Figure 27 is a plot of m_b vs. M_0 for the events shown in Figure 24. The mine collapse lies just within the earthquake population whereas the explosions, both nuclear and chemical, plot higher than the earthquake population, with an offset of about 0.5 in m_b . Thus, this discriminant successfully identifies earthquakes from explosions. However if the m_b 's were converted to equivalent M_L 's using the appropriate relationships, the explosions would then plot within the upper bounds of the earthquake population as their M_L 's are relatively smaller. Consequently $m_b:M_0$ provides a better discriminant criterion than does $M_L:M_0$.

3.3 Conclusions

The performance of the three discriminants for earthquakes and explosions in the Colorado Plateau and Western Cordillera suggests that they are portable to other similar tectonic provinces. Previously they had been shown to work in the Basin and Range and throughout California with its many tectonic sub-regions.

Although the peak amplitude SP:LP ratio did not separate the earthquake and explosion populations, the magnitude-normalized SP:LP ratio does, with the nuclear explosions having a higher SP:LP ratio. However, smaller chemical explosions lie well within the earthquake population in both cases. The broadband digital recordings of recent earthquakes in the region provide a self-consistency check between peak amplitude and integrated energy SP:LP ratios. That is, the digital earthquake data integrated SP:LP ratios for this region fall within the earthquake population of chapter 1, while the peak amplitude SP:LP ratios are consistent with those of the analog earthquake data.

For the S-P P:S (peak amplitude) discriminant, explosions (both nuclear and chemical), on average, do have a higher ratio than earthquakes. However, as in the case of the TERRA-scope events, there is some overlap in populations. Unlike the case of the SP:LP ratio, there appears to be little or no distance dependence to the S-P P:S ratio, so network-averaged S-P P:S are easy to measure and yield far more complete separation of events.

In a related matter, it was found that there is significant offset in the $m_b:M_L$ scaling relationship between explosions and earthquakes, of approximately 0.5 M_L units (for a given m_b). This suggests some form of network-averaged P:S magnitude differential may be a very effective discriminant, especially for smaller events. On the other hand, it also suggests that $M_L:M_0$ would be less effective at distinguishing earthquakes from explosions than $m_b(P):M_0$, because explosion M_L estimates are relatively low in comparison to their m_b measurements.

Hence, $m_b:M_0$ effectively separates earthquakes from explosions. The one chemical explosion data point suggests an even larger separation from earthquakes, whereas the one available datum for a mine collapse lies within the earthquake population. We conclude that these

discriminants indicate some degree of portability to the Colorado Plateau and Western Cordillera regions. This issue is further examined for other regions and using digital data in the proceeding chapter.

4 Application of the Regional Seismic Discriminants to Central and Southwest Asia

4.1 Introduction

This chapter describes and discusses the performance of the two empirical energy-ratio discriminants and $m_b:M_0$ to events in central and Southwestern Asia. Regional recordings by digital broadband stations operated by various networks, as well as several regional broadband arrays, comprise the data set. These recordings are, for the most part, of the highest quality; consequently observational errors should be minimal. Several of these stations recorded one or more blasts from either the East Kazakh (or Semipalatinsk) or Lop Nor test site, or both. Body-wave magnitudes used came from PDE and M_0 measurements were taken from various sources.

The area covered by these data is large, as seen by comparing the scale between maps in this section and those in the previous chapter on PNE's, and encompasses a number of diverse and extreme tectonic regimes. These include the edge of the Siberian Shield, the Tibetan Plateau -- a large expanse of the world's thickest crust, and the Hindu-Kush -- a region of great orogeny involving subduction. As the region is so large the analysis was sub-divided by geographic region, in part for plotting purposes.

For all of the data sets we provide both the basic $spP_z:lp-3$ ratio and the magnitude-normalized ratio results.

4.2 Data Analysis

The first region to be investigated was central Asia -- encompassing the East Kazakh and Lop Nor test sites and the greater region around them. Figure 28 is a map of this region showing the events and stations used; events are color-coded with respect to the the station

recording them Table 6 provides event information for them. The station GAR, and the Tibetan PASSCAL array (Owens *et al.*, 1993) are each treated separately, while the few recordings from the stations in black are combined with the WMQ data set. WMQ, BRV, and GAR are the only stations for which records for explosions from both test sites are available for. In the case of WMQ, only seismograms for one explosion have been released from the CDSN. The Tibetan PASSCAL array did record one large ($m_b = 6.5$) Lop Nor explosion and four earthquakes from the same general direction, including one along azimuth to the test site. These events comprise the data set for this array.

Figure 29 shows the $spP_z:lp-3$ and magnitude-normalized $spP_z:lp-3$ ratios vs. distance for the WMQ data set. For all of the data sets we provide both the basic $spP_z:lp-3$ ratio and the magnitude-normalized ratio results. As with the TERRAscope results in Chapter 2, the magnitude-normalized energy ratio separates the two populations better than does the raw ratio. One earthquake near Lop Nor (black star) appears explosion like until the ratios are magnitude normalized. This again is similar to TERRAscope behavior in that earthquakes recorded at less than 300 km often fell within the explosion population until the data were magnitude normalized.

The WMQ data set consists primarily of crustal earthquakes. This was not the case for GAR which recorded a number of deep near-regional earthquakes within the Hindu-Kush region. Consequently the earthquake population was sorted by depth and plotted accordingly in Figure 30. The closer of the two explosions is from Semipalatinsk. Table 7 provides the event information. In both cases the explosions do separate from the earthquakes, however it appears that the deep ($d > 80$ km), mantle earthquakes tend to have higher $spP_z:lp-3$ ratios as they are depleted in surface wave energy relative to the shallower quakes. Earthquakes with default PDE depths of 33 km which plot high are also suspected of actually being deep event.

Results for the Tibetan PASSCAL array data are provided in Figure 31. These energy ratios are low compared to the other data sets analyzed; note the two order of magnitude reduction in the y axis relative to the other $spP_z:lp-3$ plots. Event information is given in

Table 8. In this case, the explosion yields lower $spP_z:lp-3$ energy ratios than any of the earthquakes. Even when the data are magnitude normalized it plots low -- well within the earthquake population. There are several possible explanations for this. The first, which only explains the explosion observations, is that it is quite large and did display significant Love waves, thus suggesting that additional long-period energy, due to tectonic release, has significantly decreased the $spP_z:lp-3$ ratio. The lack of observations for comparable-sized NTS and Semipalatinsk test site (STS) explosions precludes any direct check of this hypothesis. However, as such large explosions from historical analog data sets (Woods and Harkrider, 1995) do not show this same behavior with respect to $M_L:M_0$ (Woods *et al.*, 1993) (or $m_b:M_s$) this is unlikely the explanation.

The other possibility is that propagation effects are responsible for depleting the explosion P waves. Zhu and Helmberger (1993) and McNamara *et al.* (1995) found that short-period S-waves were drastically reduced relative to their broadband records for paths crossing the Northeastern portion of the Tibetan plateau. It is not clear whether this effect is due to low shear-wave velocities and attendant low anelastic Q, or due to scattering of the wavefield as it crosses into The Plateau. The crustal structure varies more here than just about any other continental regime and cause complicated propagational effects (Zhu *et al.*, 1995). Our preferred explanation is extreme lateral variation in the path structure which would affect the P-wave similarly. The fact that the earthquakes' energy ratios aren't depressed as much as the explosion's suggests strong azimuthal variation in the ratio which are more likely due to propagational affects -- possibly including scattering, whereas a hot lithosphere would tend to affect all paths crossing this region similarly in which case it would still be expected that explosion SP:LP ratios should be higher than those of earthquakes. This doesn't appear to be the case by interpreting this, admittedly, limited data set.

Thus at least in this tectonic environment, albeit a most extreme case, was found an instance in which propagation effects of some sort strongly influence the $spP_z:lp-3$ ratio, most likely primarily in the P-wave. This results highlights the necessity to calibrate all regions in

which this discriminant is to be applied.

This analysis was extended to the southwest, towards the Hindu-Kush region. Figure 32 is a map of this area showing stations and events. The two primary stations examined are NIL and AAK; some data from the KNET array, centered about AAK, were also analyzed. Here, events are again color coded with respect to the recording station; additionally, events recorded by both AAK and NIL are plotted in yellow. The Pakistan PASSCAL array (Sandvol *et al.*, 1994) and the events recorded by it are shown in Figure 39 (dark blue symbols). This was done so that the events in the Hindu-Kush region would all be clearly displayed, as a majority of the events lie within the comparatively small region.

Figure 33 displays the two spPz:lp-3 vs. distance plots for the PAK array data. Only earthquakes were recorded by this array during its temporary deployment. The populations are sorted by depth range. For the most part, in both the raw and magnitude-corrected cases, the deep earthquakes have higher energy ratios than the shallower ones. The behavior of the crustal earthquakes is similar to that of TERRAScope and central Asia data with ratios below unity, whereas the deeper, mantle events generally have higher integrated energy ratios plotting in the explosion population region, the exception being records recorded on apparent P-wave nodes.

What is apparent from the plot is that the deep earthquakes behave as explosion with respect to this discriminant in that they have high energy ratios relative to the shallower (crustal) earthquakes. This is not surprising in that it is well known that deep earthquakes tend to generate little if any fundamental mode surface wave energy. The $m_b:M_s$ discriminant has the same short-fall without applying a magnitude depth correction.

This difference in energy ratios due to waveform content is borne out in Figures 34 through 36, which show the vertical component records in different bandwidths with their attendant energy curve for a shallow ($d = 26$ km), intermediate ($d = 77$ km), and a deep ($d = 141$ km) earthquake, respectively. The top trace in each figure is the broadband velocity record, below which is the short-period ($0.5 < f < 3.0$ Hz) and its energy curve, and under which is the

long-period ($0.033 < f < 0.12$ Hz) velocity record and its energy curve. Note the large surface wave on the 4th trace centered at 220 sec and the corresponding step function in the energy curve for the shallow event. The longer period (T) cut-off of 8 sec. was used in an attempt to isolate long-period ($T < 6$ sec.) body wave energy from the LP measurement for data in regions with deep events.

For the intermediate depth earthquake in Figure 35 there is long-period energy coming in near 65 sec, which is presumed to be due to the long-period S-wave signature along with some surface wave as evidenced by the dispersive character of the wavetrain. The deep earthquake in Figure 36 is an even more extreme case, in that by far the largest long-period phase in the record is that due to a S-wave arrival at 120 sec; the later arriving surface wave-train is much smaller in comparison and the corresponding energy curve also reflects the fact that most of the incoming long-period energy is due to an impulsive S-wave (body wave) rather than a dispersive surface wave. Figure 37 shows the $spP_z:lp-3$ ratio vs. distance for NIL-recorded events. Again, explosion observations are available too. The explosions, which are only recorded at a large distance, do separate from the shallower earthquakes, however the deep earthquakes often also plot high. The events with PDE depths of 33 km which plot high are believed to be deep earthquakes. Figure 38 shows the $spP_z:lp-3$ ratio vs. distance for events recorded by AAK and the KNET array. Here, again, explosion observations are available too. The explosions, which are only recorded at a large distance, do separate from the shallower earthquakes, however the deep earthquakes often also plot high. The events with PDE depths of 33 km which plot high are believed to be deep earthquakes. In both the case of NIL and AAK, the $spP_z:lp-3$ ratio does separate explosions from crustal earthquakes.

Figure 39 is a map of showing events recorded by ABKT, as well as those recorded by the Pakistan PASSCAL array already discussed. Also shown is the January 5th, 1995 Ural mine collapse (square) which was well recorded by OBN and ARU. Plots of the $spP_z:lp-3$ ratios vs. distance for ABKT data and the Ural event are shown in Figure 40. Table 10 provides their event information. In this case no explosion data were available as ABKT is too far

away from Lop Nor to obtain good SNR records and it is really beyond what would be classified as regional. There is no discernible difference between the different depth earthquake populations, with most all earthquakes having ratios of less than 10.

The $spP_z:lp-3$ ratios of the mine collapse are low in comparison to those of the earthquake data. These results imply that collapses should fall at the low end of the earthquake population, however just the opposite result was found with the Solvay mine collapse in Chapter 3. In the case here no other ARU or OBN data was available for earthquakes within the regional distances considered. Obviously more data of this type needs to be examined in relation to intra-regional earthquakes. of

We next examine the short-period P:S ratio for the aforementioned data sets. Figure 41 shows results for WMQ (a) and GAR (b). At WMQ separation is fairly good between earthquakes and explosions, whereas at GAR it is not the case. No clear depth dependence for earthquakes is apparent.

For the Tibetan array, as was already discussed, there is strong attenuation of short-period S-waves, and it appears to be the same for P-waves from the $spP_z:lp-3$ analysis. Figure 42 shows evidence of this in the form of a record section for one earthquake with paths crossing the Northern Tibetan Plateau. As the propagational effects seem to be strong, with earthquakes often having no appreciable short-period S-wave, it was assumed that the S:P ratio would not recover a reliable estimate of the relative short-period P and S source spectrum due to path effects.

Figures 43 and 44a show the short-period P:S ratio for the stations centered about the Hindu Kush region. For NIL separation of earthquakes and explosions is good, but for AAK it is not. Again a correlation between energy ratio and earthquake depth is observed, with deeper earthquakes having a higher ratio.

Finally we examine $m_b:M_0$ for Eurasia. All m_b values were taken from PDE and the moments were taken from a variety of sources. As in the case of the Colorado Plateau (Chapter 3), this criterion fairly well separates the two source populations.

4.3 Conclusions

The $spP_z:lp-3$ energy ratio was found to be effective at identifying explosions from crustal earthquakes for all but once regional case which appears to be due to strong lateral variation in the crustal waveguide. As has been discussed, depth is an important factor in effecting the $E_{spP_z}:E_{lp-3}$ discriminant, with deep earthquakes generating little or no long-period surface wave energy and thus appearing explosion like by the discriminant's criterion.

Another consideration involving time windowing and deep events is that deep events often have very strong, fairly long-period S-wave arrivals as discussed in section 2. Should the surface wave time window be too permissive, the S-wave energy can show up as surface wave energy. Thus in such cases the event will have too large an apparent long-period integrated energy sum, thereby misplacing the deep event into the crustal earthquake class. This is not a problem for misidentifying explosions, but rather if this measurement is to be used as a depth estimator.

The short-period P:S was less successful at separating earthquakes from explosions. It worked well for WMQ, for which most paths are across continental shield or fairly small mountain ranges. However, in areas with more active tectonics, and consequently more heterogeneous crust, explosion and earthquake SP P:S ratios were quite similar. We believe that scattering effects are responsible for this.

The $m_b:M_0$ criterion does appear to discriminate earthquakes and explosions throughout Eurasia. This method appears to be a good hybrid procedure to obtain LP source information for the smallest possible events, *i.e.* with regional broadband records. Such events usually still have a teleseismic m_b estimate.

5 An Improvement to the Regional Short-period:Long-period Integrated Energy Ratio Discriminant with Results for Several Tectonic Regions

5.1 Introduction

The teleseismic $m_b:M_s$ discriminant is firmly established as the most reliable means to identify explosions from earthquakes (Pomeroy *et al.*, 1982), at least above a certain magnitude threshold. The caveats to this technique are that a rough estimate of depth -- itself a source discriminant of sorts -- is necessary to correct for surface wave amplitude, and that the magnitude threshold for this measure is limited by signal level of surface waves to events above $m_b > 4.5$. As no other discrimination technique in the literature is as successful at identifying seismic sources as this, finding a means to lower this magnitude measuring threshold is of considerable interest to seismic monitoring.

To this end Woods and Helmberger (1997) developed the ratio of integrated short-period to long-period energy (SP:LP) measure as a regional analog to the $m_b:M_s$ discriminant. The basis for this measure was regional TERRAscope observations which showed significant differences in the level of excitation of Pnl and surface wave-trains between explosions and earthquakes.

The SP:LP discriminant originated out of an attempt at quantifying, as simply as possible, the apparent differences in P wave and surface wave generation between earthquakes and explosions observed in regional TERRAscope data. Consequently the energy ratio was plotted vs. distance. However, to allow network averaging, to make it portable and to directly compare any two events, all data should be distance corrected so as to remove this variable for analysis purposes.

To accomplish this objective, we correct the data to a reference distance as in other magnitude scales. We chose $\Delta = 500$ km as a reference distance since it is beyond critical angle, but before the upper-mantle gradient causes problems. For the TERRAscope/IRIS station data

set, an empirical distance correction was determined. A simple r^n distance dependence fit the data well. The goodness of fit was judged by minimizing the distance dependence of residual log SP:LP ratios for explosions which were multiply recorded. It was assumed that the modulation of earthquake SP:LP levels by source mechanism effects would make distance dependence interpretation difficult. Alternative methods being developed involve semi-empirical distance corrections from synthetic modeling, and using master events corrected for mechanism and source level (moment) to determine an empirical distance correction.

5.2 Method and Data Analysis

As the SP:LP ratio is meant to perform as a simple measurement, so, too, a simple method to correct for distance is desired. We chose to first try a r^n dependence which has been shown in various studies (Zhu and Helmberger, 1996; Helmberger 1973; Romney *et al*, 1962; and Romney, 1959) to effectively model such amplitude dependence. As the SP:LP ratio is a ratio of two factors, both proportional to distance to a power, the exponent can be determined directly for the ratio or by obtaining a separate "n" for both the short-period and long-period integrated energies.

We first looked at the empirical power law for the SP:LP ratio. To determine the decay coefficient n, we both fit the distance decay curve and minimized the distance dependence of the intra-event distance-corrected energy ratio residuals. The residual distance-corrected energy ratio (E_{dc}) for sample (*i*) is defined as:

$$E_{dc}^i(\text{resid}) = E_{dc}^i - \bar{E}_{dc}, \quad (16)$$

where \bar{E}_{dc} is the network averaged energy ratio for an event. A suite of decay exponents at 0.5 unit intervals was used to obtain distance-corrected SP:LP energy ratios. Residual SP:LP ratios were then plotted vs. distance. It was found that $n = 3.5$ resulted in the smallest residuals and no apparent distance dependence, as shown in Figure 46.

As independent confirmation, empirical curves for explosion data were plotted along with a suite of synthetic curves, as shown in Figure 47. Again, $n = 3.5$ appears to fit the data best.

Distance-corrected SP:LP results are plotted vs. magnitude (m_b) in Figure 48. These are the same source-receiver pairs used in Woods and Helmberger (1997), and the energy ratio values have been converted to log ratio. The explosions tend to have appreciably larger SP:LP ratios than do the earthquakes with approximately 10% overlap of earthquakes into the explosion population. Further, network-averaging the SP:LP ratio for each event results in excellent separation of earthquake and explosions populations, as shown in Figure 49, and suggests a strong magnitude dependence of earthquake SP:LP values for $m_b \geq 4.5$, while the explosions, for the most part, appear distant independent. These results were averaged over as many as 9 stations for some events, but many events have fewer observations, and even an extra 1 or 2 measurements yields significantly more consistent and accurate measurements, providing a more accurate estimate of the true SP:LP source level.

There are a number of relatively low explosion points in this plot that reflect some of the well known anomalous NTS behavior relative to other test sites. In particular, the M_s 's from NTS events at Pahute seem consistently larger than expected in the global populations, as described by Stevens (1986). Secondly, a number of Yucca and Rainier events have extremely weak P-waves in the direction of TERRAscope, as discussed in chapter 2.

Our results are consistent with the results of Taylor *et al.* (1989) for regional $m_b:M_s$. The advantages to the SP:LP method are that less regionalization is required and that the SP:LP measurement includes the LP measurement of all three components. This mitigates the effect of observations of earthquakes at a Rayleigh-wave node, where strong Love waves are still produced yielding a large long-period component.

We have proceeded to analyze data from other regions of the world using the distance corrected SP:LP ratio, in particular, those for which both earthquake and explosion data are available. Results for the station WMQ (Urumqi, PRC) are plotted in Figure 50. Again, separation of the two source-type populations is good, with explosions having larger SP:LP

ratios than earthquakes. Data for only one Lop Nor explosion (denoted by a star) were available, the rest being from the Kazakh Test Site. However, there was also an earthquake which occurred close to the Lop Nor Test Site which was recorded and is plotted as a triangle. The two order of magnitude difference in energy ratio between the two events is similar to that seen in teleseismic $m_b:M_s$ data. There does appear to be an off-set in the SP:LP ratio relative to the Western United States (WUS) by a factor of 7. The Lop Nor explosion is near-in (250 km) while the Kazakh events are over 1000 km away, but their distance corrected SP:LP values are compatible. Thus it appears that this effect is not caused by the distance correction. However, this factor is equivalent to a Δm_b factor of 0.42 which is close to the known bias between WUS and the this region of central Asia.

Figure 51 shows the results for station NIL and surrounding regional events. The explosion data are all from Lop Nor, which is approximately 1600 km away from NIL. Most of the earthquake data are for closer events, but the distant earthquake data, which are also from the Lop Nor region, are plotted with filled symbols as are the explosions. There is a complete separation of these earthquake and explosion data. However, there is an overlap between explosions and deep ($d > 80$ km) earthquakes. As for the events with constrained PDE depths of 33 km, a number of them also appear to be deep, *i.e.* they have high SP:LP ratios. For such events for which we have since obtained regional moment-tensor solutions and source depths, the same pattern emerges: crustal earthquakes have lower SP:LP ratios than explosions whereas deep earthquakes often have comparable-sized ratios to explosions.

Finally, the distance-corrected SP:LP ratios were plotted vs. depth for data from several regions in Figure 52. The actual explosion depths are all between 0.4 and 1.0 km; the apparent depth difference between test sites was done for display purposes. The explosions with the lowest SP:LP ratios still can be separated from shallow ($d < 10$ km) earthquakes in any region studied; this is best observed on the log-depth plot. However, the NTS explosions do appear to have depressed SP:LP ratios relative to the other test sites. This is in accordance with waveform observations for typical explosion records from Lop Nor, Semipalatinsk, and

the three NTS sub-sites shown Figure 53. The NTS explosions all display considerably larger late arriving surface-wave and/or coda phases, and the relative excitation of P-wave to fundamental-mode surface wave is significantly lower than for the Asian explosions -- particularly relative to the Lop Nor explosion.

The fact that the SP:LP ratio does not separate deep (mantle) earthquakes from explosions is not surprising since deep events do not generate appreciable surface waves. The $m_b:M_s$ discriminant has the same problem. Thus an independent depth estimate is necessary to separate deep earthquakes from explosions using the ratio of P-waves to surface waves. Saikia *et al.* (1997) have found that the complexity of regional short-period ($f > 0.5$ Hz) S-waves is a good indicator of depth. We envision using the SP:LP energy ratio in conjunction with such a depth discriminant to yield a comprehensive monitoring algorithm.

5.3 Discussion and Conclusions

This study introduces a generalization of the SP:LP energy discriminant which makes it more useful for global monitoring as performed by the IDC and NDC, by introducing a simple distance-dependent power-law path correction. As discussed in Chapter 4, we find that explosions and often deep earthquakes plot high with respect to this ratio relative to shallow earthquakes. Plots of SP:LP energy vs. m_b and vs. depth for populations of Western U. S. events (earthquakes and explosions) along with Asian populations indicate common features with shallow earthquakes ($d < 15$ km) clearly separated from explosions. Such depth resolution is difficult to achieve. However, waveform modeling or Lg duration, amongst other methods, could be applied to the same broadband records on even a single station basis to obtain both an SP:LP energy ratio and a depth estimate for a global monitoring network/system. Consequently, all positively identified mantle earthquakes which have a high SP:LP ratio could be culled from the sample, and the focus of analysis could be turned to any crustal or indeterminate-depth events which have a high SP:LP ratio.

References

- Aki, K., 1967. Scaling law of seismic spectrum, *J. Geophys. Res.*, **72**, 1217-1231.
- Aki, K., M. Bouchon, and P. Reasenberg, 1974. Seismic source function for an underground nuclear explosion, *Bull. Seism. Soc. Am.*, **64**, 131-148.
- Alewine, R. W., 1972. Theoretical and observed distance corrections for Rayleigh-wave magnitude, *Bull. Seism. Soc. Am.*, **62**, 6133-6142.
- Basham, P.W., 1969. Canadian magnitudes of earthquakes and nuclear explosions in Southwestern North America, *Geophys. J. R. Astr. Soc.*, **17**, 1-13.
- Baumgardt, D. R. and G. B. Young, 1990. Regional seismic waveform discriminants and case-based event identification using regional arrays, *Bull. Seism. Soc. Am.*, **80**, 1874-1892.
- Brune, J. N., 1970. Tectonic stress and the spectra of seismic shear waves from earthquakes, *J. Geophys. Res.*, **75**, 4997-5009.
- Burdick, L. J., E. J. Garnero, J. M. McLaren, B. W. Woods, D. V. Helmberger, and D. G. Harkrider, 1992. Uncertainty in Yield Scaling at Low Yield, *Final Technical Report FR, WCCP-R-92-01, Woodward-Clyde, Pasadena, CA.*
- Carder, D. S., 1962. The Gnome Symposium Forward, *Bull. Seism. Soc. Am.*, **52**, 977-979.
- Chung, D. H. and D. L. Bernreuter, 1981. Regional relationships among magnitude scales, *Rev. Geophys. Space Sci.*, **19**, 649-663.
- Day, S. M. and K. L. McLaughlin, 1991. Seismic source representation for spall, *Bull. Seism. Soc. Am.*, **81**, 191-201.

- Day, S. M., N. Rimer, and J. T. Cherry, 1983. Surface waves from underground explosions with spall: Analysis of elastic and nonlinear source models, *Bull. Seism. Soc. Am.*, **73**, 247-264.
- Denny, M. D. and L. R. Johnson, 1991. Seismic moment estimation and the scaling of the explosion source, *Geophysical Monograph 65: Explosion Source Phenomenology*, editors: S. R. Taylor, H. J. Patton and P. G. Richards; AGU, Washington, D. C., 171-183.
- Denny, M. and J. Zucca, 1993. DOE Non-Proliferation Experiment includes seismic data, *EOS*, **74**, 527.
- Doser, D. I. and R. B. Smith, 1982. Seismic moment rates in the Utah region, *Bull. Seism. Soc. Am.*, **72**, 525-551.
- Doser, D. I. and R. B. Smith, 1989. An Assessment of source parameters of earthquakes in the Cordillera of the Western United States, *Bull. Seism. Soc. Am.*, **79**, 1389-1409.
- Dreger, D. S. and D. V. Helmberger, 1991. Complex faulting deduced from broadband modeling of the February 28, 1990 Upland Earthquake ($M_L = 5.2$), *Bull. Seism. Soc. Am.*, **81**, 1129-1144.
- Eberhart-Phillips, D., R. M. Richardson, M. L. Sbar, and R. B. Herrmann, 1981. Analysis of the 4 February 1976 Chino Valley, Arizona, earthquake, *Bull. Seism. Soc. Am.*, **71**, 787-801.
- Evernden, J. F., W. J. Best, P. W. Pomeroy, T. V. McEvilly, J. M. Savino and L. R. Sykes, 1971. Discrimination between small-magnitude earthquakes and explosions, *J. Geophys. Res.*, **76**, 8042-8055.
- Fan, G. and T. Wallace, 1991. The Determination of source parameters for small earthquakes

- from a single, very broad-band seismic station,, *Geophys. Res. Let.* **18**, 1385-1388.
- Fliedner, M. and S. Ruppert, 1994. Southern Sierra Nevada: P-wave velocity and Moho depth modeling, *EOS*, **75**, 585.
- Gupta, I. N, W. W. Chan and R. A. Wagner, 1992. A comparison of regional phases from underground nuclear explosions at East Kazakh and Nevada Test Sites. *Bull. Seism. Soc. Am.*, **82**, 352-382.
- Hankins, D. M., 1962. Observations from some GNOME Seismograms, *Bull. Seism. Soc. Am.*, **52**, 1075-1077.
- Hanks, T. C. and M. Wyss, 1972. The use of body-wave spectra in the determination of seismic source parameters, *Bull. Seism. Soc. Am.*, **62**, 561-589.
- Haskell, N. A., 1967. Analytic approximation for the elastic radiation from a contained underground explosion, *J. Geophys. Res.*, **72**, 2583-2586.
- Helmberger, D. V., 1973. On the structure of the low velocity zone, *Geophys. J. R. astr. Soc.* **34**, 251-263.
- Herrin, E. and T. Goforth, 1977. Phase-matched filters: Applications to the study of Rayleigh waves, *Bull. Seism. Soc. Am.*, **67**, 1259-1275.
- Herrmann, R. B., J. W. Dewey, and S. K. Park, 1980. The Dulce, New Mexico, Earthquake of 12 January, 1968, *Bull. Seism. Soc. Am.*, **70**, 2171-2183.
- Herrmann, R. B. and O. W. Nuttli, 1982. Magnitude: the Relation of M_L to m_{bLg} , *Bull. Seism. Soc. Am.*, **72**, 389-397.

- Jih, R. S. and K. L. McLaughlin, 1988. Investigation of explosion generated SV Lg waves in 2-D heterogeneous crustal models by finite-difference method, Teledyne-Geotech, AFGL-TR-88-0025, 57 pp.
- Jih, R. S., 1995. Numerical investigation of relative contribution of Rg scattering and incomplete dissipation to Lg excitation, *Proceedings of the 17th Annual Seismic Research Symposium*, Phillips Laboratory, Hanscomb AFB, MA.
- Kadinsky-Cade, K., M. Barazangi, J. Oliver, and B. Isack, 1981. Lateral variations of high-frequency seismic wave propagation at regional distances across Turkish and Iranian Plateaus, *J. Geophys. Res.*, **86**, 9377-9396.
- Kafka, A. L., 1990. Rg as a depth discriminant for earthquakes and explosions: A case study in New England, *Bull. Seism. Soc. Am.*, **80**, 373-394.
- Kanamori, H., J. Mori, E. Hauksson, T. H. Heaton, L. K. Hutton, and L. M. Jones, 1993. Determination of earthquake energy release and M_L using TERRAscope, *Bull. Seism. Soc. Am.*, **83**, 330-346.
- Keller, G. R., R. B. Smith, L. W. Braile, R. Heaney, and D. H. Shurbert, 1976. Upper crustal structure of the Eastern Basin and Range, Northern Colorado Plateau, and Middle Rocky Mountains from Rayleigh wave dispersion, *Bull. Seism. Soc. Am.*, **66**, 869-876.
- Kim, W-Y., D. W. Simpsom, and P. G. Richards, 1993. Discrimination of earthquakes and explosions in the Eastern United States using regional high-frequency data, *Geophys. Res. Lett.*, **20**, 1507-1510.
- Lambert, D. G. and S. S. Alexander, 1971. Relationship of body and surface wave magnitudes for small earthquakes and explosions, Teledyne Geotech, ARPA-TR-72-1714.

- Lander, J. F., 1969. Seismological Notes, *Bull. Seism. Soc. Am.*, **59**, 1023-1030.
- Lieberman, C. R. and P. W. Pomeroy, 1969. Relative excitation of surface waves by earthquakes and underground explosions, *J. Geophys. Res.*, **74**, 1575-1590.
- Lilwall, R. C., 1988. Regional $m_b:M_s$, Lg/Pg amplitude ratios and Lg spectral ratios for criteria distinguishing between earthquakes and explosions: a theoretical study, *Geophys. J.*, **93**, 137-147.
- Lynnes, C. S., R. Baumstark, R. K. Cessaro, and W. W. Chan, 1990. Pg/Lg discrimination in the Western United States, Teledyne-Geotech, GL-TR-90-0167, 35 pp.
- Mayeda, K. M. and W. R. Walter, 1996. Moment, energy, stress drop, and source spectra of western United States earthquakes from regional coda envelopes, *J. Geophys. Res.*, **101**, 11,195-11,208.
- Marshall, P. D., 1970. Aspects of the spectral differences between earthquakes and underground explosions, *Geophys. J. R. Astr. Soc.*, **20**, 397-416.
- Marshall, P. D., Douglas, A., and Hudson, J. A., 1971. Surface waves from underground nuclear explosions, *Nature*, **234**, 8-9.
- Marshall, P. D., D. L. Springer, and H. C. Rodean, 1979. Magnitude corrections for attenuation in the upper mantle, *Geophys. J. R. astr. Soc.* **57**, 609-638.
- Mayeda, K. M. and W. R. Walter, 1996. Moment, energy, stress drop, and source spectra of Western United States earthquakes from regional coda envelopes, *J. Geophys. Res.*, **101**, 11,195-11,208.

- Mueller, R. A. and J. R. Murphy, 1971. Seismic characteristics of underground nuclear detonations: Part I. Seismic spectrum scaling, *Bull. Seism. Soc. Am.*, **61**, 1675-1692.
- McNamara, D. E., T. J. Owens, and W. R. Walter, 1995. Observations of regional phase propagation across the Tibetan Plateau.s, *J. Geophys. Res.*, **100**, 22,215-22,229.
- Müller, G., 1973. Seismic moment and long-period radiation of underground nuclear explosions, *Bull. Seism. Soc. Am.*, **63**, 847-857.
- Murphy, J. R. and T. J. Bennett, 1982. A Discrimination analysis of short-period regional seismic data recorded at Tonto Forest Observatory, *Bull. Seism. Soc. Am.*, **72**, 1351-1366.
- Nuttli, O. W., G. A. Bollinger, and D. W. Griffiths, 1979. On the Relationship between Modified Mercalli Intensity and body-wave magnitude, *Bull. Seism. Soc. Am.*, **69**, 893-909.
- Owens, T. J., G. E. Randall, F. T. Wu and R.S Zeng, 1993. PASSCAL instrument performance during the Tibetan Plateau passive seismic experiment, *Bull. Seism. Soc. Am.*, **83**, 1959-1970.
- Patton, H. J. and S. R. Taylor, 1984. Q Structure of the Basin and Range from surface waves, *J. Geophys. Res.*, **89**, 6929-6940.
- Patton, H. J., 1988. Source models of the HARZER explosion from regional observations of fundamental-mode and higher mode surface waves, *Bull. Seism. Soc. Am.*, **78**, 1133-1157.
- Patton, H. J. and G. Zandt, 1991. Seismic moment tensors of Western U. S. earthquakes and implications for the tectonic stress field, *J. Geophys. Res.*, **96**, 18,245-18,259.

- Patton, H. J. and W. R. Walter, 1993. Regional moment:magnitude relations for earthquakes and explosions, *Geophys. Res. Lett.*, **20**, 277-280.
- Pechmann, J. C., W. R. Walter, S. J. Nava, and W. J. Arabaz, 1995. The February 3, 1995, M_L 5.1 seismic event in the Trona Mining District of Southwestern Wyoming, *Seism. Res. Let.*, **66**, no. 3, 25-34.
- Peppin, W. A. and T. V. McEvilly, 1974. Discrimination among small magnitude events on Nevada Test Site, *Geophys. J. R. Astr. Soc.*, **37**, 227-243.
- Pomeroy, P. W., W. J. Best, and T. V. McEvilly, 1982. Test ban treaty verification with regional data - A Review, *Bull. Seism. Soc. Am.*, **72**, S89-S129.
- Romney, C., B. G. Brooks, R. H. Mansfield, D. S. Carder, J. N. Jordan, and D. W. Gordon, 1962. Travel times and amplitudes of principal body phases recorded from GNOME, *Bull. Seism. Soc. Am.*, **52**, 1057-1074.
- Romney, C., 1959. Amplitudes of seismic body waves from underground nuclear explosions, *J. Geophys. Res.*, **64**, 1489-1498.
- Saikia, C. K., H. K. Thio, B. B. Woods, and D. V. Helmberger, 1997. Waveform complexity as a possible depth discriminant for the automated IDC System, *Proceedings of the 19th Annual Seismic Research Symposium on monitoring a CTBT*, sponsored by NTPO, AFTAC, DOE, DSWA, 281-290, PE 35145F.
- Sandvol, E., J. Ni, and T. Hearn, 1994. Seismic azimuthal anisotropy beneath the Pakistan Himalaya, *Geophys. Res. Let.* **21**, 1635-1638.
- Savino, J. L., L. R. Sykes, R. C. Lieberman and P. Molnar, 1971. Excitation of seismic surface waves with periods of 15 to 70 seconds for earthquakes and underground explo-

- sions, *J. Geophys. Res.*, **76**, 8003-8020.
- Smith, K.D. and J. N. Brune, 1993. A sequence of very shallow earthquakes in the Rock Valley fault Zone; Southern Nevada Test Site (abstract), *EOS*, **74**, 417.
- Springer, D. L. and R. L. Kinnaman, 1971. Seismic source summary for U. S. underground nuclear explosions, 1961-1970, *Bull. Seism. Soc. Am.*, **61**, 1073-1098.
- Springer, D. L. and R. L. Kinnaman, 1975. Seismic source summary for U. S. underground nuclear explosions, 1961-1970, *Bull. Seism. Soc. Am.*, **65**, 343-349.
- Stead, R. J. and D. V. Helmberger, 1988. Numerical-analytical interfacing in two dimensions with applications to modeling NTS seismograms, *Pure and Appl. Geophys.*, **128**, 101-193.
- Stevens, J. L and S. M. Day, 1985. The physical basis of $m_b:M_s$ and variable frequency magnitude methods for earthquake/explosion discrimination, *J. Geophys. Res.*, **90**, 3009-3020.
- Stevens, J. L., 1986. Estimation of scalar moments from explosion-generated surface waves, *Bull. Seism. Soc. Am.*, **76**, 123-151.
- Stevens, J. L and K. L. McLaughlin, 1988. Analysis of surface waves from the Novaya Zemlya, Mururoa, and Amchitka test sites, and maximum likelihood estimation of scalar moments from earthquakes and explosions, S-Cubed, SSS-TR-89-9953.
- Stewart, S. W. and L. C. Pakiser, 1962. Crustal structure in Eastern New Mexico interpreted from the Gnome Explosion, *Bull. Seism. Soc. Am.*, **52**, 1017-1030.
- Stump, B. W., 1985. Constraints on explosive sources with spall from near-source waveforms, *Bull. Seism. Soc. Am.*, **75**, 1312-1325.

- Taylor, S. R. and G. E. Randall, 1989. The effects of spall on regional seismograms, *Geophys. Res. Lett.*, **16**, 211-221.
- Taylor, S. R., D. D. Denny, E. S. Vergino, and R. E. Glaser, 1989. Regional discrimination between NTS explosions and Western U.S. earthquakes, *Bull. Seism. Soc. Am.*, **79**, 1142-1176.
- Thio, H. K. and H. Kanamori, 1995. Moment tensor inversion for local earthquakes using surface waves recorded at TERRAscope, *Bull. Seism. Soc. Am.*, **85**, 1021-1038.
- Vidal, A. and L. Munguia, 1991. Local magnitude and source parameters for earthquakes in the Peninsular Ranges of Baja California, Mexico, *Bull. Seism. Soc. Am.*, **81**, 2254-2267.
- Viecelli, J. A., 1973. Spallation and the generation of surface waves by an underground nuclear explosion, *J. Geophys. Res.*, **78**, 2475-2487.
- Walter, W. R., K. M. Mayeda, and H. J. Patton, , 1995. Phase and spectral ratio discrimination between NTS earthquakes and explosions. Part I: Empirical observations, *Bull. Seism. Soc. Am.*, **85**, 1050-1067.
- Woods, B. B., S. Kedar, and D. V. Helmberger, 1993. $M_L:M_0$ as a regional seismic discriminant, *Bull. Seism. Soc. Am.*, **83**, 1167-1183.
- Woods, B. B. and C. K. Saikia, 1994. Regional surface wave magnitude and moment determination methods applied to nuclear explosions at the Nevada Test Site: Implications for yield estimation and seismic discrimination, *Proceedings of the 16th Annual Seismic Research Symposium*, Phillips Laboratory, Hanscomb AFB, MA.
- Woods, B. B. and D. G. Harkrider, 1995. Determining surface wave magnitudes from regional NTS data, *Geophys. J. Int.*, **120**, 474-498.

- Woods, B. B. and D. V. Helmberger, 1997. Regional seismic discriminants using wavetrain energy ratios, *Bull. Seism. Soc. Am.* **87**, 589-605.
- Zhao, L. S. and D. V. Helmberger, 1994. Source estimation from broadband regional seismograms, *Pure and Appl. Geophys.*, **149**, 1168-1192.
- Zhao, L. S. and D. G. Harkrider, 1992. Wave fields from an off-center explosion in an embedded solid sphere, *Bull. Seism. Soc. Am.*, **82**, 1927-1955.
- Zhu, L. and D. V. Helmberger, 1995. Focal mechanism determination and propagation characteristics of high frequency S-waves on the Tibetan Plateau, *Proceeding of the 17th Seismic Research Symp.* sponsored by PL/AFOSR/DOE, 702-710, PL-TR-95-2108, ADA310037.
- Zhu, L., T. J. Owens, and G. E. Randall, 1995. Lateral variation in crustal structure of the Northern Tibetan Plateau, *Bull. Seism. Soc. Am.*, **85**, 1531-1540.
- Zhu, L. and D. V. Helmberger, 1996. Advancement in source estimation techniques using broadband regional seismograms, *Bull. Seism. Soc. Am.*, **86**, 1634-1641.

Table 1: Events with Waveforms shown in this study						
Event	Date	Time	Lat.	Lon.	Depth	m_b
Lee Vining	90/10/24	6:15:20	38.05	-119.16	8.3	5.4
Little Skull Mountain	92/ 6/29	10:14:22	36.68	-116.28	11.0	5.6
L.S.M. Aftershock 1	92/ 6/29	10:31:02	36.70	-116.25	5.0	4.3
L.S.M. Aftershock 2	92/ 6/29	10:40:50	36.76	-116.24	5.0	3.8
L.S.M. Aftershock 3	93/ 5/30	15:21:03	36.65	-116.15	2.0	4.0
Kearsarge (P)	88/ 8/17	17:00:00	37.29	-116.31	0.6	5.5
Montello (P)	91/ 4/16	15:30:00	37.25	-116.44	0.6	5.4
Divider (Y)	92/ 9/23	15:04:00	37.02	-115.99	0.4	4.4
Hunter's Trophy (R)	92/ 9/18	17:00:00	37.21	-116.21	0.4	4.4
NPE (R)	93/ 9/22	7:01:00	37.20	-116.21	0.3	4.1

Table 2: Analog Earthquakes Studied

Date	Time	Lat.	Lon.	m_b	Event
65/02/16	16:22	43.70	-105.0	4.9	Wyoming
66/01/05	0:37	39.8	-104.7	5.0	Colorado
66/01/23	1:56	37.0	-107.0	5.5	Dulce, New Mexico
66/01/23	6:14	"	"	4.3	Dulce aftershock
66/01/23	7:49	"	"	4.6	" "
66/01/23	11:01	"	"	4.3	" "
66/01/23	12:00	"	"	$m < 4$	" "
66/01/23	19:43	36.9	-107.1	4.5	" "
66/01/23	23:48	36.9	-107.0	4.6	" "
67/08/09	13:25	39.9	-104.7	5.3	Colorado
65/01/14	12:30	39.60	-110.20	4.5	eastern Utah
66/10/03	2:26	37.40	-104.10	4.5	Texas Panhandle
66/12/19	20:52	39.0	-106.5	4.6	Colorado
67/04/04	22:53	38.32	-107.75	4.5	Colorado
67/04/10	19:00	39.94	-104.75	4.9	Colorado
67/04/26	10:17	43.41	-108.77	4.7	Wyoming
68/11/17	14:33	39.50	-110.99	4.6	eastern Utah
69/12/25	12:49	33.40	-110.60	4.4	S.E. Arizona
70/05/23	22:55	38.07	-112.40	4.9	southern Utah
70/11/28	7:40	35.00	-106.70	4.5	northern New Mexico
71/01/04	7:39	35.02	-106.69	4.7	northern New Mexico
71/11/10	14:10	37.80	-113.13	4.5	southern Utah
73/03/17	7:43	36.09	-106.17	4.5	northeastern New Mexico
73/04/22	6:7	42.63	-107.85	4.8	Wyoming
74/02/15	13:33	36.50	-100.69	4.5	Oklahoma?
75/08/01	7:27	31.42	-104.01	4.8	southeastern New Mexico
76/01/05	6:23	35.84	-108.34	5.0	northwestern New Mexico
76/02/04	0:4	34.65	-112.50	4.9	central Arizona
76/02/09	3:7	34.61	-112.53	4.9	central Arizona
77/03/05	3:0	35.92	-108.29	4.6	Northern New Mexico
77/09/30	10:19	40.52	-110.44	5.1	eastern Utah
80/05/24	10:3	39.94	-111.97	5.0	central Utah
81/04/05	5:40	37.61	-113.30	4.2	southern Utah
81/04/02	16:10	39.91	-104.96	4.3	eastern Colorado

Table 3: U.S. PNE's and other Chemical Explosions Studied					
Date	Time	Lat.	Lon.	m_b	Event
61/12/10	19:00	32.26	-103.87	4.3	GNOME 3.1 kt
67/12/10	19:30	36.68	-107.21	5.1	GASBUGGY 29 kt
69/09/10	21:00	39.36	-107.95	5.3	RULISON \approx 40 kt
73/05/17	16:00	39.79	-108.37	5.4	RIOBLANCO 3 \times 30 kt
66/04/03	16:21	39.40	-106.40	4.7	Bechtel Mine, CO: 0.315 kt
68/10/30	17:00	47.92	-106.64	5.0	Montana, Pre-Gondola III
72/03/09	18:45	32.75	-110.49	4.5	Reliable Mine, AZ: 2 kt
73/04/19	17:00	34.30	-112.61	4.5	Zonia Mine, AZ: 2.07 kt
74/03/14	21:00	34.24	-112.69	4.1	Zonia Mine, AZ: 0.427 kt
82/09/20	3:55	33.95	-107.06	5.0	White Sands?
85/06/27	18:20	33.62	-106.48	3.4	White Sands: Minor Scale

Table 4: Digitally Recorded Events Studied					
Date	Time	Lat.	Lon.	m_b	Event
95/02/03	15:26	41.620	-109.760	5.0	Solvay Mine Collapse, WY
88/08/14	20:03	39.128	-110.869	5.3	San Rafael Swell, Utah
92/03/16	14:42	40.495	-112.078	4.8	Utah
92/07/05	18:17	35.987	-112.249	4.0	Western Arizona
92/09/02	10:26	37.047	-113.461	5.7	St. George, UT
93/02/04	6:18	35.965	-112.226	3.6	Grand Canyon, Arizona
93/04/09	12:29	28.608	-98.160	4.3	Texas
93/04/25	9:29	35.601	-112.142	5.0	Cataract Crk, AZ F.S.
93/04/29	8:21	35.579	-112.115	5.4	Cataract Crk, AZ M.S.
93/04/29	21:08	35.618	-112.141	3.6	Cataract Crk, AZ A.S.
93/05/07	15:34	35.629	-112.183	3.8	Cataract Crk, AZ A.S.
93/06/05	23:58	32.830	-115.610	3.5	Yuma, Arizona
93/02/04	6:18	35.965	-112.226	3.6	Grand Canyon, Arizona
95/03/19	18:36	35.000	-104.212	3.3	New Mexico
95/03/20	12:46	40.330	-108.550	4.1	Colorado
95/04/01	5:22	40.196	-108.984	3.3	Colorado
95/04/14	0:32	30.30	-103.30	5.6	Western Texas, M.S.
95/04/15	14:33	30.271	-103.324	4.3	Western Texas, A.S.
95/04/17	8:23	35.964	-112.223	4.1	Western Arizona

Table 5: Events used in $m_b:M_0$ Analysis

Date	Time	Lat.	Lon.	m_b	M_0	Event
61/12/10	19:00	32.26	-103.87	4.3	3.24e21	GNOME (a)
67/12/10	19:30	36.68	-107.21	5.1	2.0e22	GASBUGGY
69/ 9/10	21:00	39.36	-107.95	5.3	2.04e22	RULISON
73/05/17	16:00	39.79	-108.37	5.4	5.37e22	RIOBLANCO
67/ 8/ 9	13:25	39.9	-104.7	5.3	1.51e23	Colorado EQ
34/ 3/12	18:20	41.8	-112.9	6.1	3.1e24	Hansel Valley 2, UT (b)
34/ 3/13	15:05	41.8	-112.9	6.6	7.7e25	Hansel Valley 1, UT
62/ 8/30	13:35	41.8	-111.8	5.7	7.0e24	Logan, UT
62/ 9/ 5	16:04	40.72	-112.1	5.2	4.0e23	Magna, UT
63/ 7/ 7	19:20	39.6	-111.9	4.4	3.4e23	Levan, UT
64/10/18	18:33	41.7	-111.7	4.1	4.2e23	Cache Valley, UT
66/ 3/17	11:47	41.6	-111.6	4.6	8.1e23	Logan 2, UT
66/ 8/16	18:02	37.4	-114.2	5.6	1.1e24	NV-UT border
67/10/ 4	10:20	38.5	-112.1	5.2	2.5e24	Richfield, UT
71/11/10	14:10	37.8	-113.0	3.7	5.7e22	Cedar City, UT
72/ 1/ 3	10:20	38.6	-112.2	4.4	9.0e22	Elsinore, UT
72/ 6/ 2	03:15	38.7	-112.1	4.0	4.5e22	SW Sevier Co., UT
73/ 3/14	06:45	42.0	-112.6	4.2	3.3e23	Pocatello Valley 1, UT
75/ 3/27	04:48	42.1	-112.5	4.2	1.3e23	Pocatello Valley 2, UT
75/ 3/28	02:31	42.2	-112.5	6.0	1.86e25	Pocatello Valley 3, UT
75/ 3/29	13:01	42.0	-112.5	4.7	3.0e23	Pocatello Valley 4, UT
75/ 3/30	06:56	42.0	-112.5	4.7	1.3e23	Pocatello Valley 5, UT
76/11/ 5	02:48	41.8	-112.6	4.0	5.8e22	Hansel Valley 2, UT
31/ 8/16	11:40	30.4	-104.2	5.9	3.3e25	Valentine, TX (c)
59/ 8/18	06:37	44.88	-111.1	6.0	2.8e25	Hebgen Lake, MT 1
59/ 8/18	15:26	44.85	-110.7	6.5	3.1e25	Hebgen Lake, MT 6
59/ 8/19	04:04	44.76	-111.6	5.8	4.8e25	Hebgen Lake, MT 7
64/10/21	07:38	44.86	-111.6	5.8	1.1e25	Hebgen Lake, MT 8
66/ 8/16	18:02	37.46	-114.2	5.6	1.1e24	SE Nevada
75/ 2/28	02:31	42.1	-112.5	6.0	1.2e25	Pocatello Valley, ID
75/ 6/30	18:54	44.7	-110.6	5.6	7.5e24	Norris, WY
83/10/28	14:06	43.96	-113.9	6.9	2.1e26	Borah Pk, ID 1
83/10/28	19:51	44.07	-113.9	5.4	1.8e24	Borah Pk, ID 2
83/10/29	23:29	44.24	-114.1	5.4	2.0e24	Borah Pk, ID 3
84/ 8/22	09:46	44.47	-114.01	5.0	2.4e24	Borah Pk, ID 4
92/ 9/ 2	10:26	37.047	-113.461	5.7	1.51e22	St. George, UT (d)
76/ 2/ 4	00:05	34.7	-112.5	4.9	1.0e23	Chino Valley, AZ (e)
66/ 1/23	01:56	37.0	-107.0	5.5	6.2e23	Dulce, NM (f)
89/11/29	06:54	34.456	-106.891	4.6	2.0e22	New Mexico (g)
90/ 1/29	13:16	34.463	-106.879	4.5	1.7e22	New Mexico (g)

Table 5 (cont): Events used in $m_b:M_0$ Analysis

Date	Time	Lat.	Lon.	m_b	M_0	Event
63/ 7/ 7	19:20	39.6	-111.9	4.9	4.4e23	central Utah (h)
67/10/ 4	10:20	38.5	-112.1	5.2	4.7e23	Marysville, UT
72/10/ 1	19:42	40.58	-111.3	4.3	3.7e22	Heber City, UT
78/11/30	06:53	42.11	-112.49	4.7	1.2e23	Pocatello Villy, ID
80/ 5/24	10:03	39.94	-111.97	4.2	4.8e22	central Utah
81/ 4/ 5	05:40	37.61	-113.30	4.5	2.0e22	Southern Utah
81/ 5/14	05:11	39.48	-111.06	3.5	2.2e21	Gentry Mtn. UT
82/ 5/12	19:29	37.27	-115.08	4.0	8.0e21	Pahranagat SZ, NV
82/ 5/24	12:13	38.71	-112.04	4.0	1.3e22	central Utah
82/ 7/ 6	02:10	37.69	-115.05	4.7	2.7e22	Pahranagat SZ, NV
83/ 2/23	11:10	35.97	-114.71	3.9	4.8e21	Lake Mead
83/ 6/ 4	11:37	37.39	-115.21	3.6	2.5e21	Pahranagat SZ, NV
83/10/28	19:51	44.06	-113.89	5.8	2.5e24	Borah Pk, ID
83/12/ 9	08:58	38.58	-112.58	3.6	2.6e22	central Utah
84/ 8/ 2	11:01	37.30	-114.94	3.7	2.5e21	Pahranagat SZ, NV
84/ 9/ 2	19:11	39.08	-115.62	3.7	3.8e21	East central Nevada
84/ 9/ 8	06:16	44.44	-114.15	5.0	3.5e23	North central Idaho
95/ 4/14	00:32	30.30	-103.30	5.6	3.6e24	Western Texas, m.s. (i)
95/ 9/13	06:01	38.151	-107.976	4.6	9.1e22	Western Colorado
95/ 2/ 3	15:26	41.620	-109.760	5.0	1.78e16	Solvay Mine Collapse, WY
93/ 4/25	09:29	35.601	-112.142	5.0	2.09e23	Cataract Crk, AZ f.s.
93/ 4/29	08:21	35.579	-112.115	5.4	1.01e24	Cataract Crk, AZ m.s.
89/ 1/30	04:06	38.824	-111.614	5.4	6.03e23	So. Wasatch Plateau, UT
89/ 2/27	15:13	38.827	-111.616	4.2	8.9e21	So. Wasatch Plateau, UT
88/ 8/14	20:03	39.128	-110.864	5.3	8.32e23	San Rafael Swell, UT
88/ 8/15	14:50	39.126	-110.874	3.0	1.34e21	San Rafael Swell, UT
88/ 8/18	12:44	39.132	-110.867	4.4	4.27e22	San Rafael Swell, UT
88/ 7/14	17:31	44.456	-114.083	4.9	9.30e22	North, central Idaho (j)
94/ 2/ 3	09:05	42.7	-111.1	5.9	8.1e24	Eastern Idaho
94/ 2/ 4	02:42	42.7	-111.0	5.2	3.10e23	Eastern Idaho
94/ 6/ 7	13:30	44.6	-113.9	5.2	5.30e23	North, central Idaho
95/ 7/25	19:34	43.0	-111.14	4.1	3.70e22	Eastern Idaho
96/ 5/16	15:41	42.61	-111.27	4.3	1.40e22	Eastern Idaho
96/ 8/ 3	06:15	44.52	-114.14	4.1	1.07e22	Utah

(a) This study; (b) Doser and Smith, 1982; (c) Doser and Smith, 1989; (d) Zhao and Helmberger, 1993; (e) Eberhart-Phillips *et al.*, 1981; (f) Herrmann *et al.*, 1980; (g) Fan and Wallace, 1991; (h) Patton and Zandt, 1991; (i) Mayeda and Walter, 1996; and (j) Berkeley M-T Catalog

Table 6: Events used in the WMQ Energy Discriminant Study

Julian Date	GMT	Mag.	Latitude	Longitude	Depth	Recording Stations
88003	20: 9:21.4	4.4	38.43	91.34	10.0	WMQ
88280	13:10:53.6	5.0	39.584	74.595	33	WMQ
88283	12: 3:18.7	4.6	38.38	76.03	10.0	WMQ
88320	16:56:46.2	5.3	42.018	89.295	33	WMQ
90011	21:14:57.8	-	35.786	80.757	10.0	WMQ
90014	3: 3:19.2	-	37.819	91.971	-	WMQ
90021	7:53:31.9	4.6	41.534	88.728	33	WMQ
90127	5:17:37.6	5.3	36.032	100.342	33	WMQ
90135	22:29:59.3	-	36.119	100.118	14.0	WMQ
90165	12:47:28.8	6.1	47.869	85.076	37.0	WMQ
90165	14:18:10.6	5.2	47.892	85.050	58.0	WMQ
90187	17:22:50.3	4.2	43.240	89.681	10.0	WMQ
90187	17:55: 5.0	-	43.240	89.681	-	WMQ
90270	21:12:32.5	5.0	47.903	84.961	33	WMQ
90297	23:38:15.1	5.2	44.117	83.856	20.0	WMQ
90297	23:46:57.7	-	44.116	83.856	21.6	WMQ
90307	17:25:13.8	5.1	40.882	89.071	22.0	WMQ
90335	18: 9:28.8	5.0	40.854	73.553	29.0	WMQ
91002	2:58:49.7	5.1	38.152	99.961	13.0	WMQ
91006	15:46:38.6	4.9	38.77	88.31	22.0	WMQ
91147	9:13:33.3	-	49.519	94.759	19.0	WMQ
91260	18:53:22.2	4.8	43.141	87.968	22.0	WMQ
91288	20:20: 9.2	4.3	43.91	87.08	30.0	WMQ
92160	9:20:54.5	4.2	43.60	88.28	30.0	WMQ
92162	2:37: 1.2	4.4	38.62	90.15	10.0	WMQ
92332	16: 9: 9.1	5.3	41.98	89.28	14.0	WMQ
93048	2: 0:25.8	5.1	38.32	89.48	15.0	WMQ
95186	23:38:42.1	4.0	42.08	87.14	33	WMQ
89128	0: 3:14.4	4.6	44.90	79.73	33	BRV
88094	1:33: 5.7	6.0	49.917	78.945	EKZ	WMQ,BRV
88113	9:30: 6.7	4.9	49.79	78.11	EKZ	WMQ
88258	4: 0: 0.0	6.3	49.87	78.8	EKZ	(JVE)*
88273	7: 0: 3.1	4.7	41.750	88.470	LN	WMQ
88328	3:57: 6.7	5.1	49.818	78.071	EKZ	WMQ
88352	4:18: 6.8	5.9	49.85	78.93	EKZ	WMQ
89245	4:16:57.3	-	50.85	78.94	EKZ	WMQ
89277	11:29:57.6	4.6	49.83	78.09	EKZ	WMQ
89292	9:49:57.3	6.0	49.90	78.97	EKZ	WMQ
90228	4:59:57.6	6.2	41.564	88.770	EKZ	WMQ,BRV
95005	12:46:1.25	4.5	59.525	56.309	Ural	ARU,OBN

* WMQ, BRV, BAY, KKL

Table 7: Events used in the Energy
Discriminant Study of GAR

Julian Date	GMT	Mag.	Latitude	Longitude	Depth
89090	8:28:16.2	4.7	36.997	69.554	33
89124	22:25:26.0	4.8	38.194	72.432	57.0
89210	18:00:34.1	4.6	39.458	73.024	38.0
89217	9:15:58.9	4.6	38.567	73.877	33
89230	7:43:23.4	4.6	36.319	71.026	105.0
89232	10:36:50.9	4.6	38.318	72.947	69.0
89236	20:06:41.1	4.5	36.785	70.769	73.0
89265	10:39:49.5	4.5	36.760	71.637	33
90060	0:25:37.0	4.0	36.486	68.860	33
90064	23:04:22.1	5.0	36.770	73.030	20.0
90065	18:07:04.1	5.0	36.909	73.038	20.0
90065	18:22:12.7	4.1	36.954	36.954	10.0
90065	21:39:50.2	5.2	36.913	73.095	24.0
90073	17:39:22.9	4.6	36.860	73.275	33
90084	1:32:19.3	4.9	37.010	72.873	33
90084	15:10:40.1	5.1	36.979	73.062	33
90085	22:19:29.8	4.8	37.000	72.771	33
90091	0:46:48.2	5.1	35.814	70.943	75.0
90103	19:42:54.6	4.6	37.249	71.627	52.0
90108	5:12:08.2	4.6	39.297	74.951	33
90109	3:45:39.6	4.5	36.778	70.908	10.0
90109	22:41:31.0	5.2	34.018	69.742	33
90111	2:06:24.9	4.6	36.289	70.927	79.0
90114	20:35:00.8	4.8	36.540	71.473	46.0
90117	5:29:25.9	5.3	28.696	28.696	17.0
90118	6:33:44.5	4.7	36.922	71.300	46.0
90122	10:43:13.8	4.6	36.416	71.124	254.0
90122	12:06:04.1	4.5	36.419	71.134	245.0
90123	10:02:22.2	4.7	42.790	76.880	33
90127	2:04:10.1	4.4	36.972	72.944	33
90165	7:20:52.4	4.8	37.110	72.861	57.0
90165	7:45:00.0	-	37.110	72.861	57.0
90165	14:18:10.6	5.2	47.892	85.050	37.0
90168	4:51:45.5	5.9	27.398	65.719	15.0
90168	17:17:43.1	5.3	27.302	65.548	15.0
90170	14:58:22.5	4.9	35.912	70.338	33
90174	23:35:00.6	4.7	36.452	70.578	205.0
90183	23:47:43.6	5.1	37.194	72.924	33

Table 7 (cont): Events used in the Energy Discriminant Study of GAR					
Julian Date	GMT	Mag.	Latitude	Longitude	Depth
90184	12:18:08.7	4.7	37.213	72.828	33
90184	18:22:10.1	4.7	37.233	71.689	33
90186	1:26:10.5	4.1	37.676	69.569	33
90186	1:36:15.3	4.3	37.740	71.390	33
90187	19:34:52.4	5.3	36.861	49.303	35.0
90207	6:53:56.3	5.8	27.247	65.508	19.0
90212	2:52:59.4	4.3	36.615	71.263	228.0
90215	9:15:06.1	6.0	65.508	84.961	33
90215	11:57:13.0	5.0	32.758	48.213	45.0
90215	14:50:03.2	4.7	40.283	70.861	33
90226	0:50:39.2	5.2	27.024	65.969	21.0
90237	12:25:04.9	4.7	40.156	63.152	33
90237	14:50:12.3	4.4	40.205	63.129	33
90242	12:19:25.5	4.9	40.277	77.138	54.0
90244	21:32:49.8	4.7	39.375	74.760	17.0
90246	2:40:59.1	4.9	36.409	70.671	202.0
90247	10:59:17.8	4.6	34.870	70.902	33
90251	19:33:18.8	5.5	27.500	66.092	28.0
90256	19:07:49.1	4.8	43.894	81.779	33
90284	13:57:05.1	5.3	32.838	48.212	46.0
90294	10:56:30.8	4.7	37.635	72.131	33
90297	23:38:15.1	5.2	44.117	83.856	20.0
90297	23:46:57.6	5.3	44.119	83.876	33
88258	4: 0: 0.0	6.3	49.87	78.8	JVE
90228	4:59:57.6	6.2	41.564	88.770	LN

Table 8: Events used in the Energy Discriminant Study of the Tibet PASSACL Array					
Julian Date	GMT	Mag.	Latitude	Longitude	Depth
91193	22:06:00.2	4.8	39.420	94.830	16.0
91231	6:05:51.3	5.5	46.944	85.302	30.0
91245	11:05:50.4	5.5	37.440	95.402	10.0
92109	18:19:29.2	4.1	36.150	92.540	10.0
92142	4:59:58.0	6.5	41.662	88.729	LN

Table 9: Events recorded by PAKN, KNET, AAK, and
NIL, and used in the energy discriminant study

Julian Date	GMT	Mag.	Latitude	Longitude	Depth	Recording Stations
92136	8: 8: 2.9	6.2	41.019	72.429	50.0	KNET
92276	14:38:44.3	4.9	38.006	73.044	118.0	PAKN,KNET
92289	2:42: 6.3	4.6	39.212	72.798	16.0	PAKN,KNET
92289	19:42:11.8	4.6	38.134	74.265	135.0	PAKN,KNET
92292	16:14:45.5	5.1	42.066	73.116	19.0	PAKN
92301	2:54:35.0	4.5	37.977	73.643	167.0	PAKN
92307	4:52:52.9	4.8	37.228	71.990	128.0	PAKN
92310	9:21:56.5	4.4	36.494	70.374	200.0	PAKN
92311	7:21:57.8	5.1	41.051	72.518	40.0	PAKN,KNET
92311	11:47:42.9	4.6	34.584	79.921	12.0	PAKN
92311	17:58:38.0	4.5	34.532	69.394	33	PAKN
92313	20:50: 3.0	5.3	38.778	69.864	64.0	PAKN
92317	20:41: 4.6	5.7	36.446	70.852	198.0	PAKN
92322	2:38:50.1	5.3	33.782	67.574	36.0	PAKN,KNET
92322	2:38:50.1	5.3	33.782	67.574	36.0	PAKN,KNET
92328	23:11: 6.7	5.6	38.620	72.635	41.0	PAKN,KNET
92330	4:46: 8.1	4.5	37.303	71.641	196.0	PAKN
92331	22:57:13.5	4.1	36.620	71.388	189.0	PAKN
92339	11:36:36.2	5.9	37.814	72.194	120.0	PAKN
92341	3:44:29.9	5.5	37.810	72.186	128.0	PAKN
92359	5: 9:47.4	5.2	42.221	72.225	38.0	KNET
93364	14:24: 4.5	5.7	44.735	78.793	15.0	KNET
94012	10:22:51.3	5.3	39.247	75.493	28.0	KNET
94121	21:17:20.7	5.2	39.126	71.621	33	KNET
94353	2:24:15.7	4.9	39.574	79.516	28.0	NIL
94353	3:22:17.8	4.1	34.032	72.060	33	NIL
94358	23:51:47.9	5.3	38.588	73.897	33	NIL
94359	0:35:45.0	4.0	38.588	73.897	-	NIL
94360	14:48: 1.4	5.3	36.469	71.244	226.0	NIL
94360	20:34:25.6	4.5	36.535	70.969	195.0	NIL
94363	16: 1:18.2	5.5	35.655	80.663	33	NIL
95003	1:31:14.7	4.5	39.816	78.178	33	NIL,AAK
95003	23:32:44.0	4.9	38.761	68.735	33	NIL,AAK
95003	1:31:14.7	4.5	39.816	78.178	33	NIL,AAK
95003	23:32:44.0	4.9	38.761	68.735	33	NIL,AAK
95006	5:23:49.4	4.0	36.24	71.60	33	NIL
95006	5:57:45.2	0.0	36.24	71.60	33	NIL
95007	15:57:58.6	4.6	36.370	70.687	208.0	NIL,AAK
95008	19:24:57.9	5.4	36.542	71.351	206 0	NIL,AAK
95010	8:11:28.5	4.1	37.176	71.611	100.0	NIL,AAK

Table 9b (cont.): Events recorded by PAKN, KNET, AAK,
and NIL, and used in the energy discriminant study

Julian Date	GMT	Mag.	Latitude	Longitude	Depth	Recording Stations
95011	2:47:58.9	4.3	35.88	70.92	33	NIL
95017	16: 7:34.1	4.1	36.199	71.266	33	NIL
95017	18: 9: 8.9	4.0	36.170	68.876	144.0	NIL,AAK
95017	22:15:49.5	4.6	34.656	70.765	27.0	NIL,AAK
95018	0:18:15.2	4.5	36.363	69.633	171.0	NIL,AAK
95018	14:38:57.7	4.5	36.517	71.269	217.0	AAK
95027	17:20: 5.3	4.2	28.977	81.475	33	NIL
95026	7: 0:45.0	5.2	36.147	71.255	106.0	NIL
95026	11:36:51.8	4.2	39.711	77.051	33	NIL
95029	1:20:10.8	5.2	36.920	71.635	109.0	NIL
95030	3: 6:56.7	4.1	29.286	82.217	52.0	NIL
95030	22:36:31.5	4.9	36.315	71.446	77.0	NIL
95030	13:56:46.9	4.0	28.349	82.457	81.0	NIL,AAK
95031	3:15:21.2	4.1	38.20	72.27	33	NIL
95033	19:34:49.4	4.6	39.322	67.493	33	NIL,AAK
95035	7:10:44.4	4.2	31.105	81.714	33	NIL
95035	9:41: 6.5	4.1	37.63	72.35	200.0	NIL
95035	21:52:37.2	4.4	38.241	70.651	33	NIL,AAK
95035	22:59: 7.0	4.1	37.34	69.84	33	NIL,AAK
95036	3:53:44.1	4.3	36.478	70.462	208.0	NIL,AAK
95036	8: 5:43.3	4.8	37.347	71.807	33	NIL
95038	20:36: 0.9	4.1	37.139	72.049	176.0	NIL,AAK
95041	7:49:19.4	4.6	36.186	69.111	44.0	NIL,AAK
95041	8:17:48.5	4.6	36.082	69.122	33	NIL,AAK
95042	6: 1:11.1	4.1	36.165	69.070	33	NIL,AAK
95046	2:58:52.6	4.7	36.167	71.364	119.0	NIL,AAK
95046	17: 5:20.6	4.1	36.398	70.412	205.0	NIL,AAK
95048	12:11:49.7	4.8	37.575	71.361	33	NIL,AAK
95049	20:25: 3.2	4.4	36.589	71.316	33	NIL,AAK
95051	4:12:23.2	5.4	39.167	71.118	26.0	NIL, KNET
95051	8: 7:34.2	5.0	41.073	72.451	39.0	NIL, KNET
95053	5:42:51.7	4.2	29.751	68.508	33	NIL
95056	4:14: 6.4	4.8	36.993	72.188	205.0	AAK
95056	9:42:23.8	4.8	39.880	77.525	33	NIL, AAK
95056	11: 5:32.3	4.7	36.536	71.004	183.0	NIL, AAK
95056	15:44:42.8	4.1	40.152	69.315	33	NIL, AAK
95058	0:19: 8.5	4.4	37.524	71.840	33	NIL
95059	10:24:13.9	4.9	37.962	73.180	141.0	NIL
95060	5:45:55.3	4.2	37.230	71.966	200.0	NIL
95061	22: 3:20.7	4.0	40.60	73.90	33	NIL
95063	14: 3:56.8	3.9	36.83	71.24	200.0	NIL

Table 9c (cont.): Events recorded by PAKN, KNET, AAK,
and NIL, and used in the energy discriminant study

Julian Date	GMT	Mag.	Latitude	Longitude	Depth	Recording Stations
95064	8:14:52.7	3.9	35.837	69.871	200.0	NIL
95067	6:27:26.1	4.1	35.832	69.747	150.0	NIL
95067	14:56:48.7	4.0	37.50	72.36	197.0	NIL
95068	21:33:28.5	4.3	37.717	72.485	100.0	NIL
95069	12: 2:24.0	4.2	36.327	70.846	132.0	NIL
95071	9:21:52.1	2.8	29.74	36.17	10.0	NIL
95072	8:25: 4.9	4.7	37.466	72.040	33	NIL
95072	22:56:23.0	4.5	37.042	71.924	133.0	NIL
95075	3:27: 2.3	4.8	30.127	67.569	29.0	NIL
95077	14:10:47.7	4.5	37.389	71.781	64.0	NIL, AAK
95077	18: 2:36.6	5.3	42.422	87.199	22.0	AAK only
95078	16:58:14.1	4.5	36.419	70.813	192.0	NIL, AAK
95080	7:43:57.3	4.3	36.392	71.267	231.0	NIL, AAK
95081	0:44:46.9	4.3	36.433	70.223	230.0	NIL, AAK
95081	19:34:52.8	4.4	41.272	73.240	33	NIL, AAK
95082	8: 7:51.5	3.8	32.889	68.143	33	NIL
95083	0:50:55.5	4.1	36.470	71.221	231.0	NIL, AAK
95083	2:39:17.0	4.1	33.10	70.46	41.0	NIL
95083	11:52:32.9	4.9	32.564	75.998	33	NIL
95083	21: 1:57.4	4.5	37.308	71.635	33	NIL, AAK
95088	15:52:36.7	4.2	41.827	79.455	33	NIL, AAK
95090	6:35:44.2	4.4	38.958	71.046	33	NIL, AAK
95094	15:29:53.9	4.5	28.01	71.54	18.7	AAK
95114	17:59:41.3	4.0	43.51	84.44	33	NIL, AAK
95122	11:48:08.4	5.3	43.87	84.89	33	NIL, AAK
95139	11:45:38.3	4.0	41.47	92.73	10.7	NIL, AAK
95148	21:46:52.8	4.4	47.65	85.66	33	NIL, AAK
95151	13:51:17.6	5.1	30.27	68.00	33	NIL, AAK
95162	8:26:31.6	4.0	29.78	67.82	33	NIL, AAK
95162	22:03:46.5	4.3	32.52	69.67	33	NIL, AAK
95197	23:36:47.9	4.6	29.90	69.43	33	AAK
95197	23:54:10.1	4.1	39.86	71.43	33	AAK
95209	14:52:23.3	4.5	31.58	69.34	33	NIL, AAK
95281	8:55:49.9	5.9	40.989	72.118	48.0	KNET
95135	04:05:59.6	5.7	41.63	88.87	LN	NIL, AAK
95214	11:59:44.2	3.9	41.45	88.27	LN	NIL, AAK
95229	0:59:59.3	5.5	41.60	88.86	LN	NIL, AAK
96160	2:55:59.4	5.7	41.65	88.76	LN	NIL, AAK
96211	1:48:59.1	4.7	41.69	88.35	LN	AAK

Table 10: Events recorded by ABKT used
in the energy discriminant study

Julian Date	GMT	Mag.	Latitude	Longitude	Depth
95003	23:32:44.0	4.3	38.761	68.735	33.0
95004	0:57:51.6	4.5	41.285	48.874	33.0
95063	21:36:14.9	4.1	36.236	69.031	314.0
95064	8:14:52.7	3.9	35.837	69.871	200.0
95067	6:27:26.1	4.1	35.832	69.747	150.0
95067	7:38: 8.5	4.2	34.223	46.563	21.0
95067	7:58: 1.9	4.3	31.614	50.493	33.0
95081	0:44:46.9	4.3	36.433	70.223	230.0
95081	6:28:36.8	4.8	30.209	51.040	79.0
95082	8: 7:51.5	3.8	32.889	68.143	85.0
95084	11:23:27.9	4.6	33.834	47.905	33.0
95121	5:31:50.6	4.4	33.331	48.771	33.0
95125	2:40:28.4	4.5	35.880	68.824	33.0
95125	3: 6:53.5	4.4	36.017	69.508	160.0
95133	7:20:43.2	4.8	40.678	50.592	53.0
95134	4:47: 0.1	4.8	39.883	69.728	34.0
95135	0:16:52.5	4.8	38.468	49.435	119.0
95135	0:21:54.7	4.5	38.54	49.29	33.0
95145	9: 5: 2.0	4.4	40.017	70.190	43.0
95147	8:34:38.3	4.6	30.488	50.817	51.0
95147	21:21:31.9	4.8	39.028	48.944	33.0
95154	20: 8:33.1	4.0	35.927	53.124	33.0
95154	23:17:21.7	4.2	28.420	55.193	33.0
95158	10: 4: 6.3	4.3	31.989	49.234	33.0
95158	23: 9:47.0	4.6	32.461	48.737	21.0
95159	7:32:15.9	4.4	28.275	55.332	33.0
95159	20:21: 9.5	4.4	32.36	49.05	33.0
95164	15:55: 0.8	4.5	36.419	69.654	33.0
95165	5:42:33.3	4.5	36.585	58.598	33.0
95166	3: 1:35.7	4.2	31.60	49.85	280.0
95166	18:37:28.0	4.6	38.446	69.928	90.0
95168	5:57:27.5	4.0	36.870	68.659	33.0
95177	21:12:55.8	4.1	36.560	51.196	33.0
95177	23:27:38.8	4.4	39.873	48.344	67.0
95178	0:46:46.3	4.3	39.900	48.372	74.0
95186	14:56:31.8	4.3	36.324	69.969	204.0
95187	16:45:10.7	4.0	38.664	49.411	33.0
95191	1:54:55.7	4.3	30.964	50.028	33.0

Table 10(cont.): Events recorded by ABKT used
in the energy discriminant study

Julian Date	GMT	Mag.	Latitude	Longitude	Depth
95195	14: 3: 6.6	4.2	42.81	48.97	53.0
95201	4:20:52.8	4.5	35.874	69.978	33.0
95201	20:44:24.5	4.3	31.494	68.675	33.0
95202	1:48:18.3	4.4	32.504	49.906	61.0
95204	11:28: 6.7	4.3	39.460	69.210	54.0
95217	16:46:56.1	4.1	31.43	49.65	33.0
95225	0:57:23.4	3.9	36.403	69.626	110.0
95228	2:16:50.6	3.9	37.12	70.41	33.0
95229	18: 9:58.7	4.5	38.961	48.908	74.0
95230	4:24:36.6	4.3	41.542	48.672	61.0
95237	1:53:51.7	4.0	35.655	68.688	33.0
95237	10:53: 1.4	4.9	28.417	57.116	79.0
95243	3:18: 3.5	4.1	37.145	69.138	41.0
95245	20:48:57.2	3.9	36.421	69.222	245.0
95247	12:10:20.6	4.2	39.82	51.25	33.0
95247	17:47: 9.5	4.4	29.995	57.486	33.0
95256	1:37:20.4	4.0	37.423	69.543	33.0
95265	4:16:33.3	3.8	36.341	70.037	172.0
95265	12:56:23.7	3.9	37.320	58.706	33.0

Kearsarge, Lee Vining and Little Skull Mtn at PAS

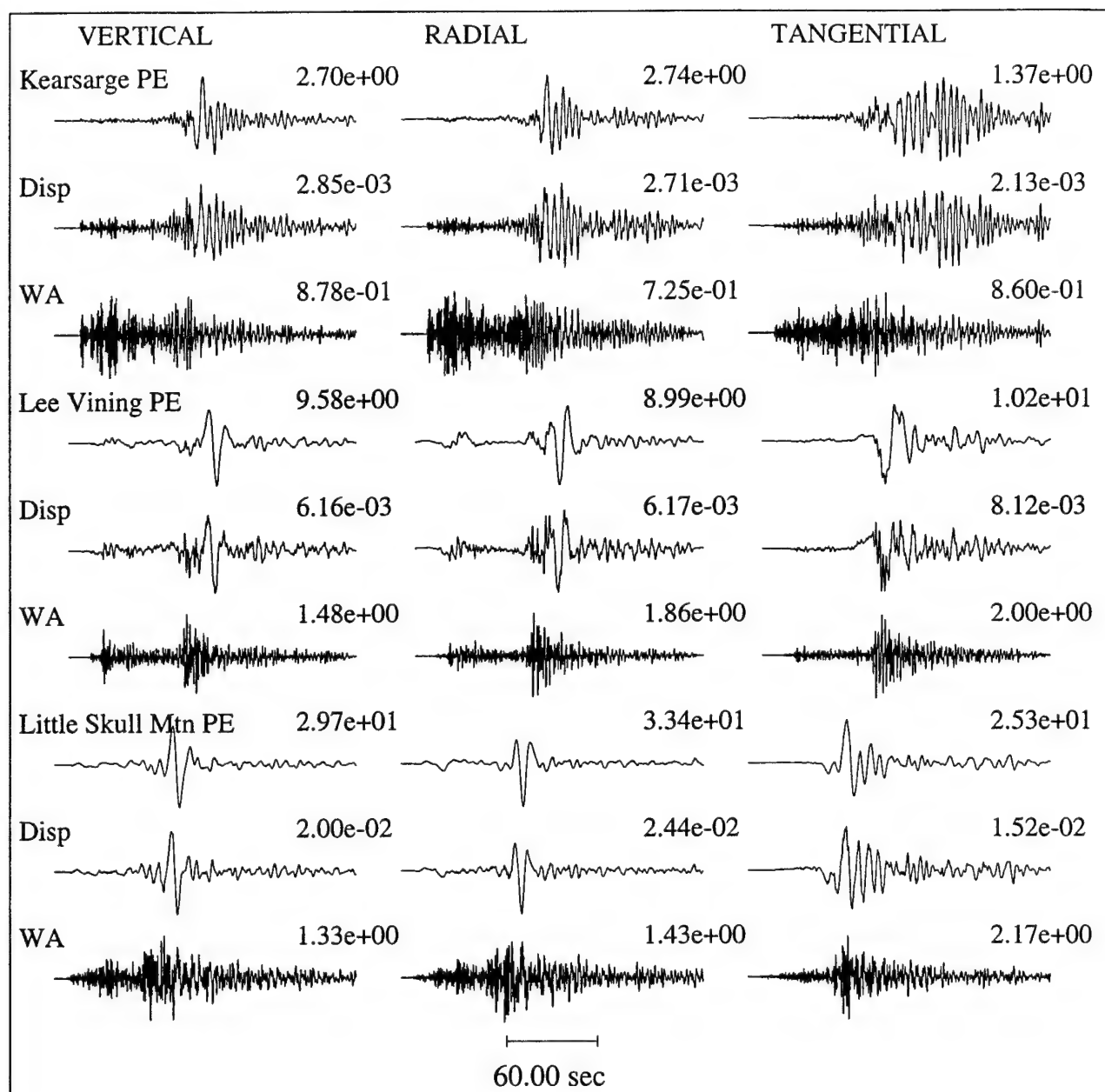


Figure 1. (after Woods *et al.*, 1993) Regional waveform comparisons of the U.S. JVE Kearsarge with comparable sized earthquakes (Lee Vining and Little Skull Mountain) at similar distances. Each set of three rows of three-component records is for one event; the first row traces are convolved with a long-period Press-Ewing (PE) instrument, the second row are broadband (BB) displacements, and the third row of traces are convolved with a short-period Wood-Anderson (WA) instrument. The peak amplitude (cm) of each trace is given to its right.

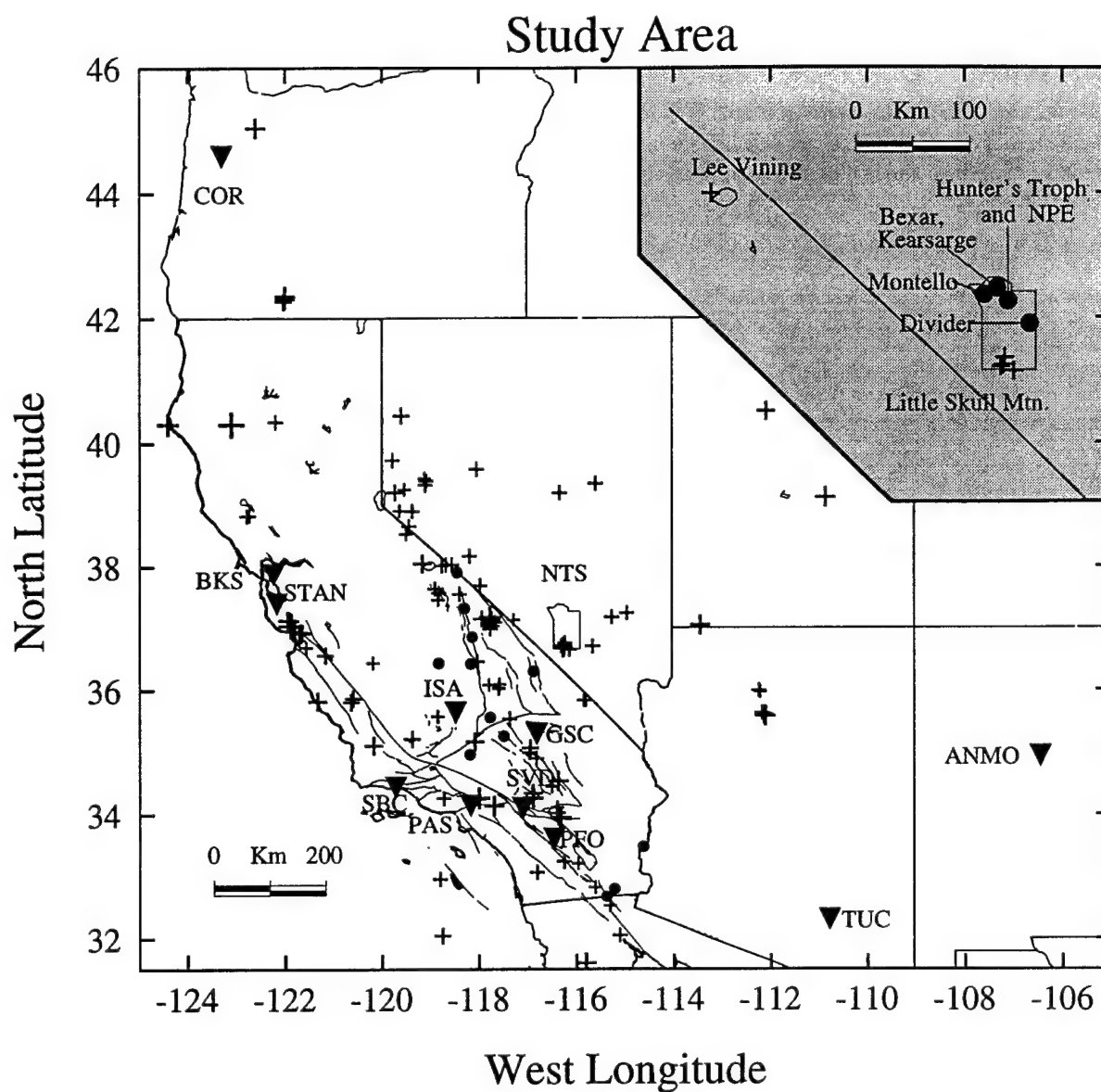


Figure 2. Map showing the stations (upside-down triangles), earthquakes (crosses), small ($M_L < 3.0$) chemical blasts which, along with NTS explosions, comprise the data used to evaluate the energy discriminants. NTS's boundary is outlined. Events used for waveform comparisons in this paper are shown in the shaded blown-up inset with NTS explosions denoted by filled circles.

GSC: Z Comp. Velocity Records and Energy Curves

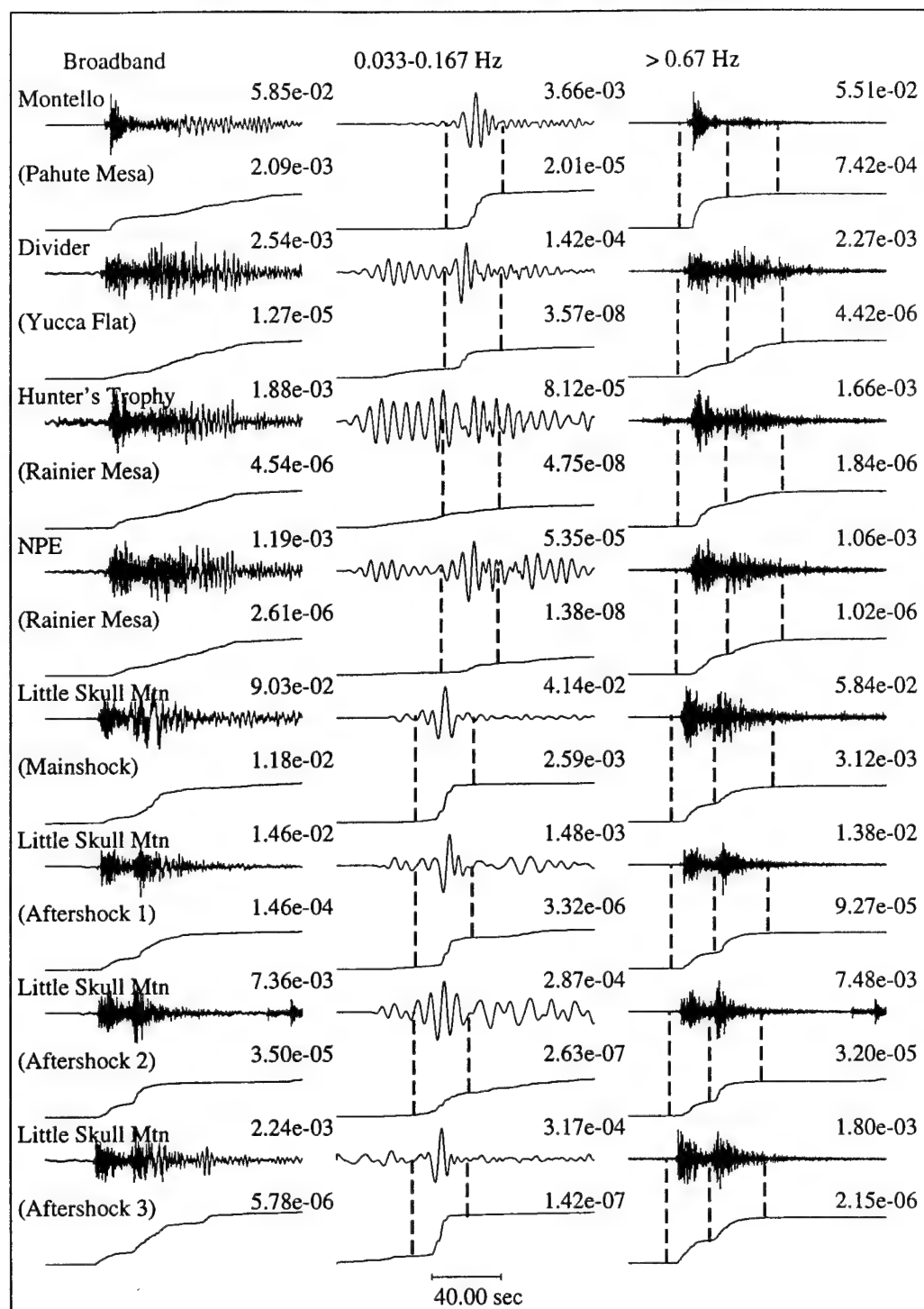


Figure 3. A comparison of vertical-component velocity records for NTS explosions and Little Skull Mountain sequence earthquakes recorded at GSC. The first (left) column is the broadband play-out, followed by the long-period, filtered record in the second (middle) column, and the short-period, filtered record in the third (right) column. Directly beneath each seismogram is its associated integrated energy curve. For the long-period and short-period play-outs the time windows used to measure the integrated energy are denoted by the vertical dashed lines. Each event's identification (and in the case of explosions also the test sub-region) is to the left of the records. Peak ground velocity amplitudes (cm/sec)

ISA: Z Comp. Velocity Records and Energy Curves

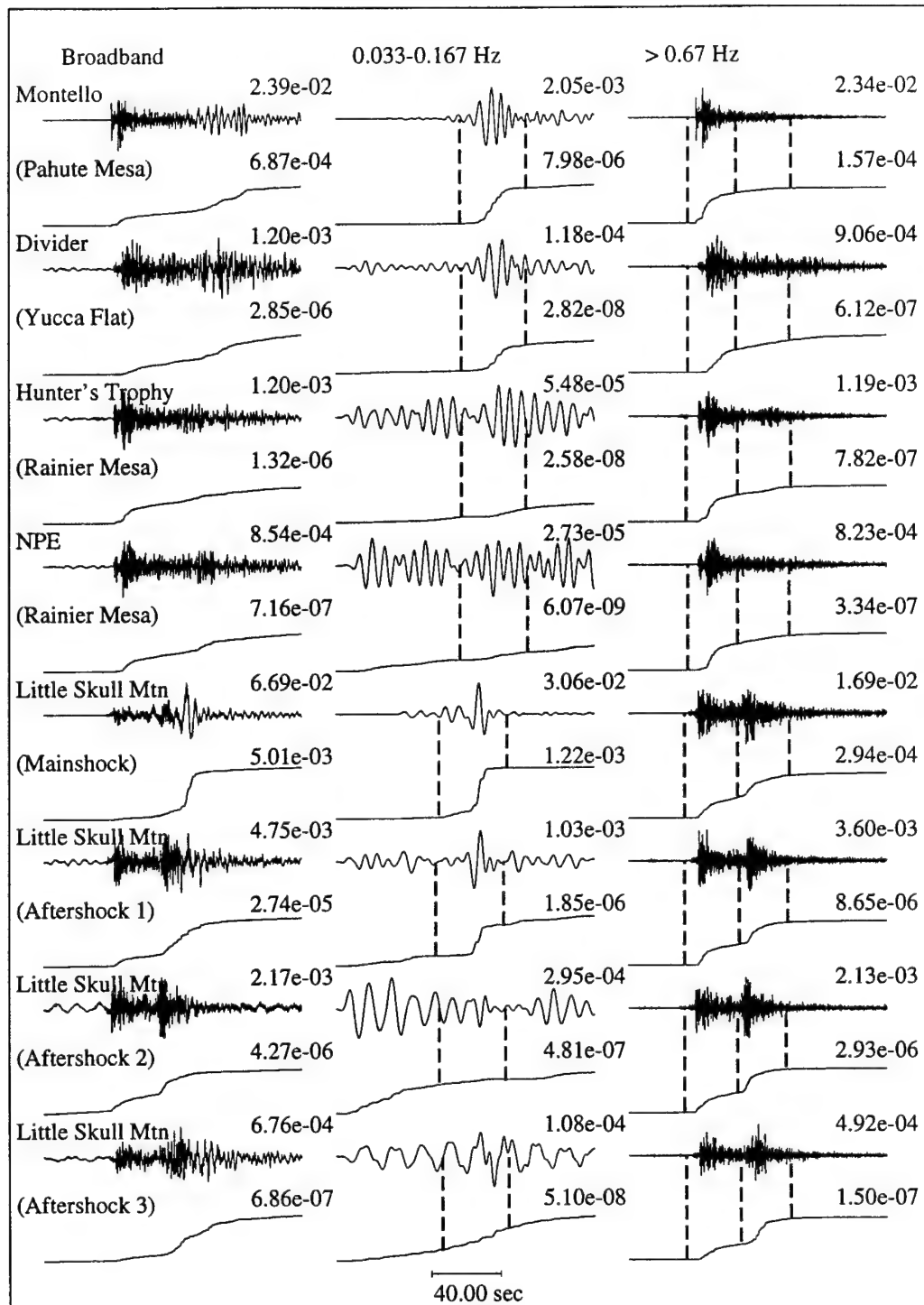


Figure 4. A comparison of vertical-component velocity records for ISA.

PAS: Z Comp. Velocity Records and Energy Curves

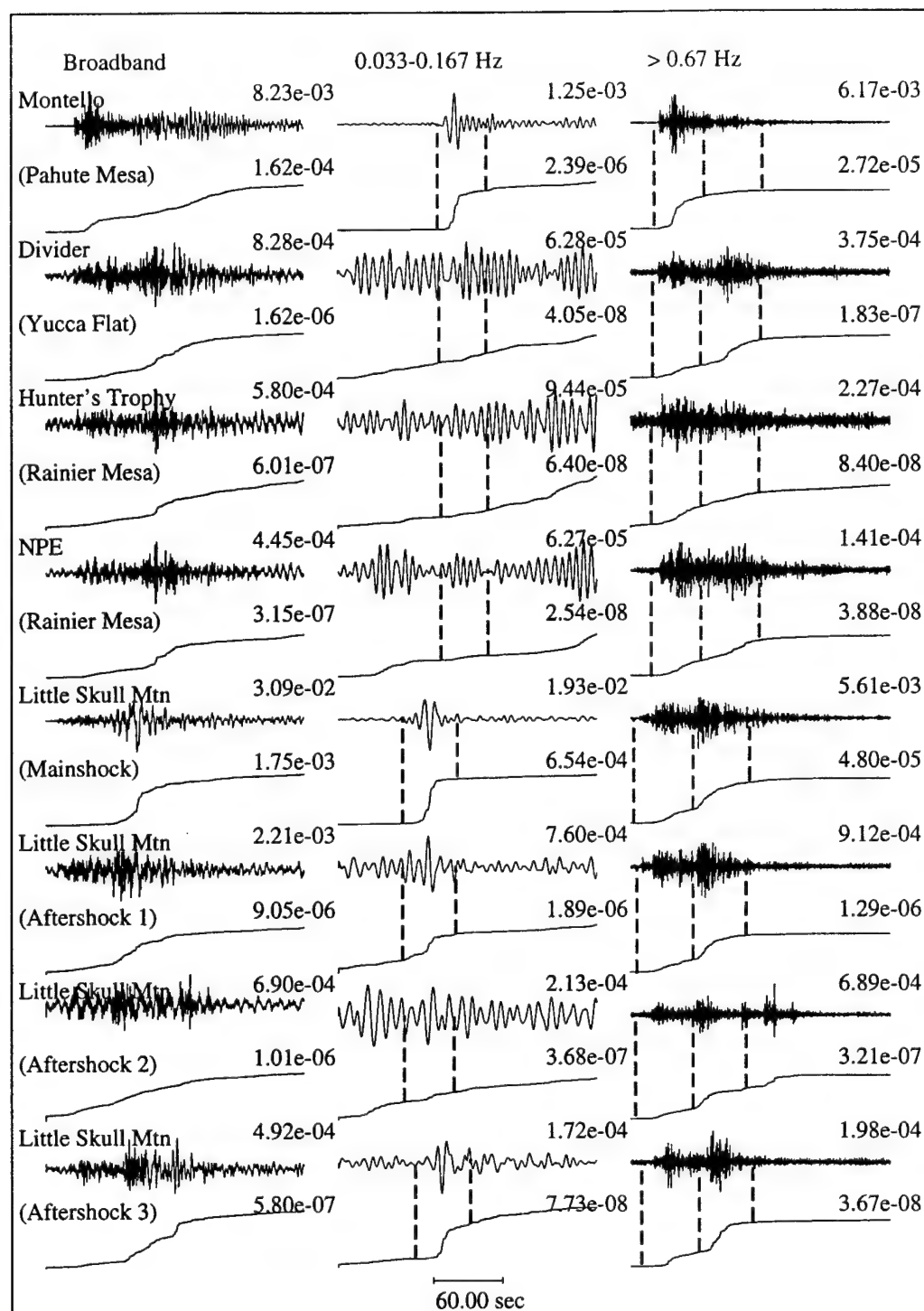


Figure 5. A comparison of vertical-component velocity records for PAS.

PFO: Z Comp. Velocity Records and Energy Curves

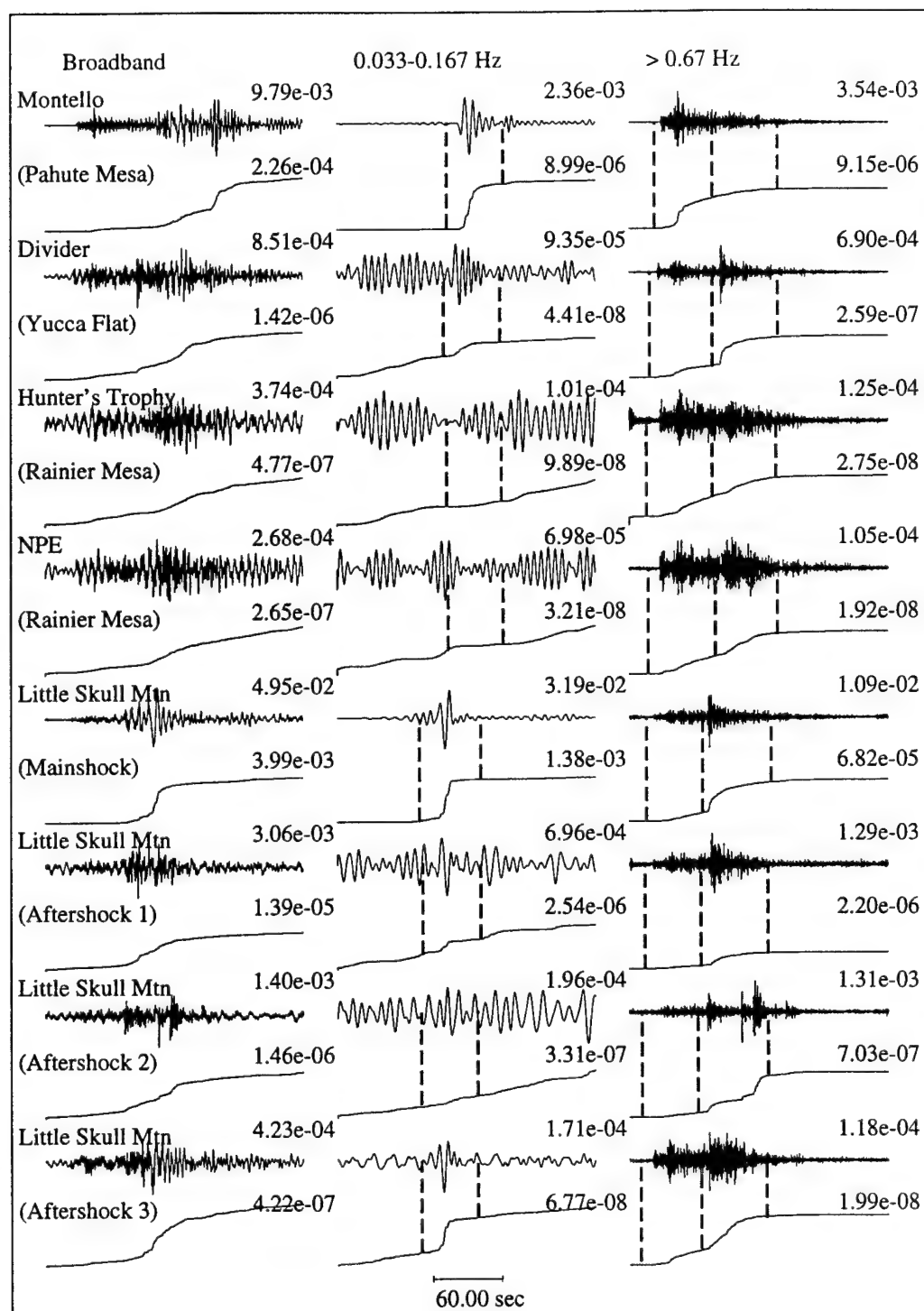


Figure 6. A comparison of vertical-component velocity records for PFO.

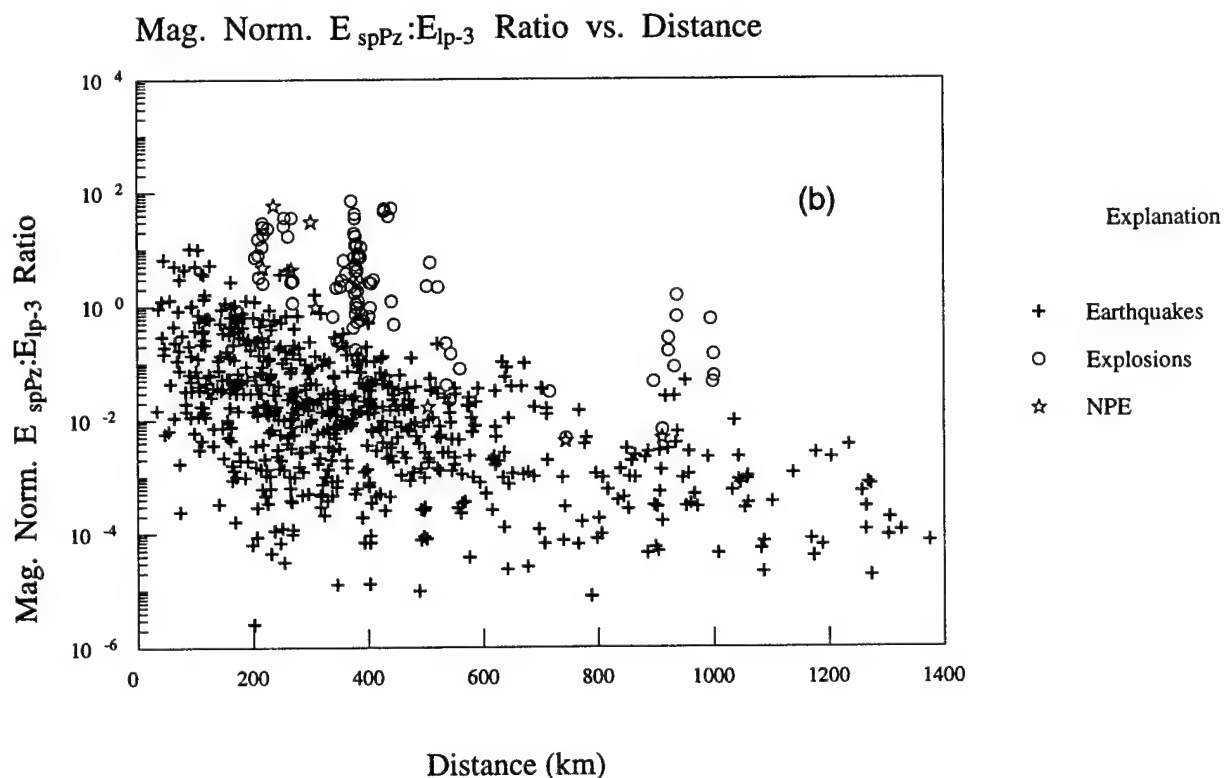
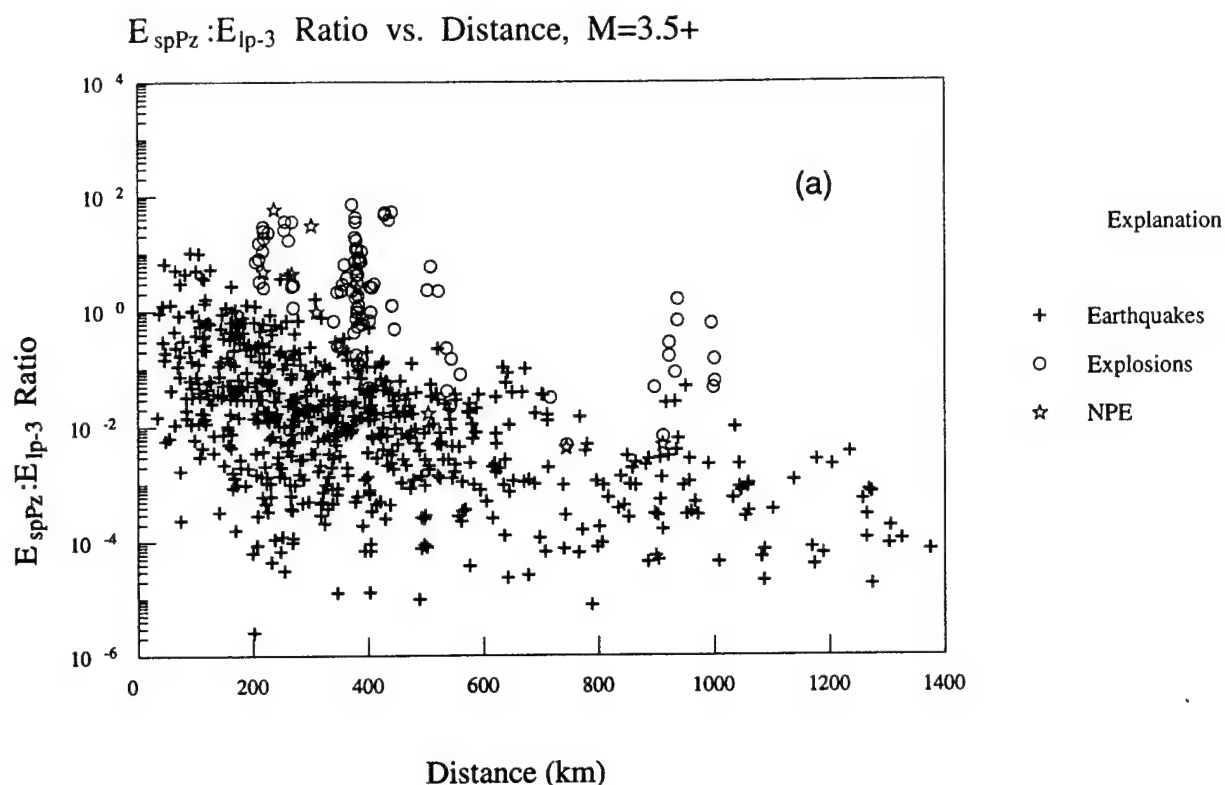


Figure 7. (a) Plot of the short-period:long-period energy ratio (E_{spPz}/E_{lp-3}) vs. distance for $M_L=3.5+$ events. Each datum point represents one source-receiver pair. Earthquakes are represented by crosses and NTS explosion by circles. The NPE shot is denoted by stars. (b) Plot of magnitude normalized energy ratio vs. distance for the same data set.

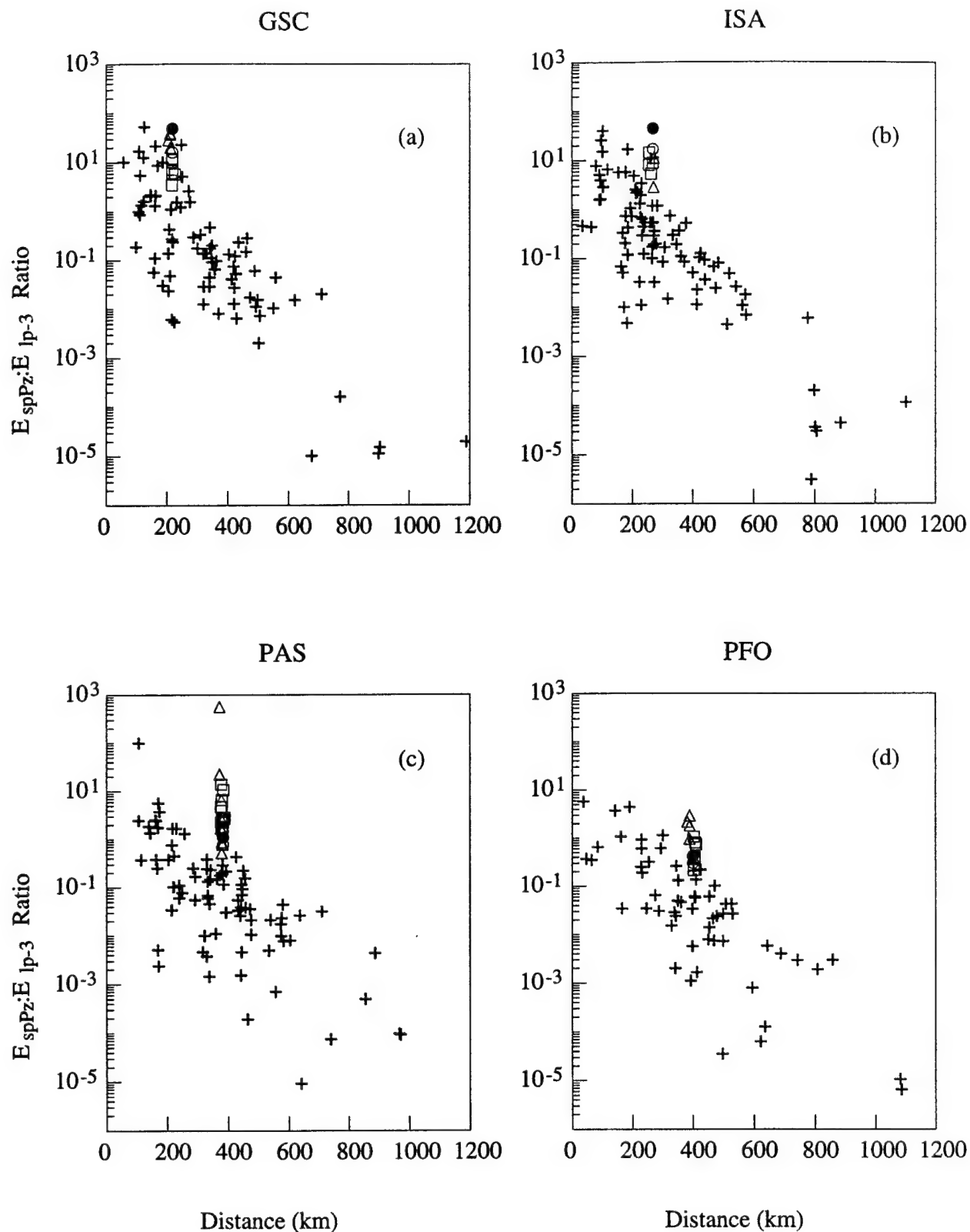


Figure 8. Plots of E_{spPz}/E_{lp-3} vs. distance for the individual stations: (a) GSC, (b) ISA, (c) PAS, and (d) PFO. Crosses denote earthquakes. NTS events are separated by sub-site: Yucca Flat (triangles) Pahute Mesa (squares) and Rainier Mesa (circles). The NPE is denoted by solid circles.

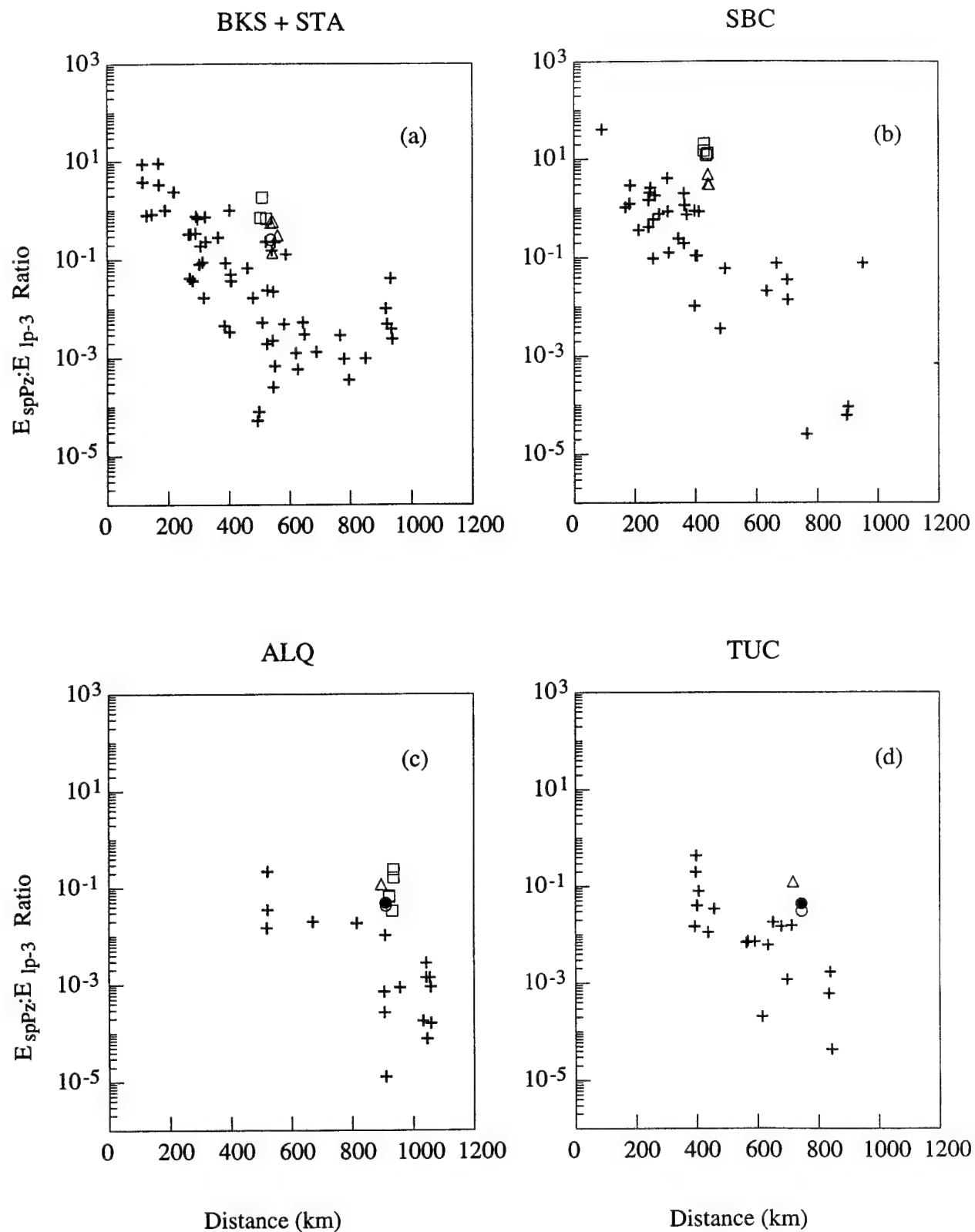


Figure 9. Plots of E_{spPz}/E_{lp-3} vs. distance for the individual stations: (a) BKS and STA, (b) SBC, (c) ALQ, and (d) TUC.

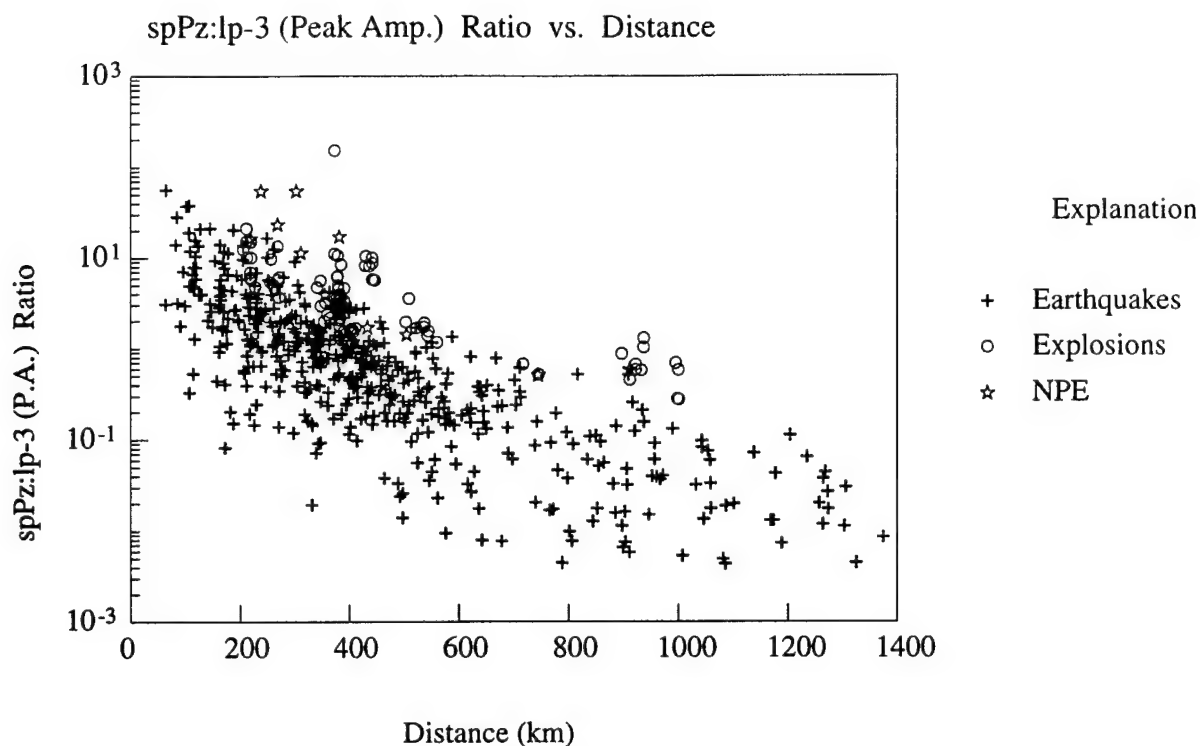


Figure 10. A short-period:long-period discriminant determined from the peak amplitude within the pertinent time window, as opposed to integrated energy (Figure 7).

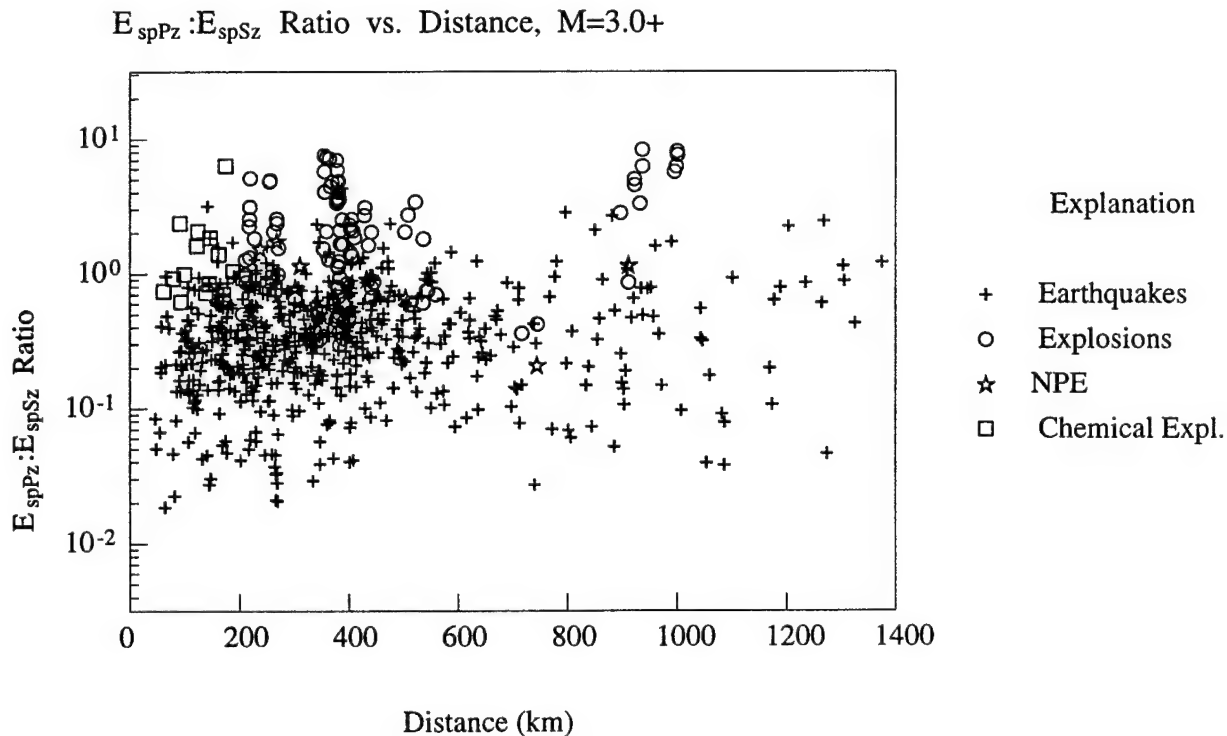


Figure 11. Plot of E_{spPz}/E_{spSz} vs. distance for all events $M \geq 3$ or greater. Crosses represent earthquakes, circles denote nuclear explosions, stars are for the NPE, and squares denote smaller chemical blasts.

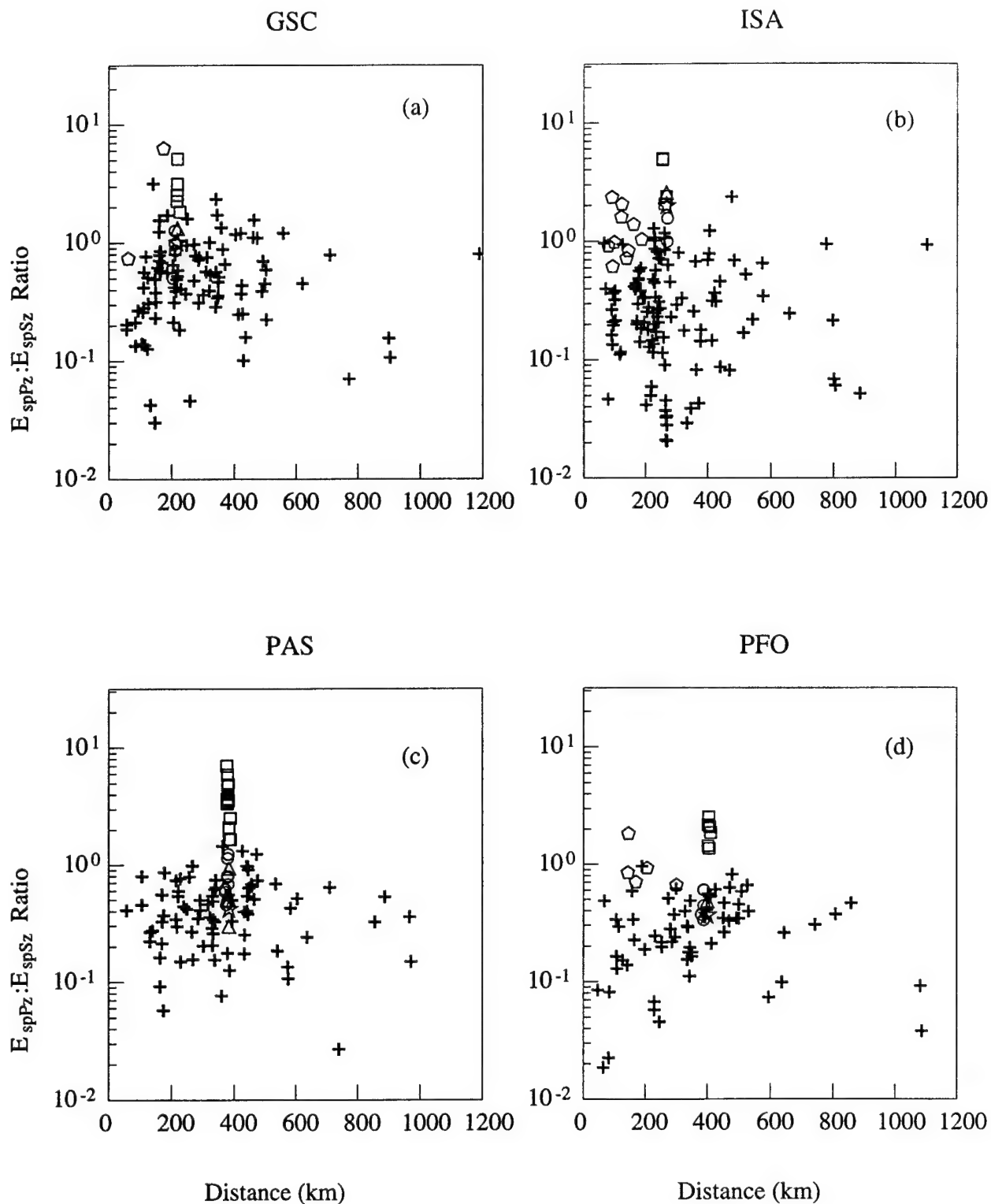


Figure 12. Plots of E_{spPz}/E_{spSz} vs. distance for individual stations: (a) GSC, (b) ISA, (c) PAS, and (d) PFO. Crosses represent earthquakes. NTS events are sorted by sub-site: Yucca Flat (circles), Pahute Mesa (squares), and Rainier Mesa (triangles). The NPE is denoted by stars. Smaller chemical explosions are denoted by pentagons.

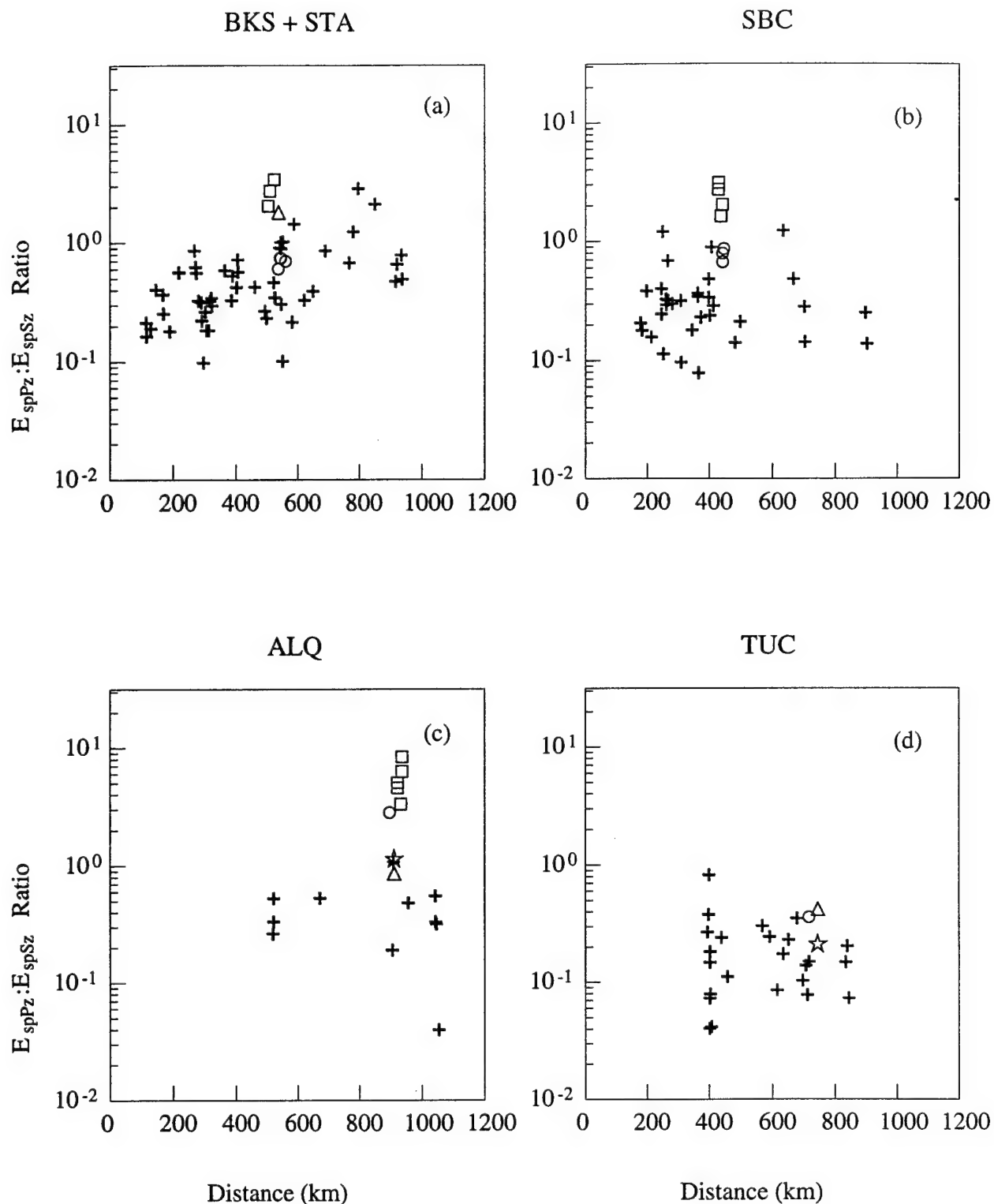


Figure 13. Plots of E_{spPz}/E_{spSz} vs. distance for individual stations: (a) BKS and STA, (b) SBC, (c) ALQ, and (d) TUC. Crosses represent earthquakes. NTS events are plotted as separate symbol types for Yucca Flat (circles), Pahute Mesa (squares), and Rainier Mesa (triangles) shots; the NPE is denoted by stars.

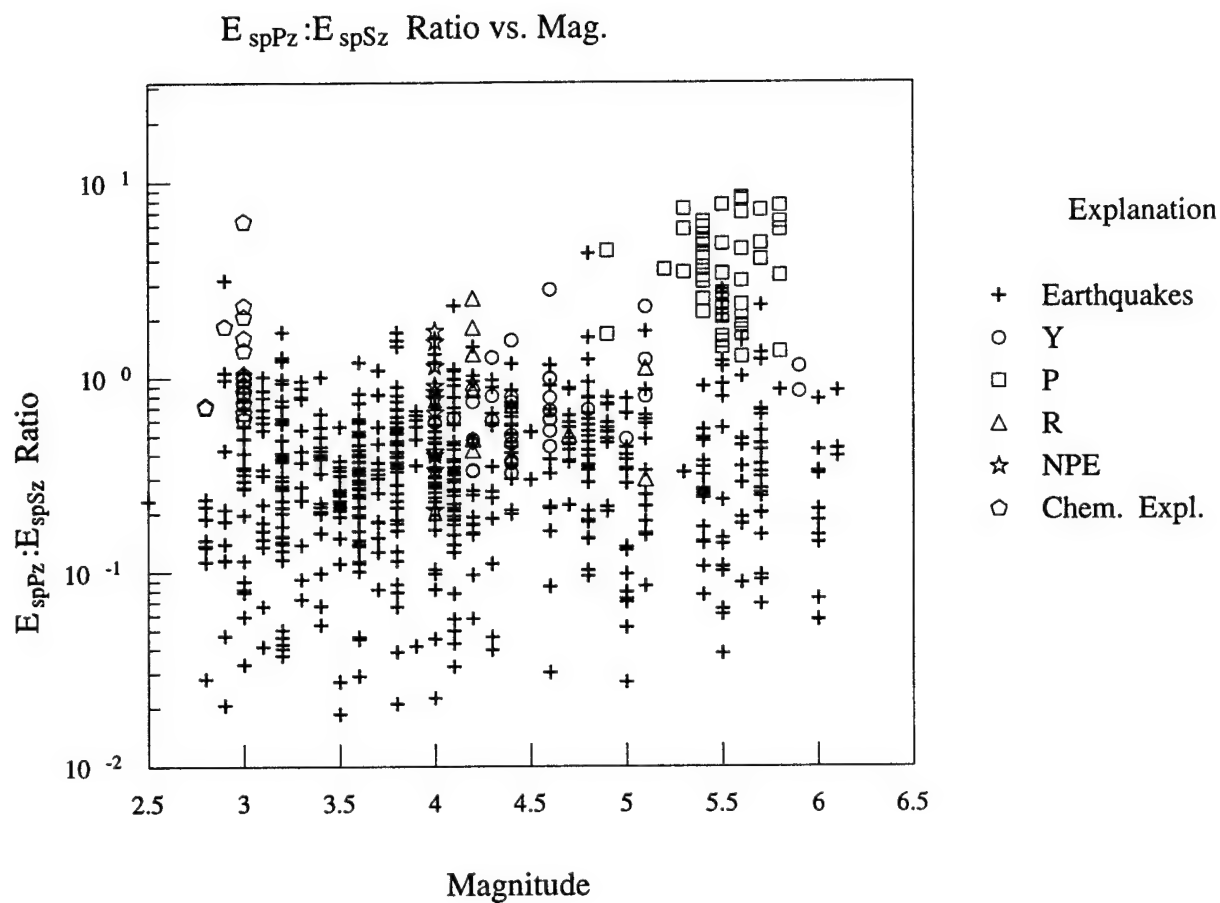


Figure 14. Plot of E_{spPz}/E_{spSz} vs. magnitude. Crosses represent earthquakes. NTS events are plotted as separate symbol types for Yucca Flat (circles), Pahute Mesa (squares), and Rainier Mesa (triangles) shots. The NPE is denoted by stars. Smaller chemical explosions are denoted by pentagons.

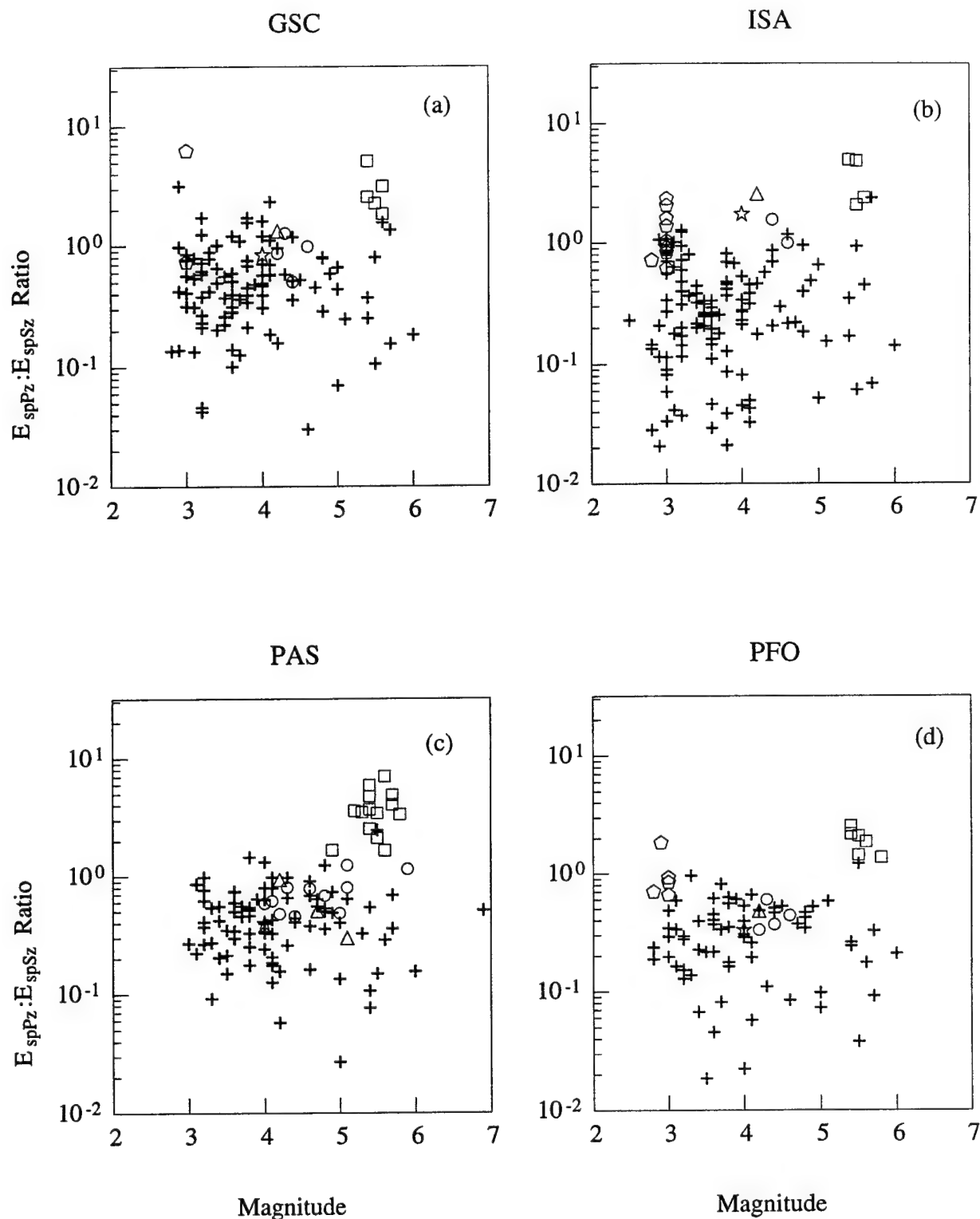


Figure 15. Plots of E_{spPz}/E_{spSz} vs. magnitude for individual stations: (a) GSC, (b) ISA, (c) PAS, and (d) PFO. Crosses represent earthquakes. NTS events are plotted as separate symbol types for Yucca Flat (circles), Pahute Mesa (squares), and Rainier Mesa (triangles). The NPE is denoted by stars. Smaller chemical explosions are denoted by pentagons.

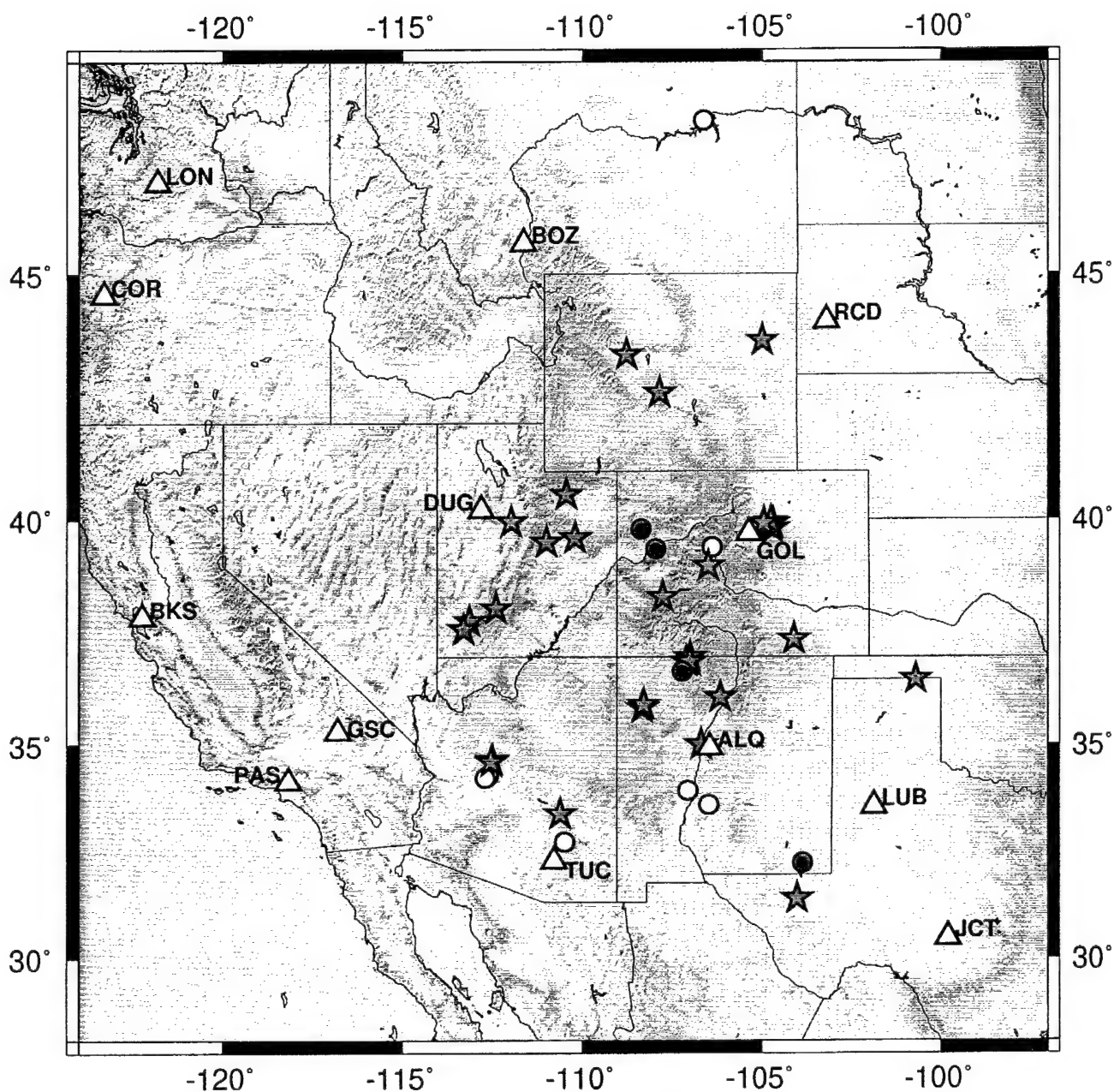


Figure 17. Map of the study area showing analog-recorded events for which SP:LP and SP-P:S peak amplitude ratios were determined. WWSN recording stations used are denoted by white triangles. Earthquakes are red stars, PNE's are blue circles, and chemical explosions are yellow circles.

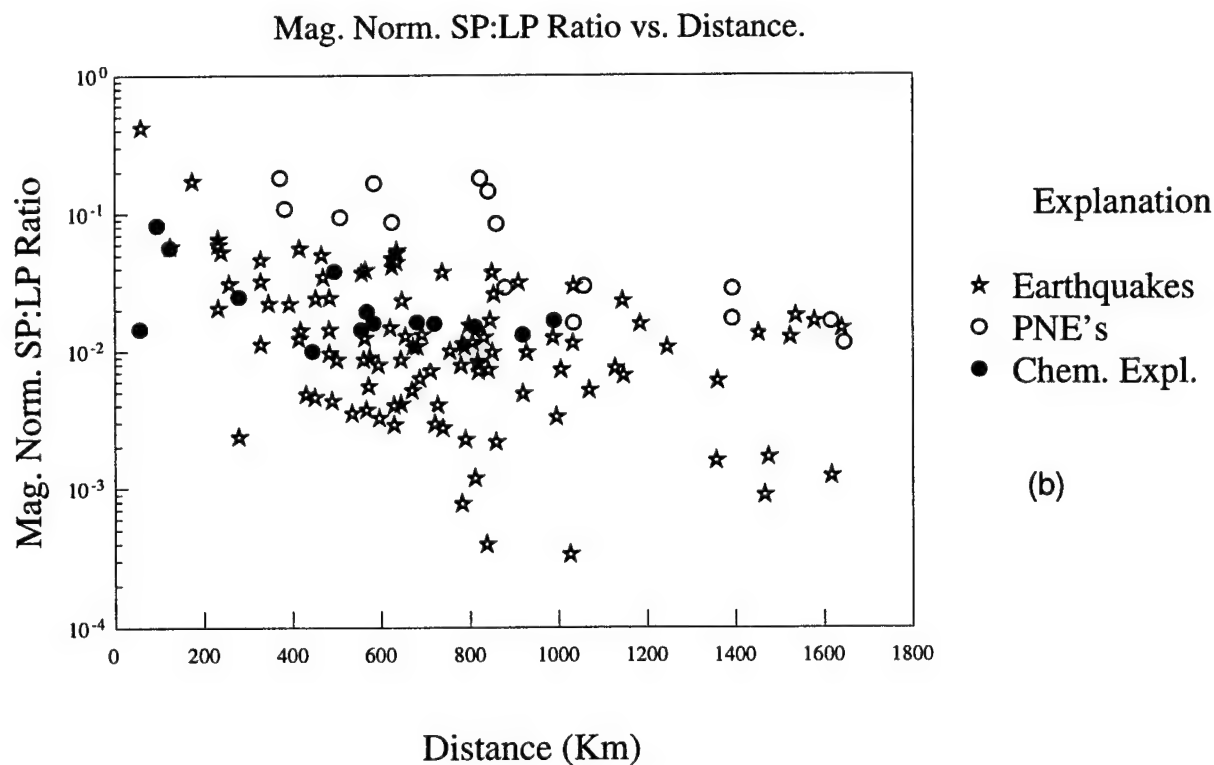
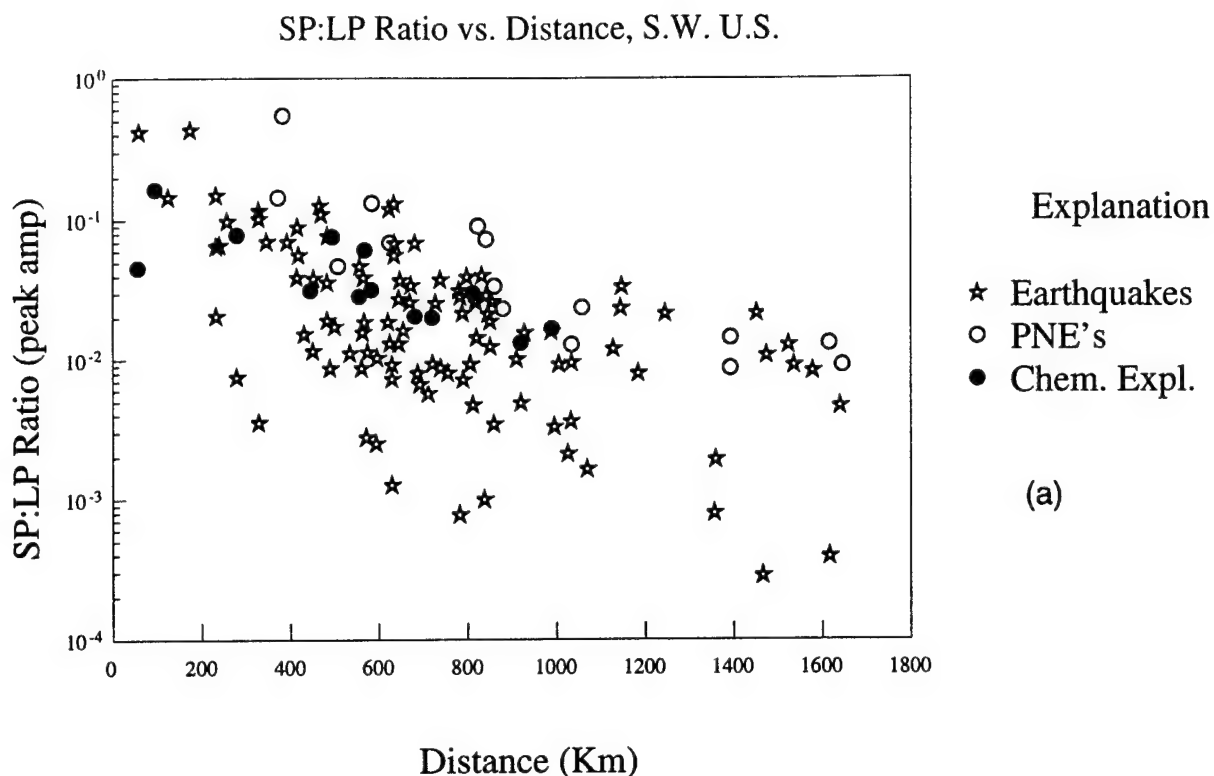


Figure 18. (a) SP:LP (peak amplitude) ratios of analog data for the S.W. U.S. and (b) magnitude-normalized SP:LP ratios for the same data set. Earthquakes are denoted by stars, and PNE's and chemical explosions are denoted by open and solid circles, respectively.

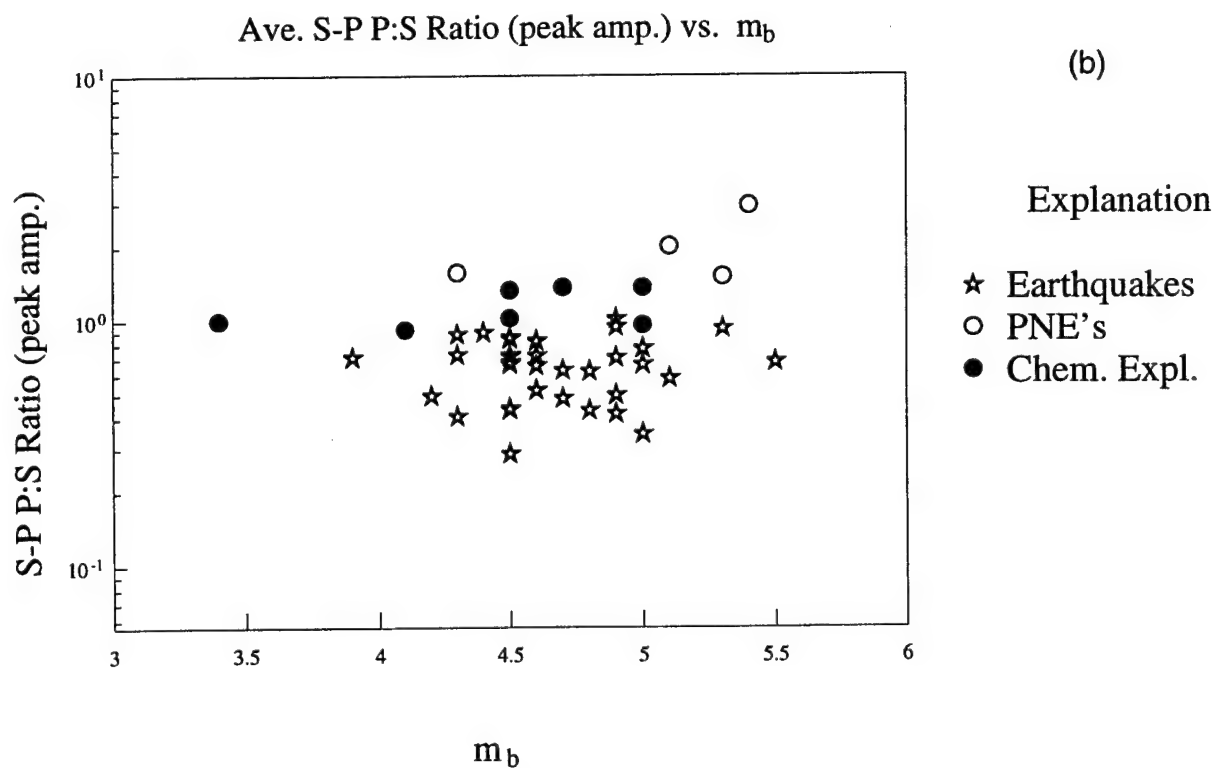
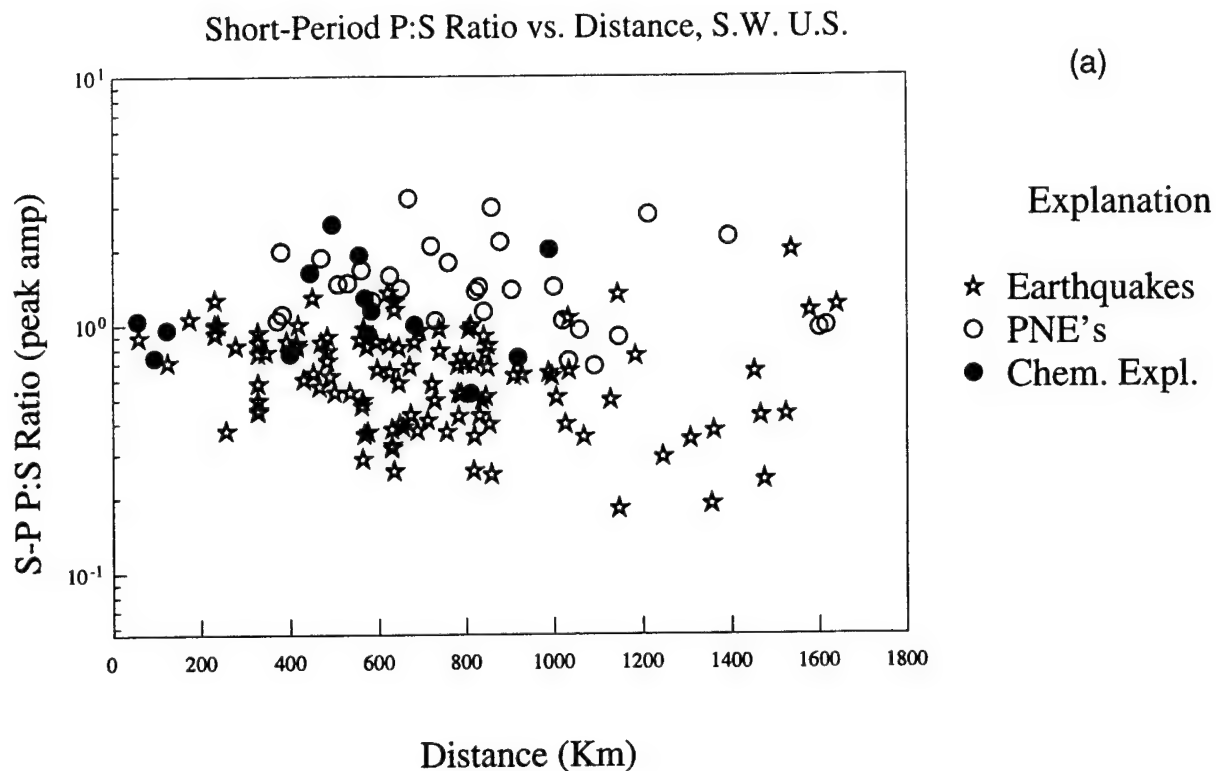


Figure 19. (a) SP-P:S (peak amplitude) ratios of analog data for the S.W. U.S. Earthquakes are denoted by stars, and PNE's and chemical explosions are denoted by open and solid circles, respectively. (b) Network averaged SP-P:S ratios for the same data.

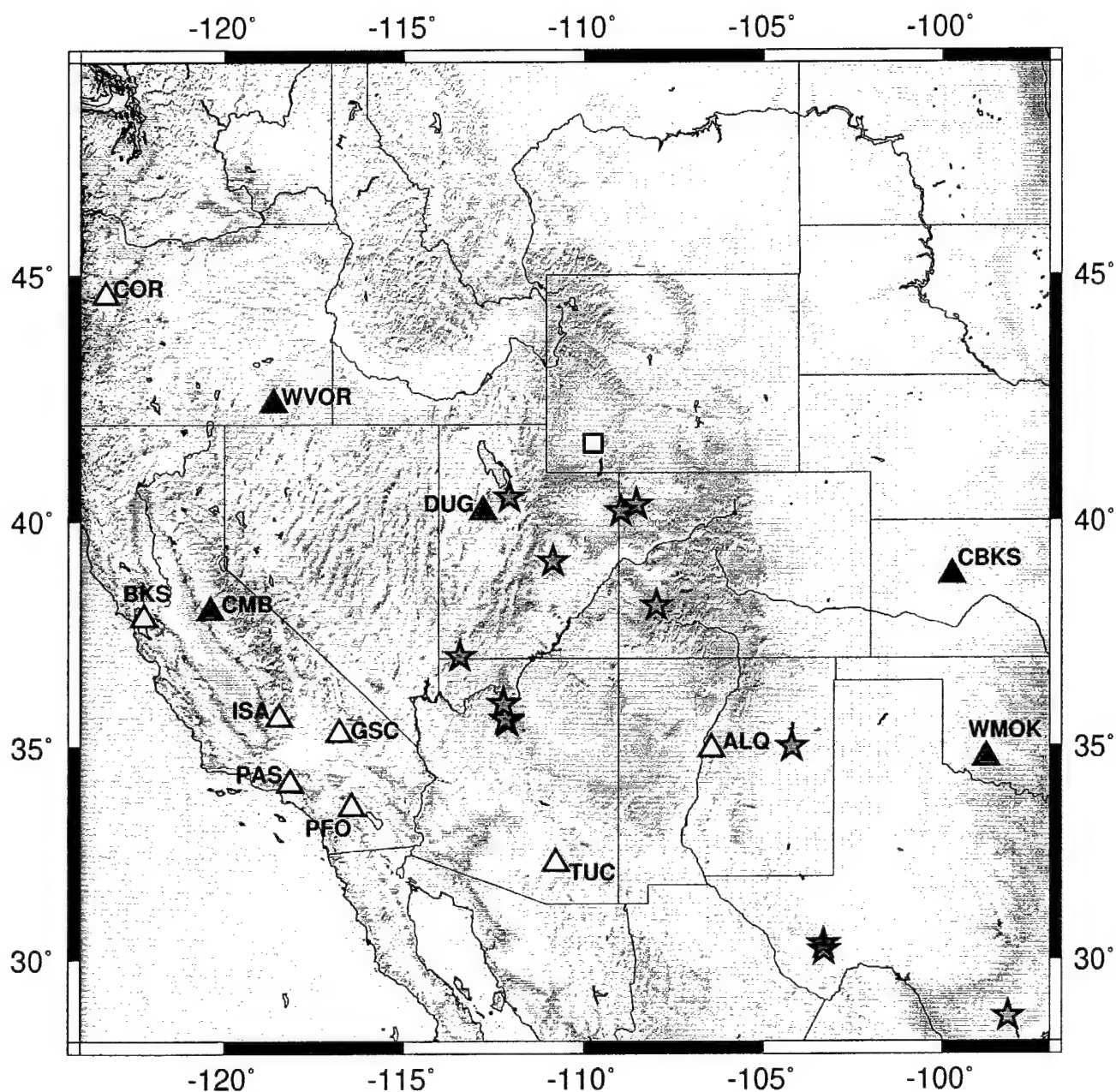


Figure 20. Map of the study area showing digitally recorded events for which SP:LP and SP-P:S peak amplitude ratios were determined. WWSN recording stations used are denoted by white triangles, earthquakes by red stars, and the one observed mine collapse by a yellow square. In the case of the large Texas earthquake (95/4/14), it is marked by a blue symbol as are additional recording stations for it.

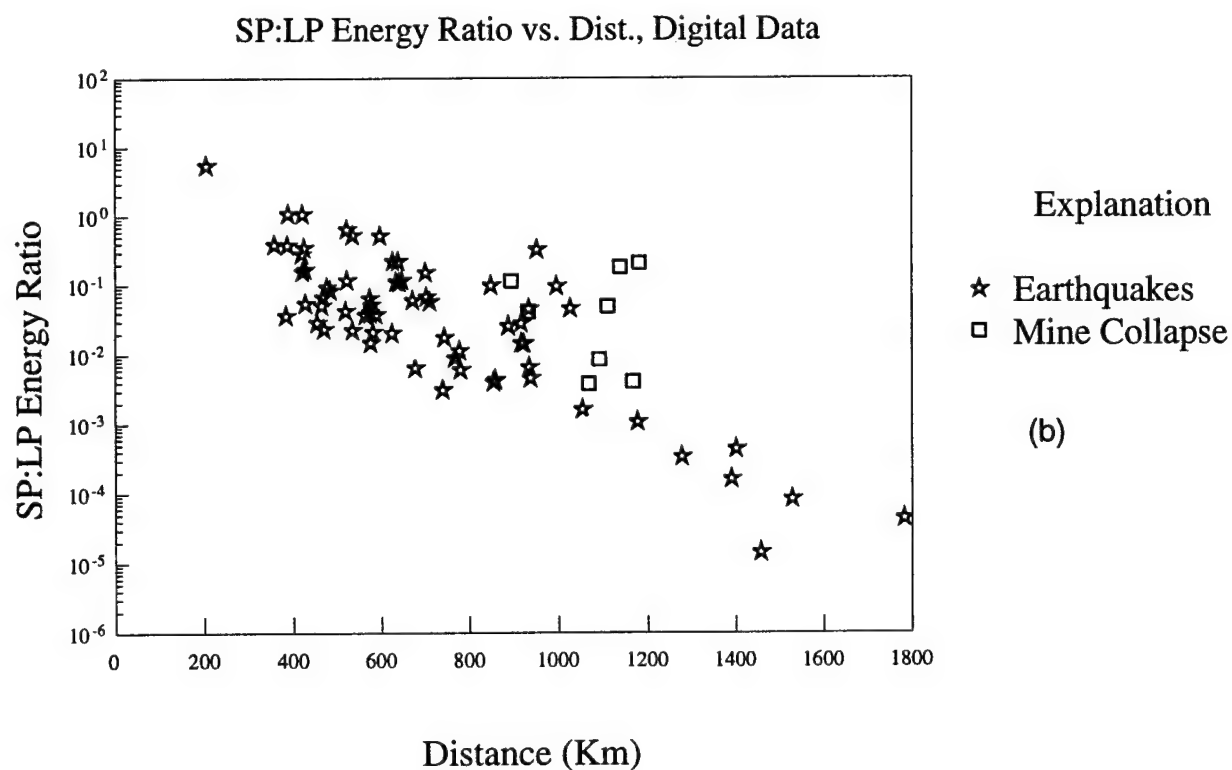
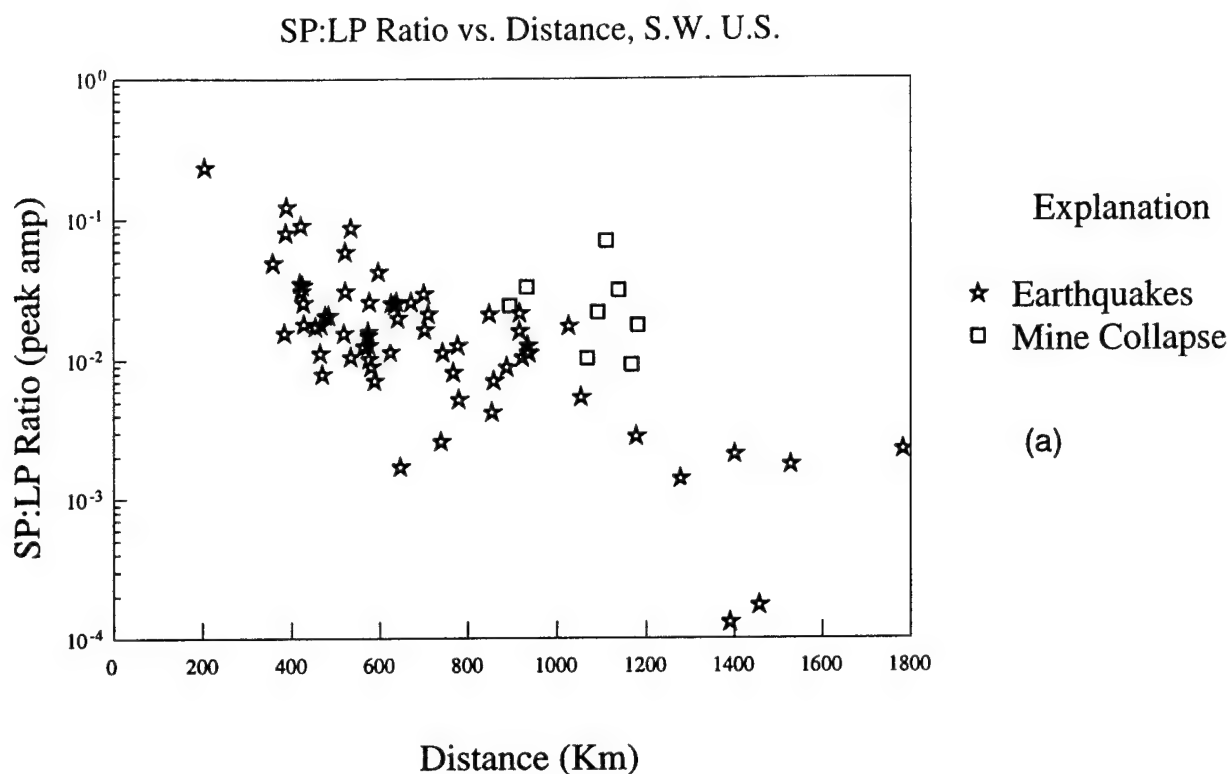


Figure 21. (a) SP:LP (peak amplitude) ratios for digital S.W. U.S. data and (b) SP:LP (integrated energy) ratios for for the same data set. Earthquakes are denoted by stars, and the Solvay mine collapse by squares.

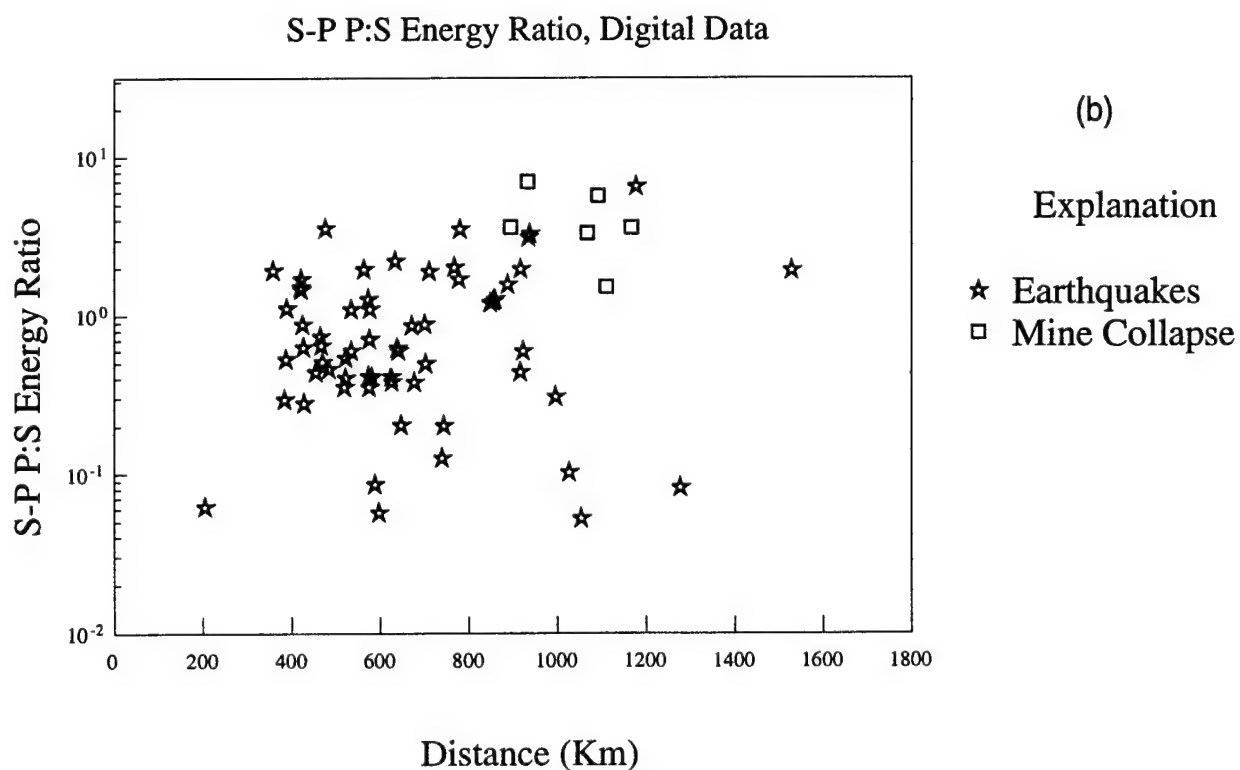
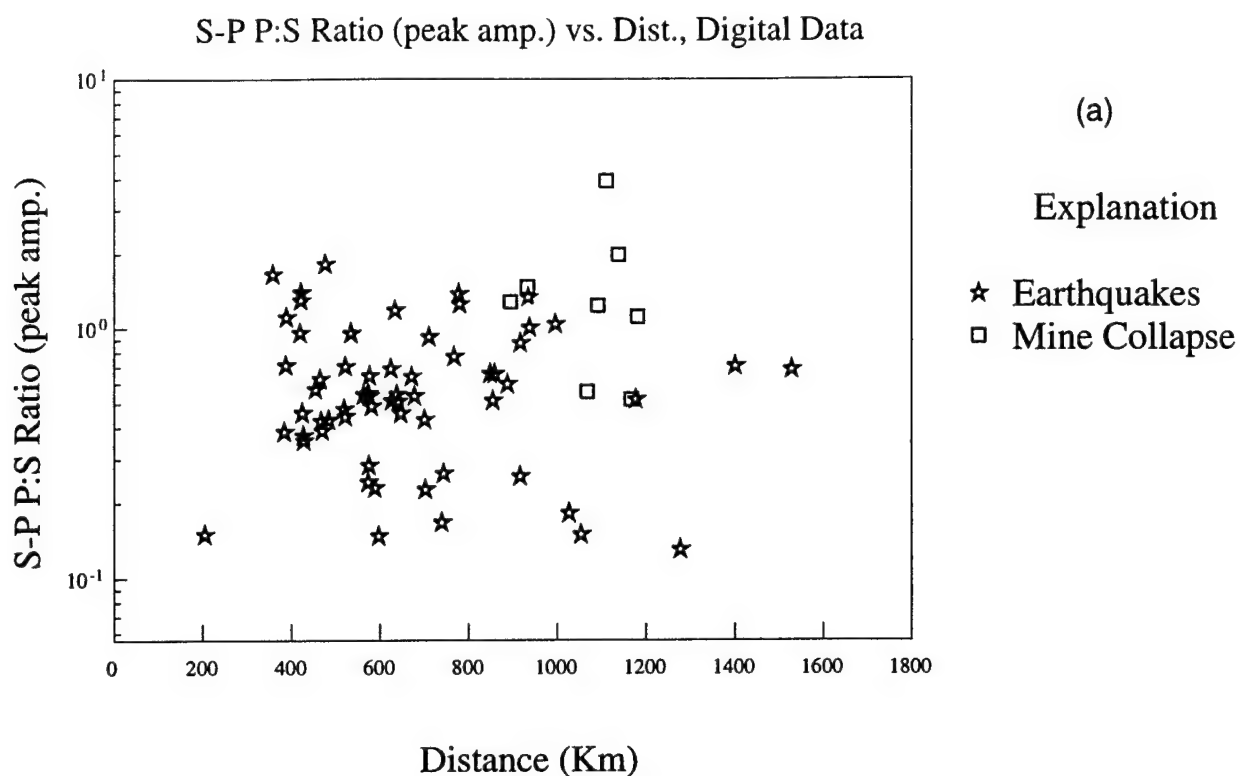


Figure 22. (a) S-P P:S ratios (peak amplitude) for digital S.W. U.S. data and (b) S-P P:S (integrated energy) ratios for for the same data set. Earthquakes are denoted by stars, and the Trona mine collapse by squares.

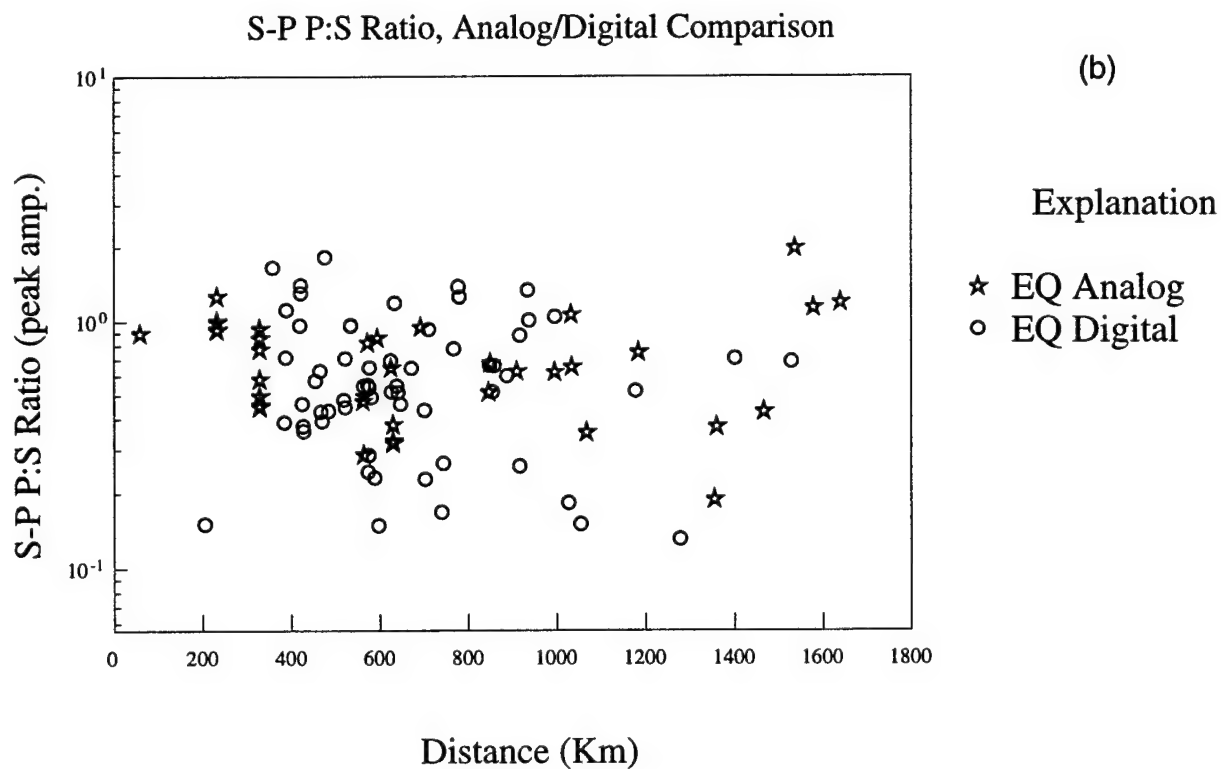
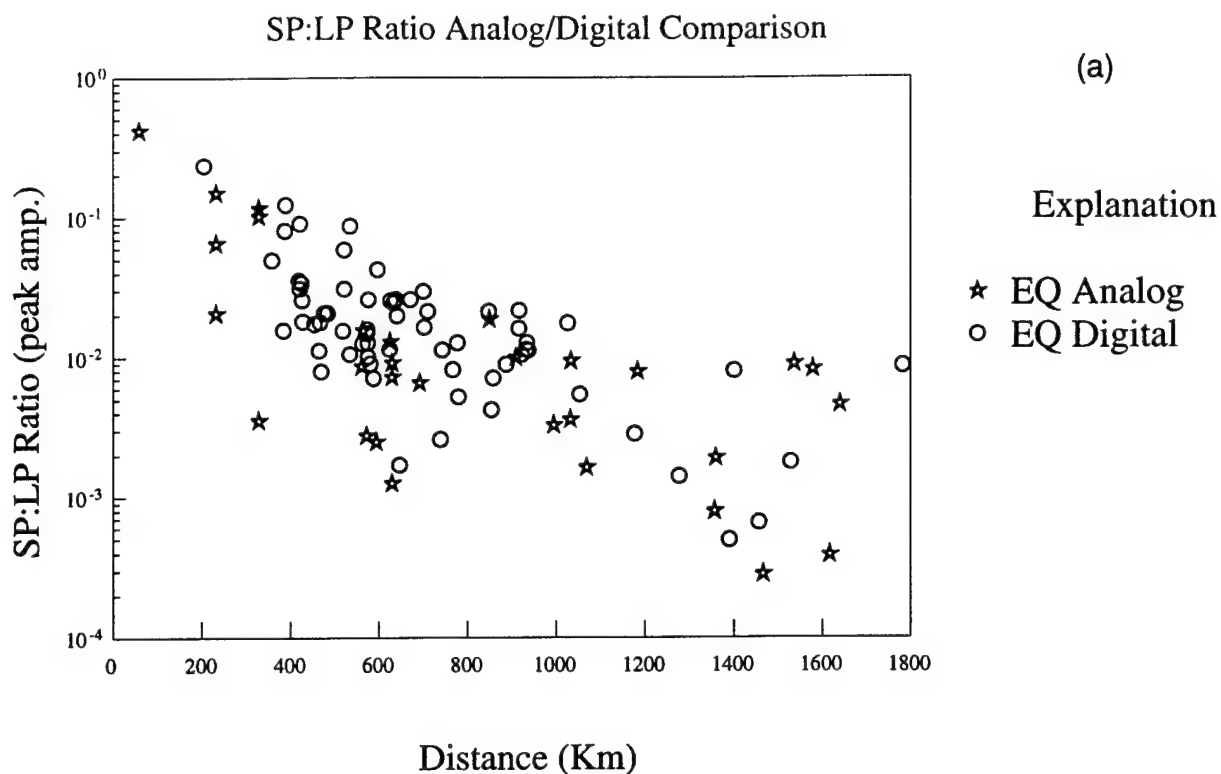


Figure 23. (a) Comparison of SP:LP peak amplitude ratios for analog (star) and digital (circle) data for S.W. U.S. earthquakes. (b) Comparison of S-P P:S peak amplitude ratios for analog (star) and digital (circle) data for the same data sets as in (a).

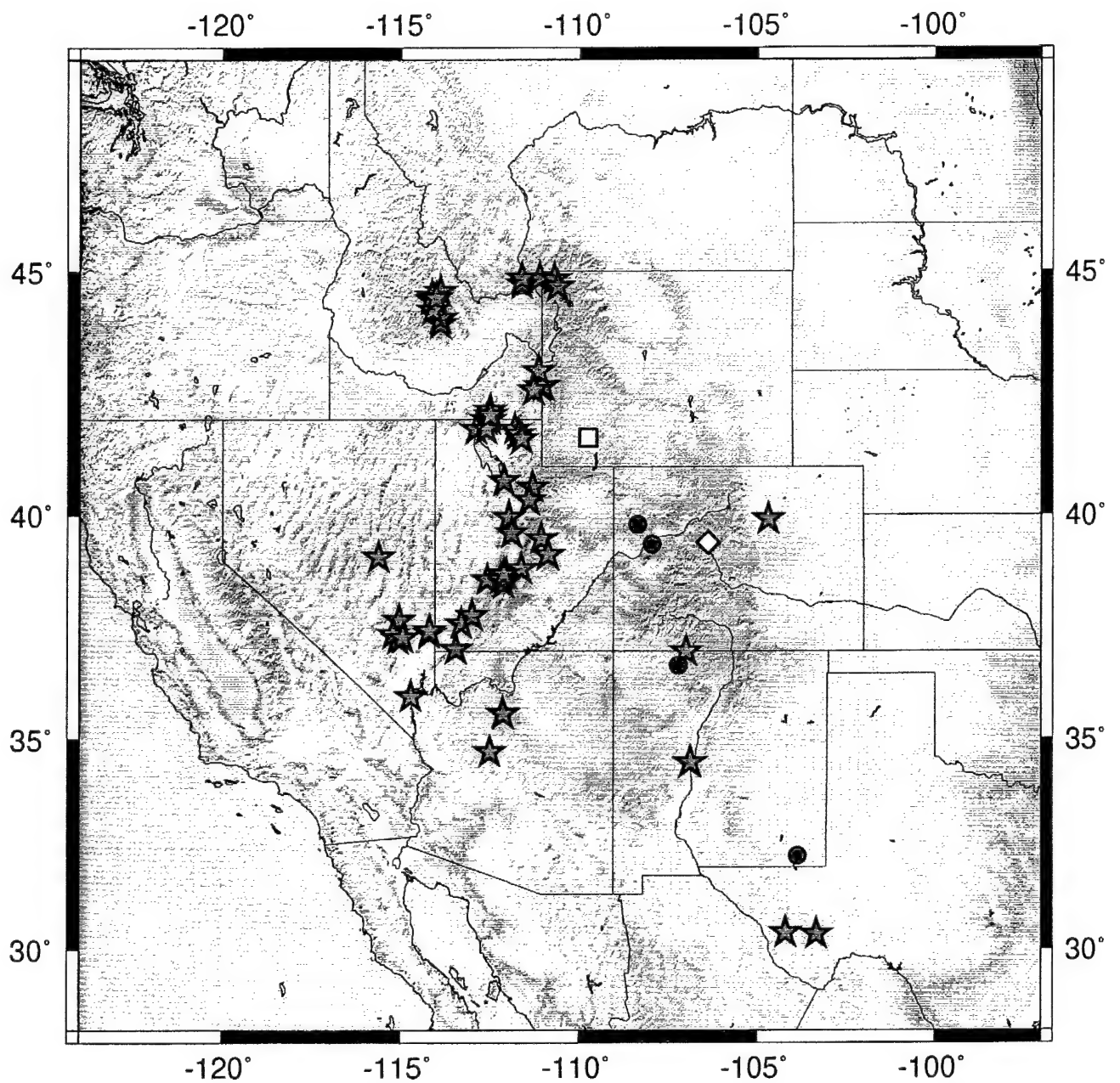


Figure 24. Map of the study area with locations of earthquakes (red stars), PNE's (blue circles), chemical explosions (yellow diamonds), and the Solvay mine collapse (yellow square) used for the $m_b:M_0$ analysis.

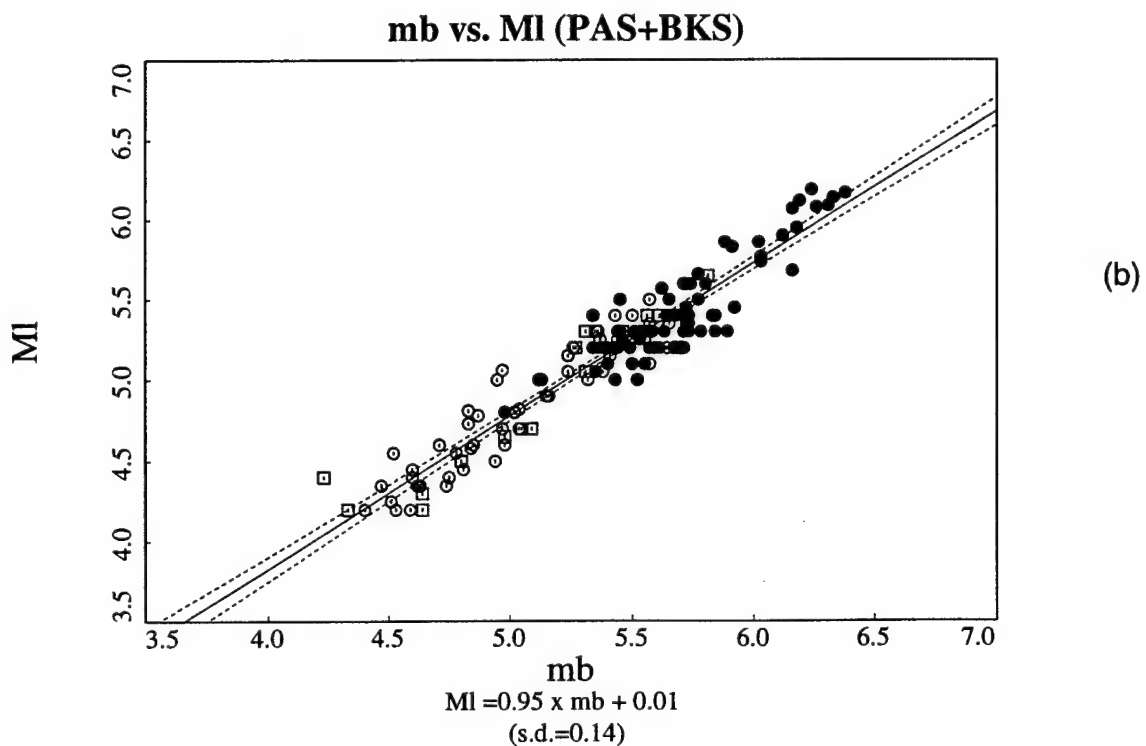
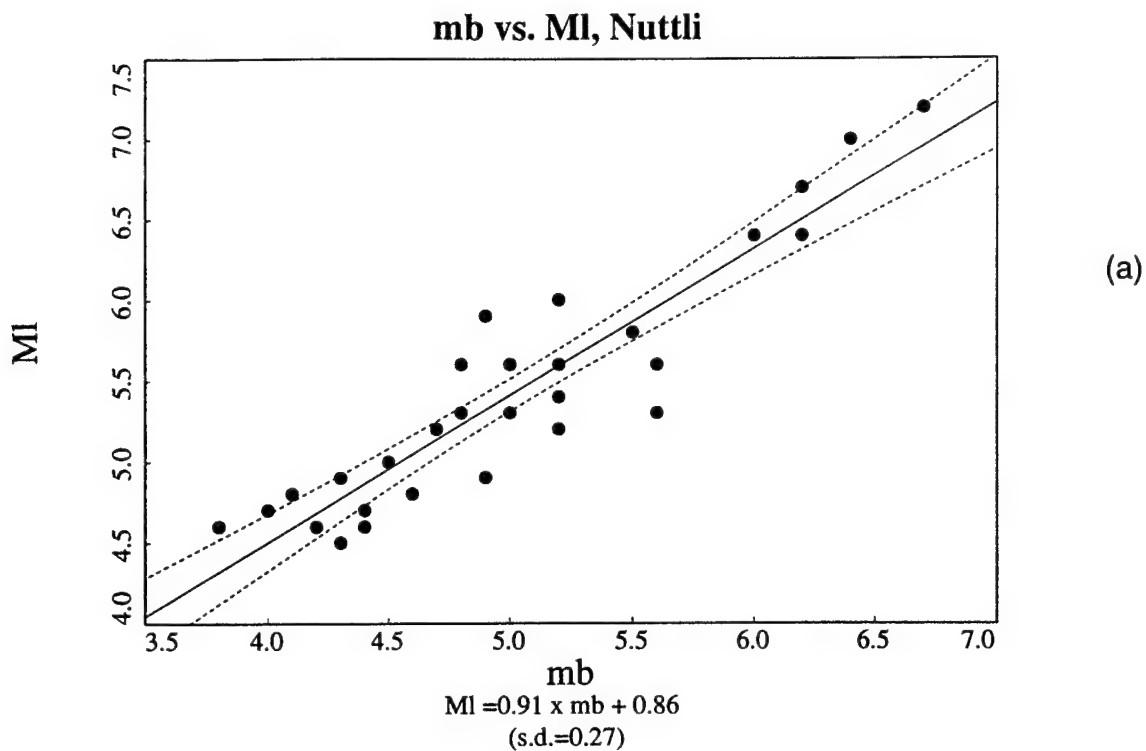


Figure 25. Least squares fit of m_b vs. M_L for (a) earthquakes previously reported by Nuttli and Herrman and (b) NTS explosions. The solid is the best fitting line (see equation below figure), while the dashed lines denote the 2σ confidence level of the fit of the line.

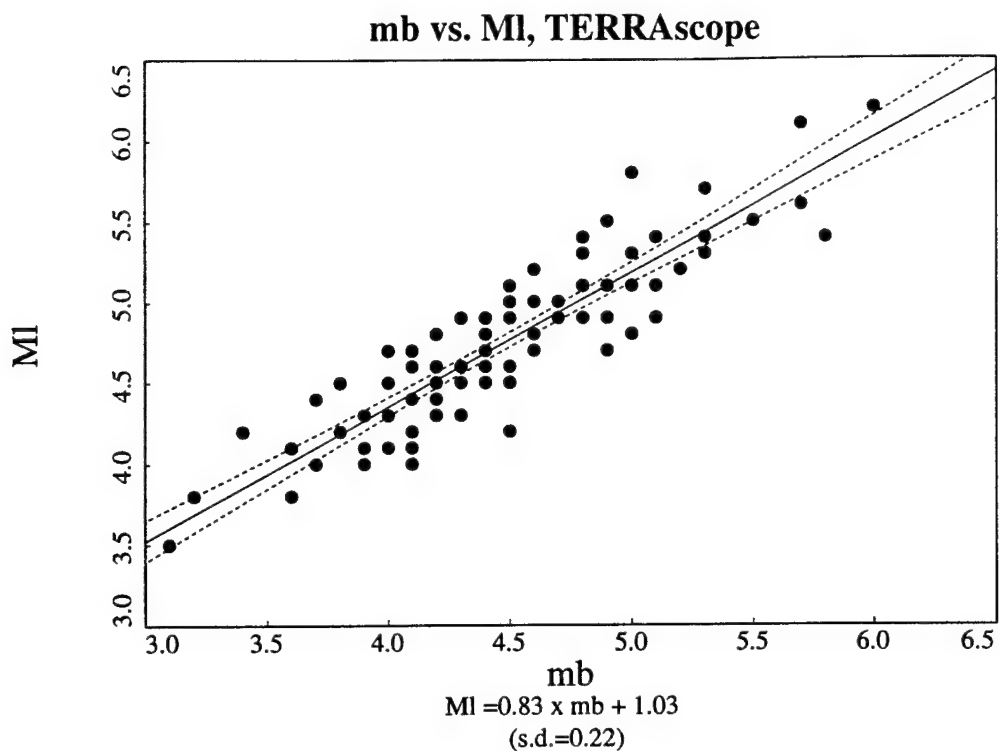


Figure 26. Least squares fit of m_b vs. M_L for recent (1990+) earthquakes recorded by TERRAscope for which M_L and teleseismic m_b values are available.

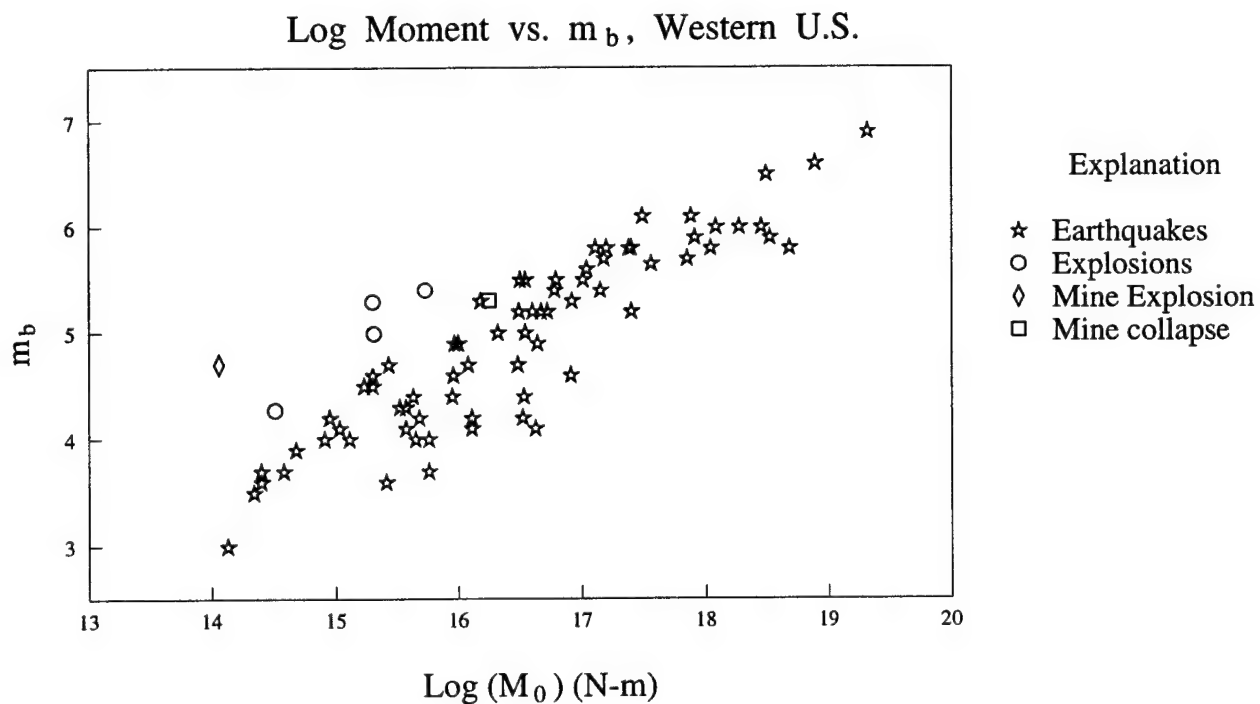


Figure 27. Log moment (M_0) vs. m_b for events in the Colorado Plateau and western Cordillera: earthquakes are stars, PNE's are circles, chemical explosions are diamonds, and the Solvay mine collapse denoted by a square.

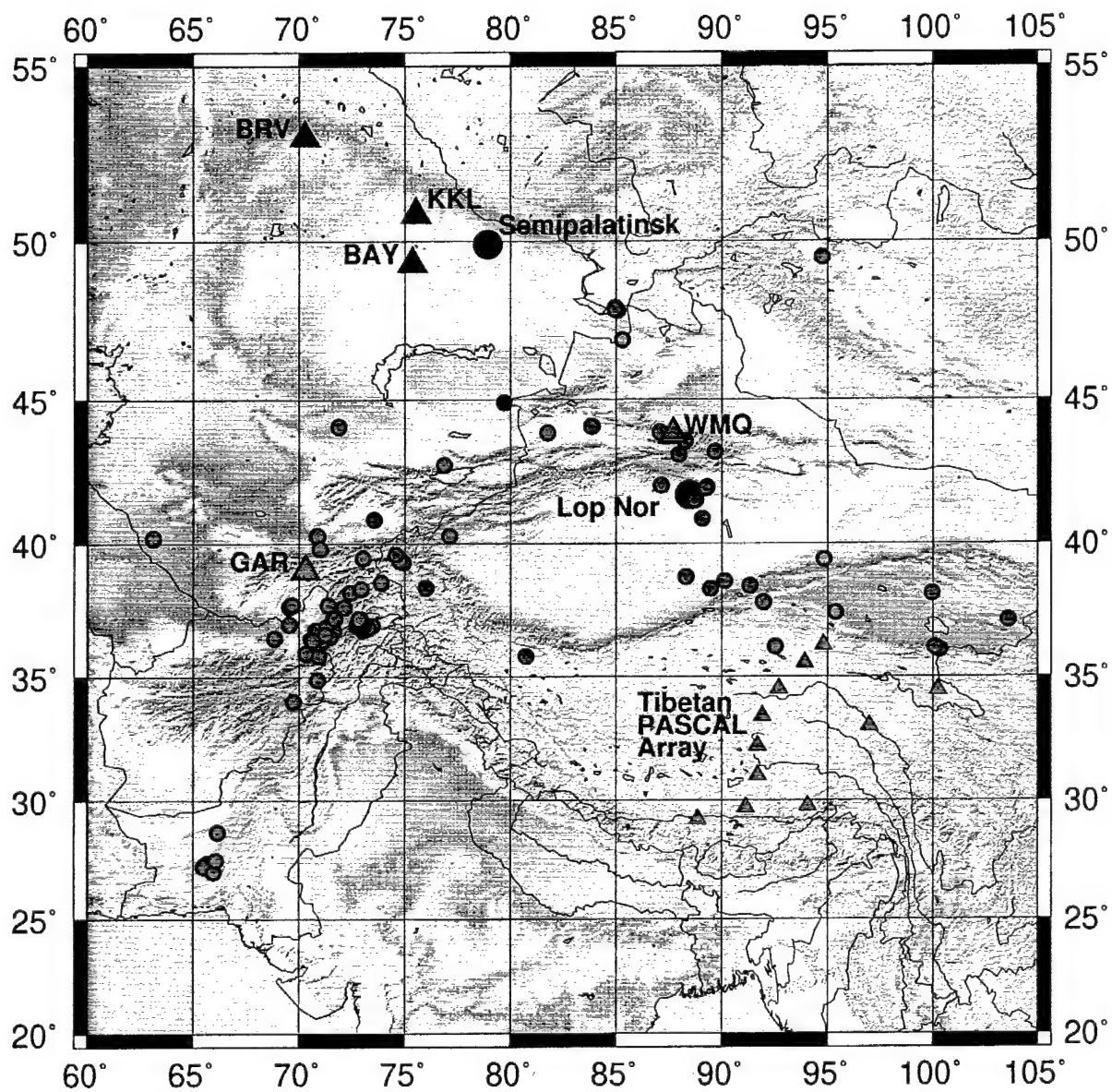


Figure 28. Map of central Asian study area showing events (small circles) analyzed and seismic stations used. Earthquakes are color-coded with the station by which they were recorded. The large black circles denote nuclear test sites. The one small black circle is an earthquake recorded by BRV.

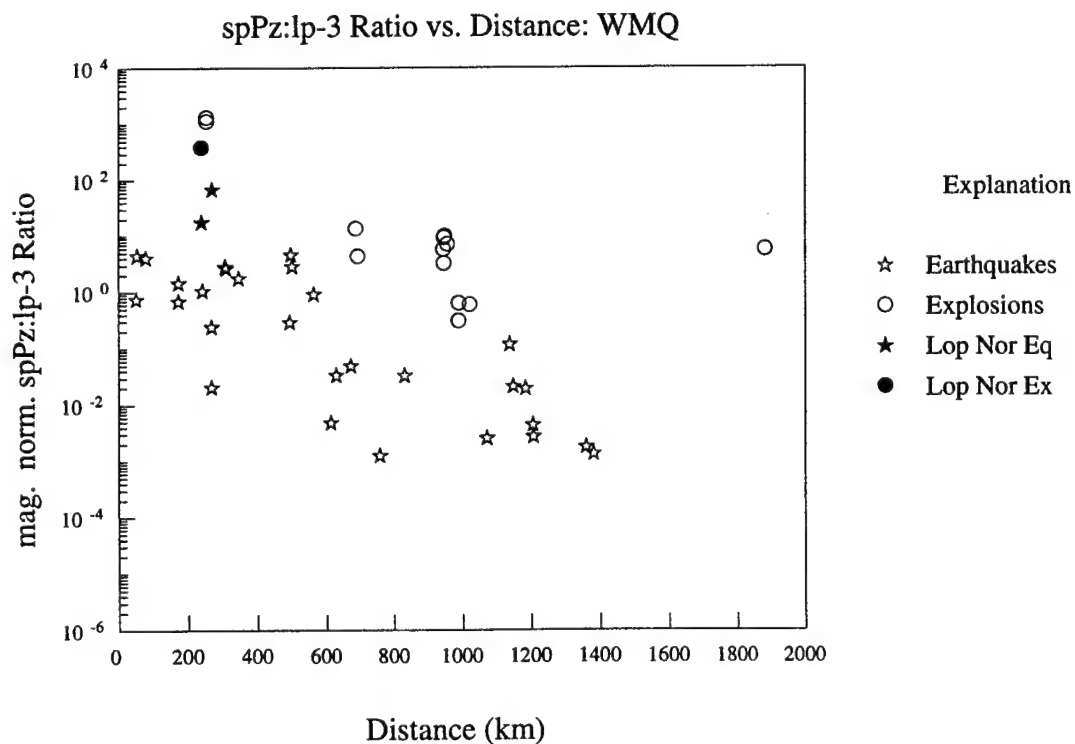
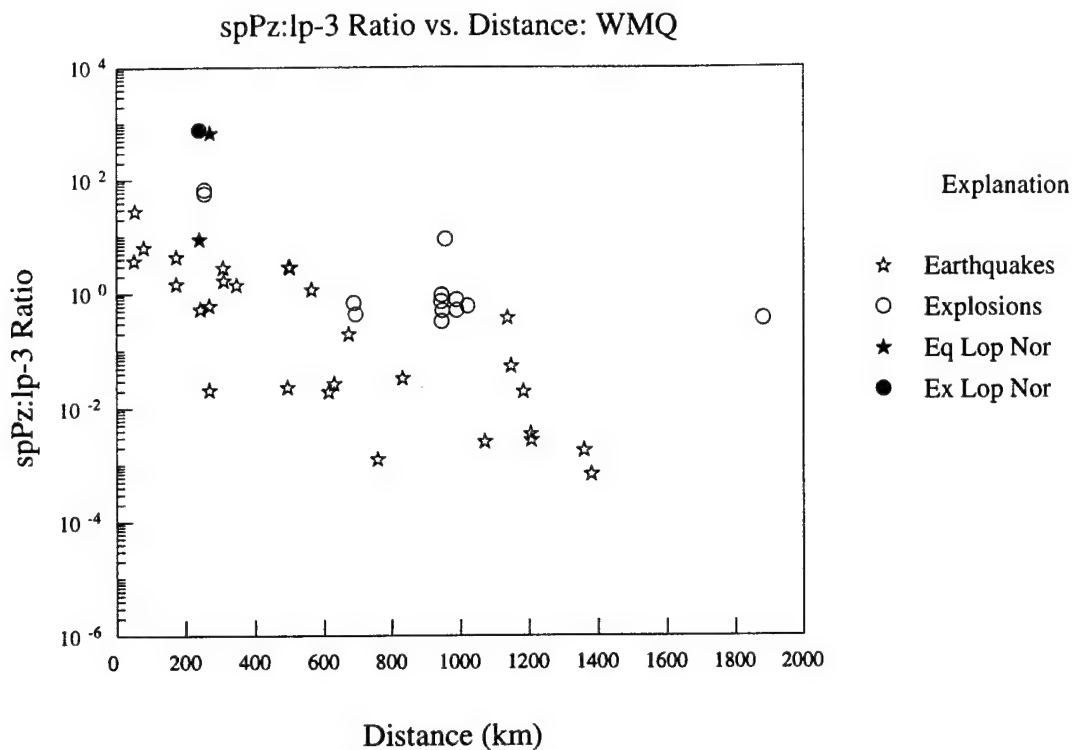


Figure 29. (a) Short-period:long-period energy ratio vs. distance for earthquakes (stars) and explosions (circles) recorded by WMQ as well as a few other recordings from those stations in black in Figure 28. The one distant ($d \approx 1900$ km) explosion is a Lop Nor shot recorded at BRV. (b) Magnitude-normalized short-period:long-period energy ratio vs. distance for the same data.

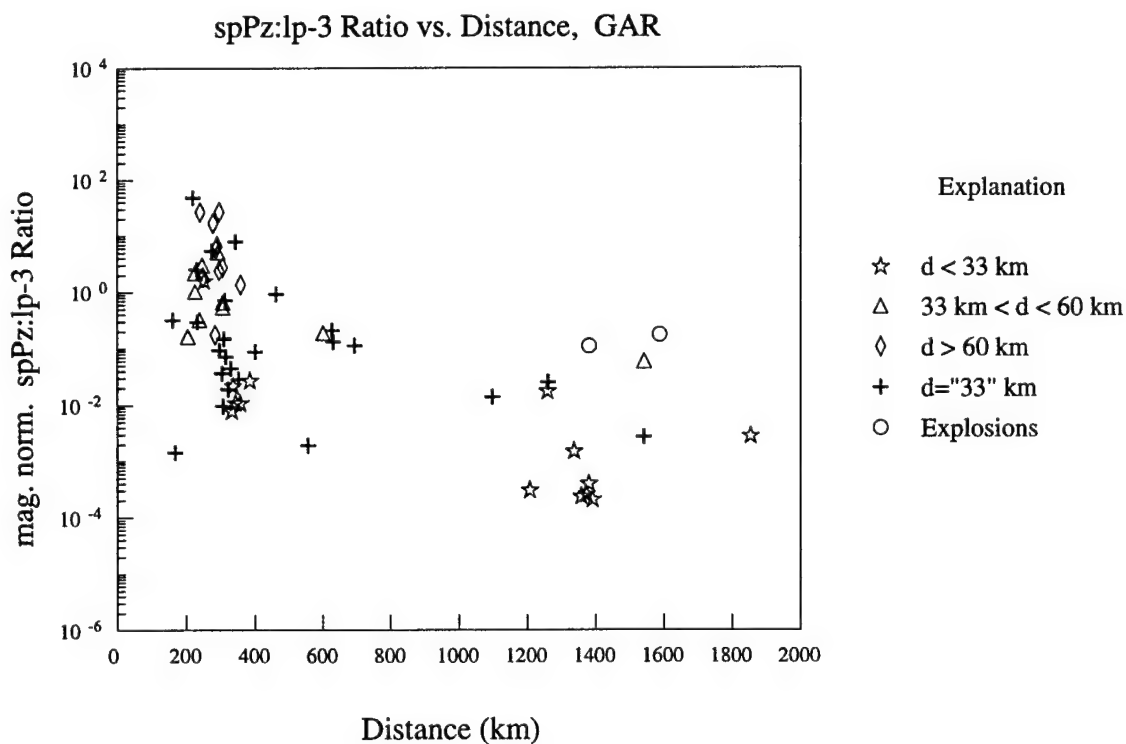
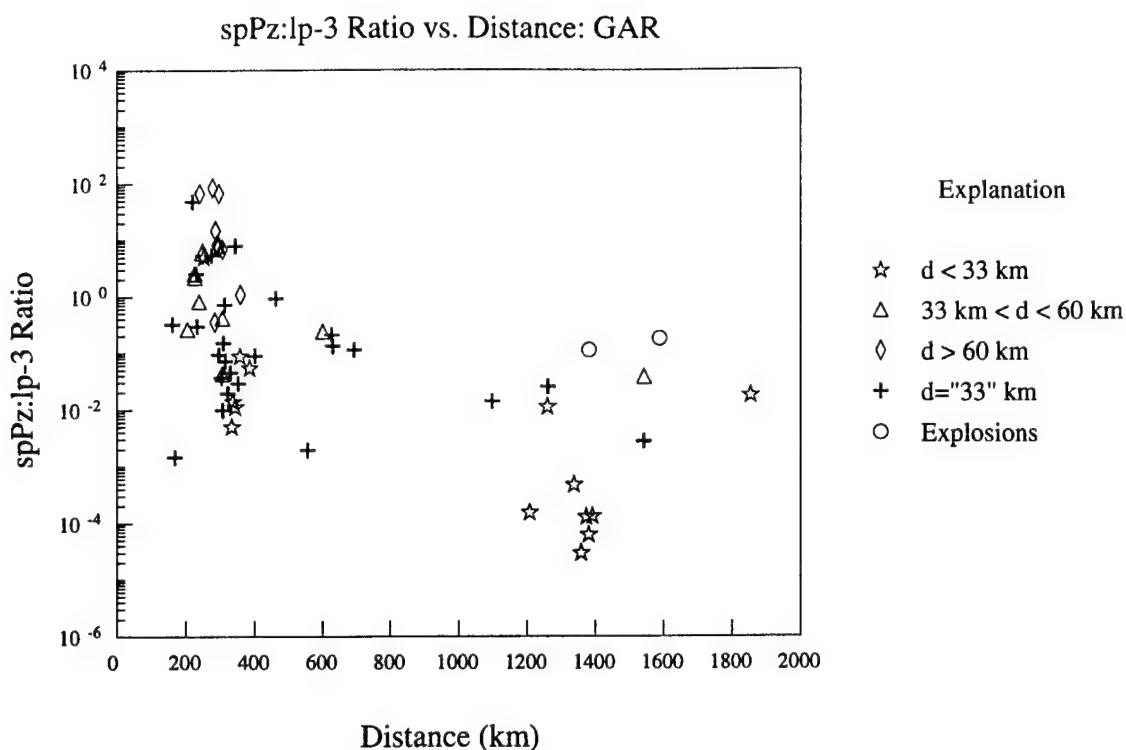


Figure 30. (a) Short-period:long-period energy ratio vs. distance for shallow (stars), intermediate-depth (triangles), and deep (diamond) earthquakes, and explosions (circles) recorded by GAR. Crosses denote earthquakes with a PDE depth of 33 km. (b) Magnitude-normalized short-period:long-period energy ratio vs. distance for the same data.

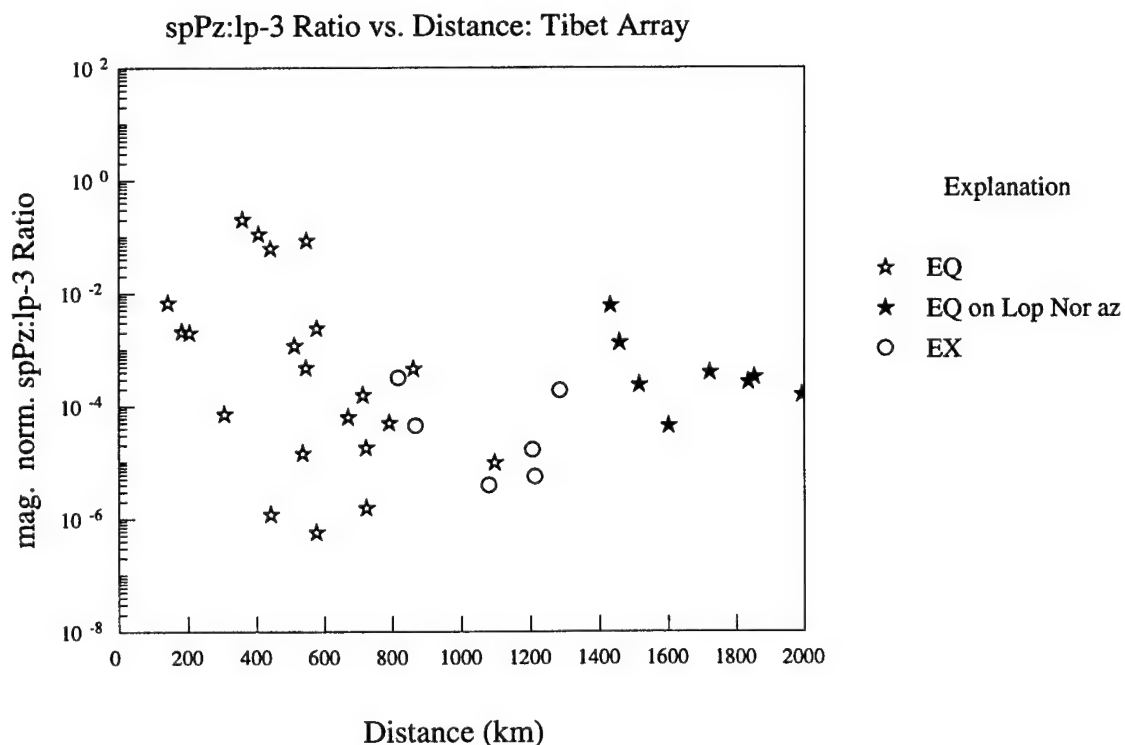
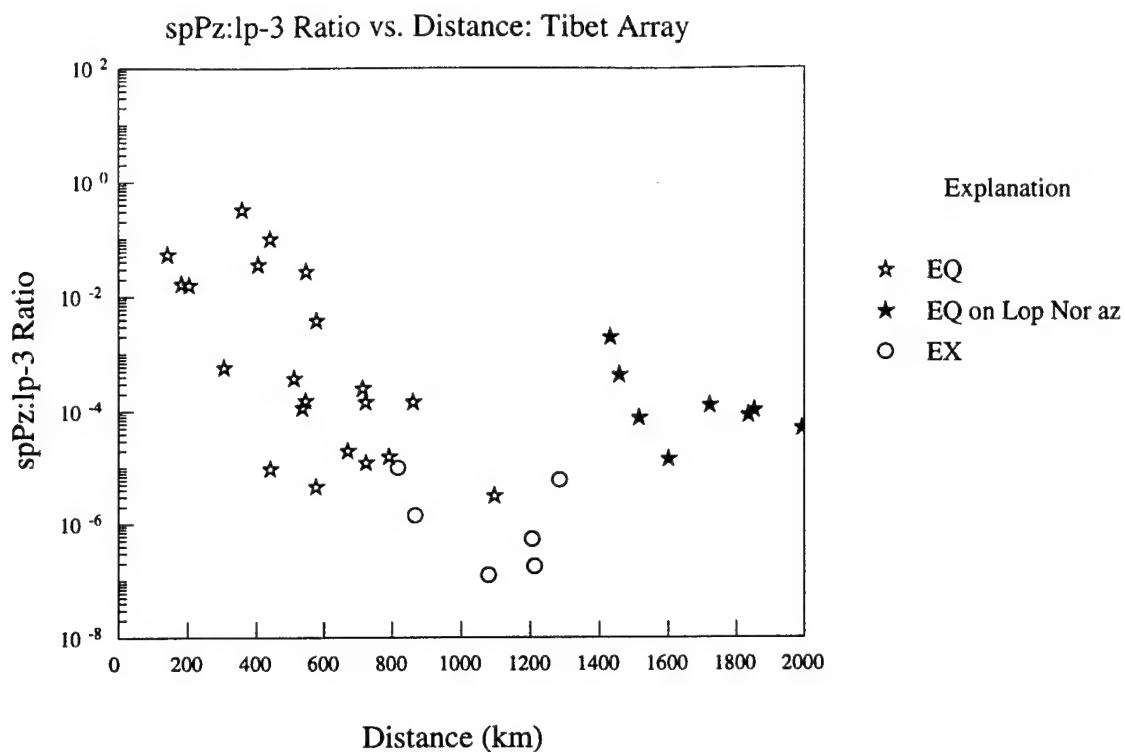


Figure 31. (a) Short-period:long-period energy ratio vs. distance for earthquakes (stars), and a Lop Nor explosion (circles) recorded by the Tibet PASCAL Array. The solid stars denote an earthquake which lies on azimuth with Lop Nor. Note the Y-axis is shifted down 2 orders of magnitude relative to the previous figures. (b) Magnitude-normalized short-period:long-period energy ratio vs. distance for the same data.

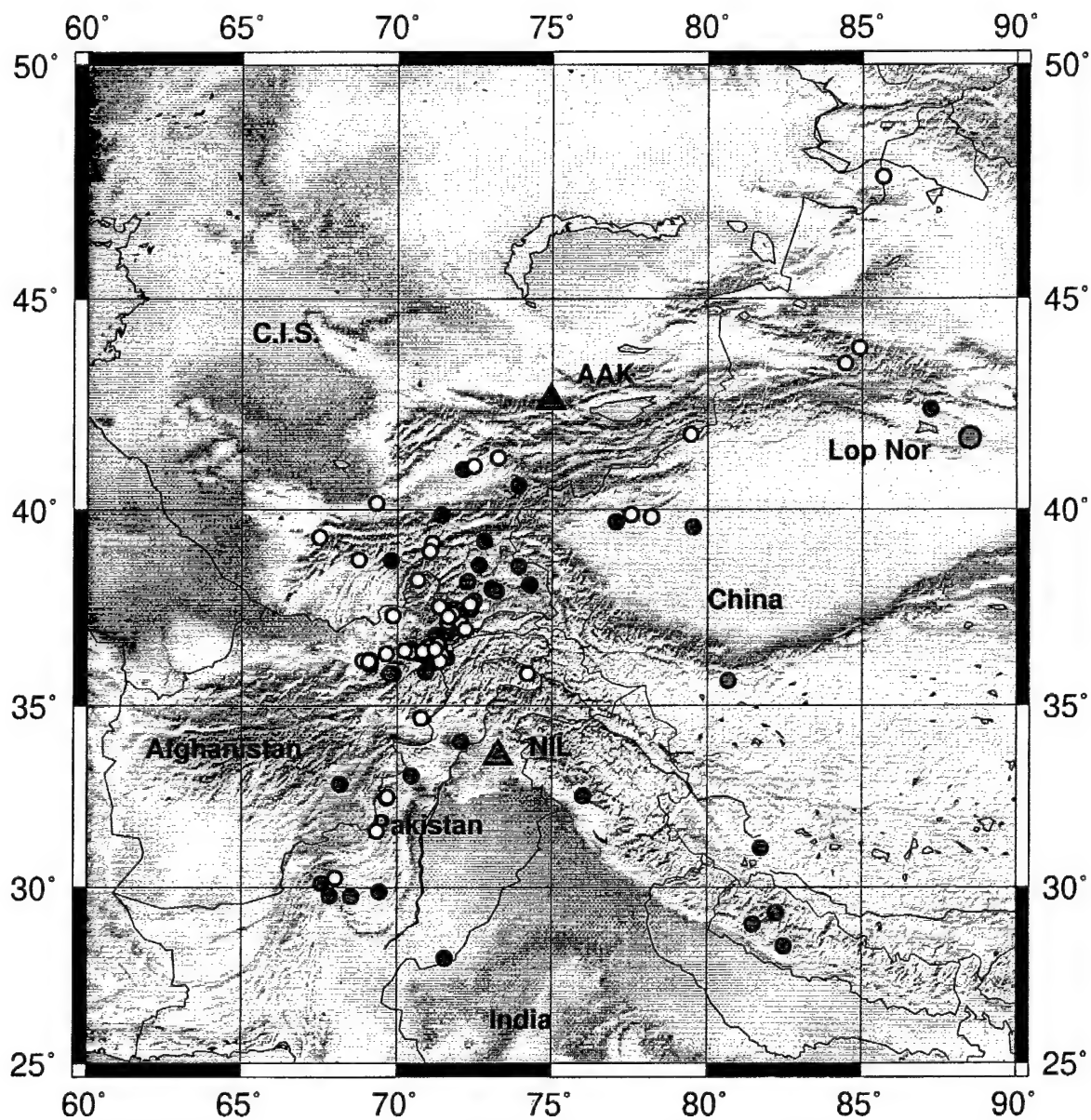


Figure 32. Map of Southwest Asia (centered about Hindu-Kush) study area showing earthquakes (small circles) analyzed and seismic stations used. Earthquakes are color-coded with the station by which they were recorded with the exception of events recorded by both NIL and AAK which are yellow. The large black circle denotes Lop Nor Test Site.

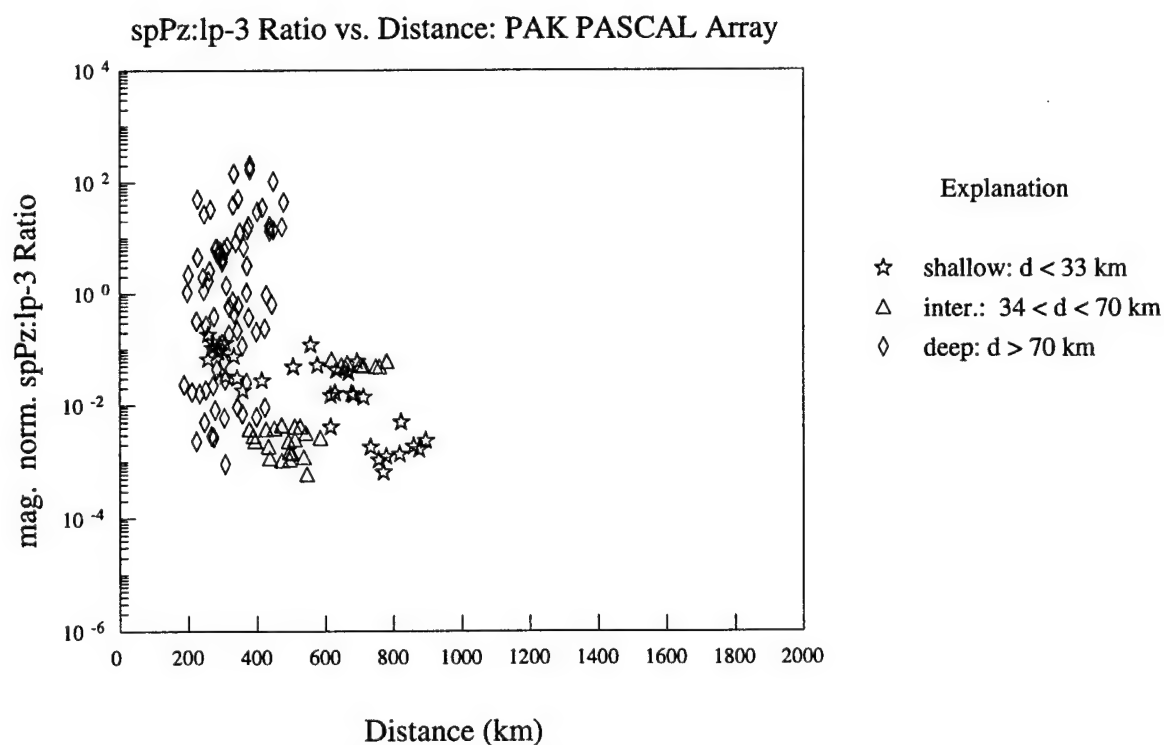
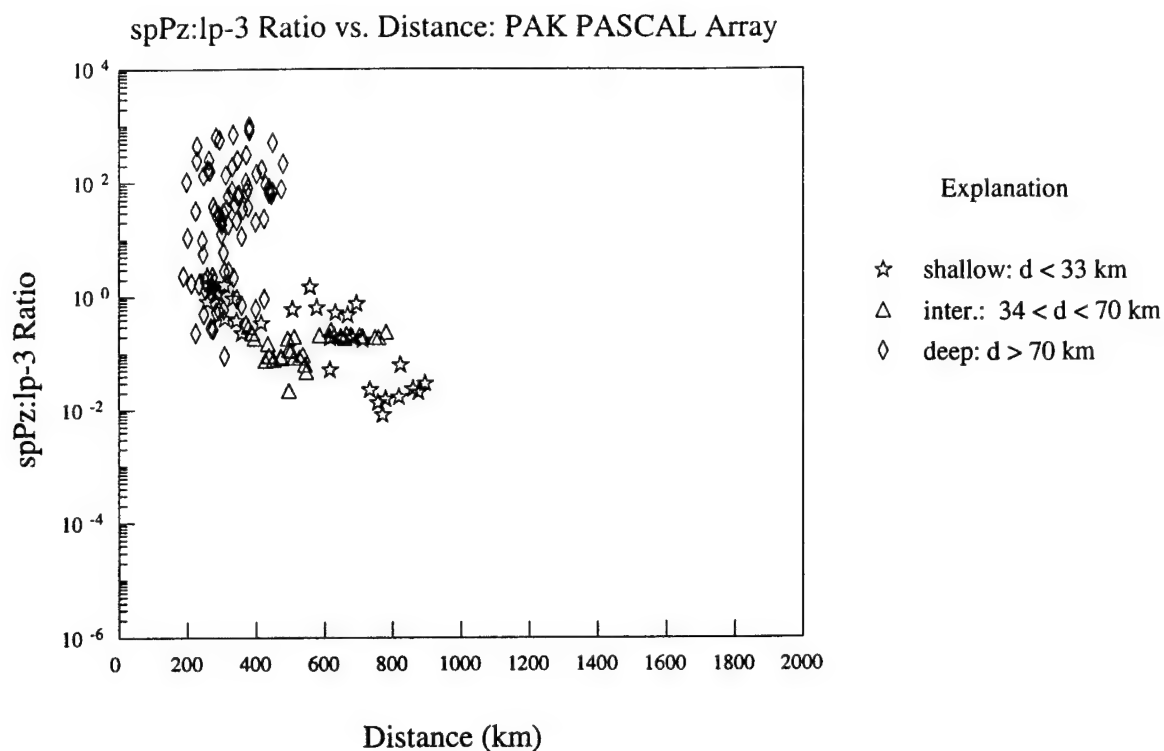


Figure 33. (a) Short-period:long-period energy ratio vs. distance for shallow (stars), intermediate-depth (triangles), and deep (diamonds) earthquakes (stars) recorded by the Pakistan PASCAL Array. (b) Magnitude-normalized short-period:long-period energy ratio vs. distance for the same data.

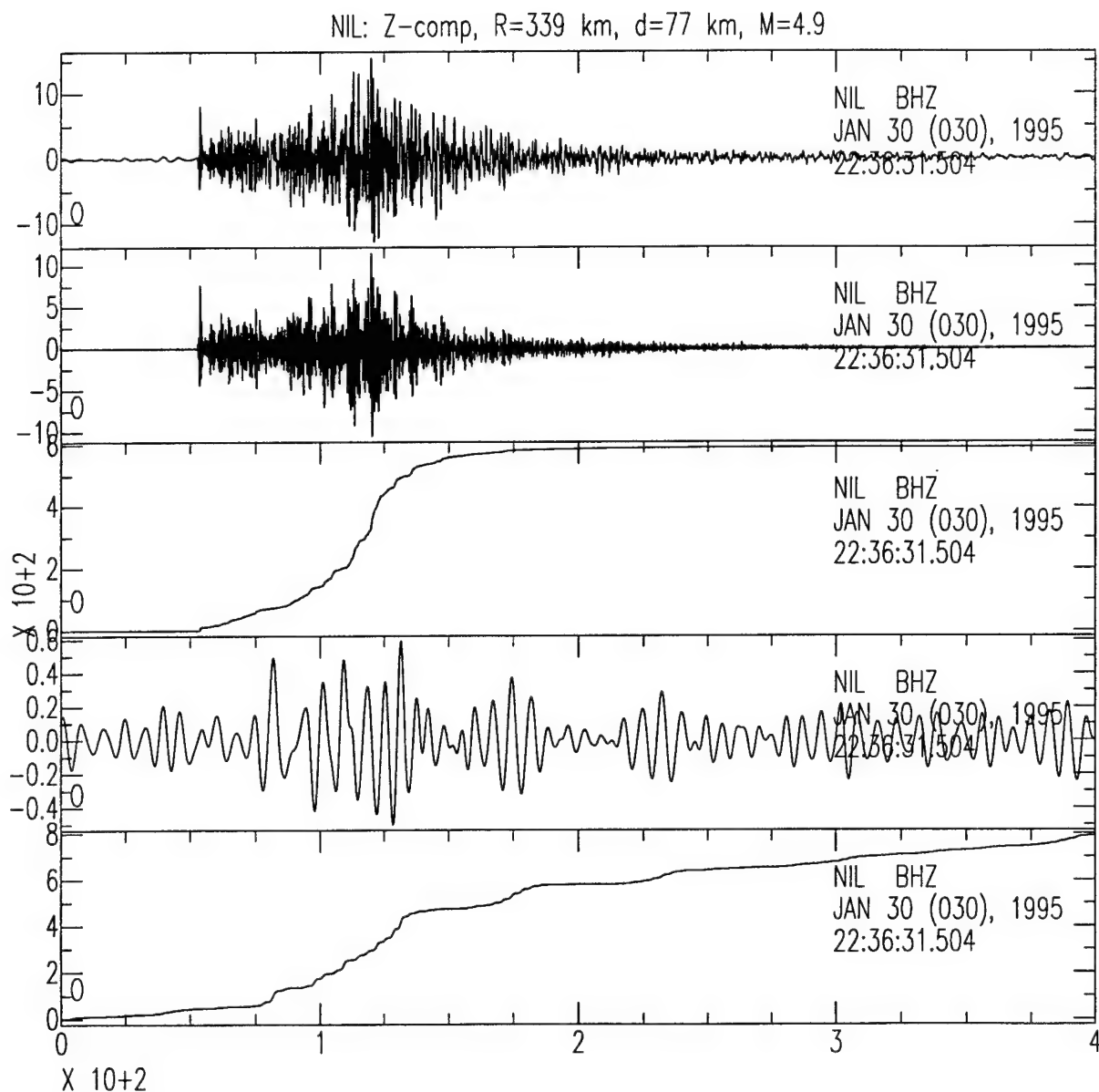


Figure 35. Vertical component velocity record for an intermediate depth earthquake recorded at NIL. The top trace is the broadband record. The second trace is the high-pass ($f \geq 1$ Hz) play-out with its attendant energy curve under it. The fourth and fifth traces are the long-period ($0.033 \leq f \leq 0.125$ Hz) play-out and energy curve, respectively.

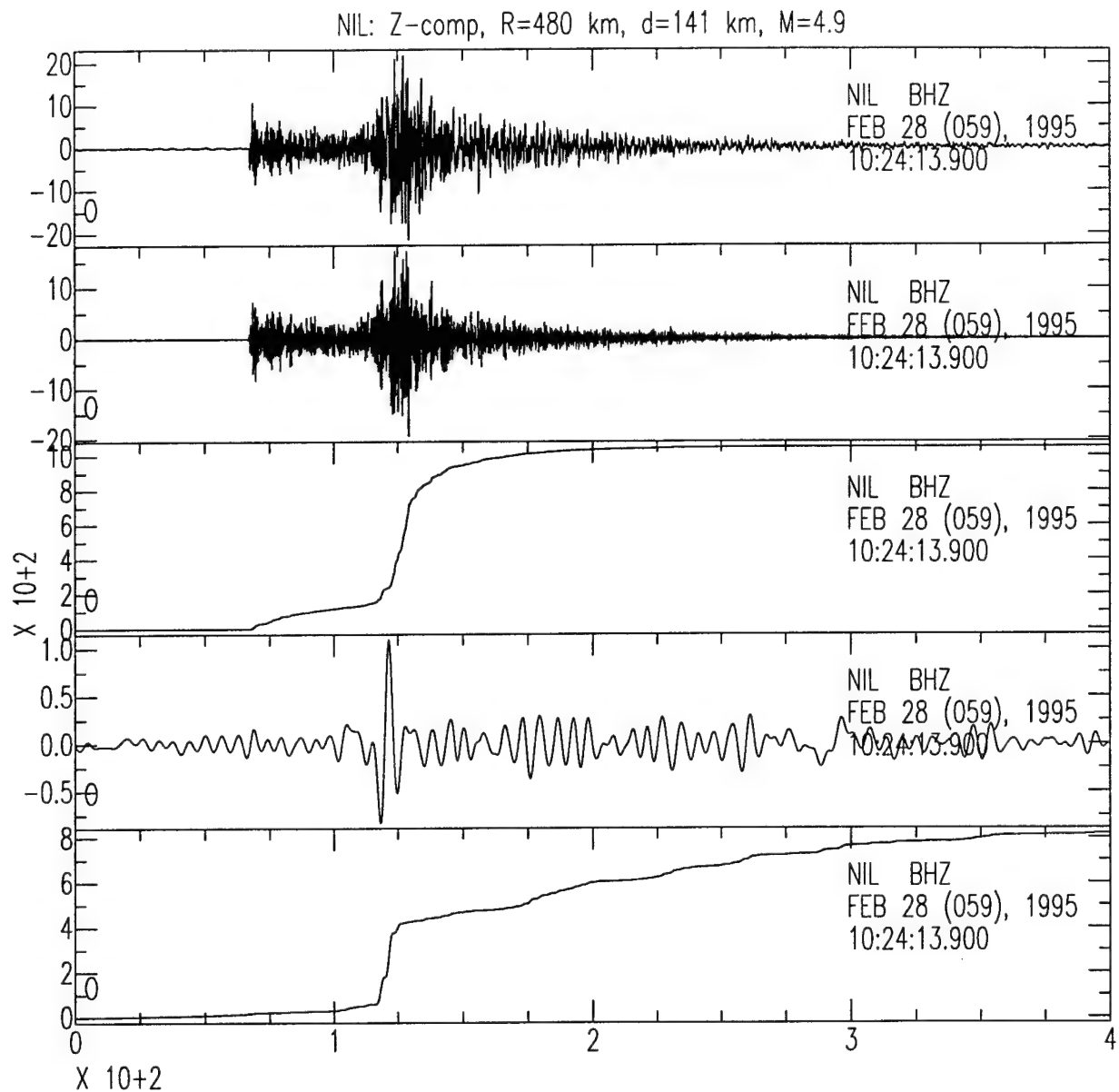


Figure 36. Vertical component velocity record for a deep earthquake recorded at NIL. The top trace is the broadband record. The second trace is the high-pass ($f \geq 1$ Hz) play-out with its attendant energy curve under it. The fourth and fifth traces are the long-period ($0.033 \leq f \leq 0.125$ Hz) play-out and energy curve, respectively.

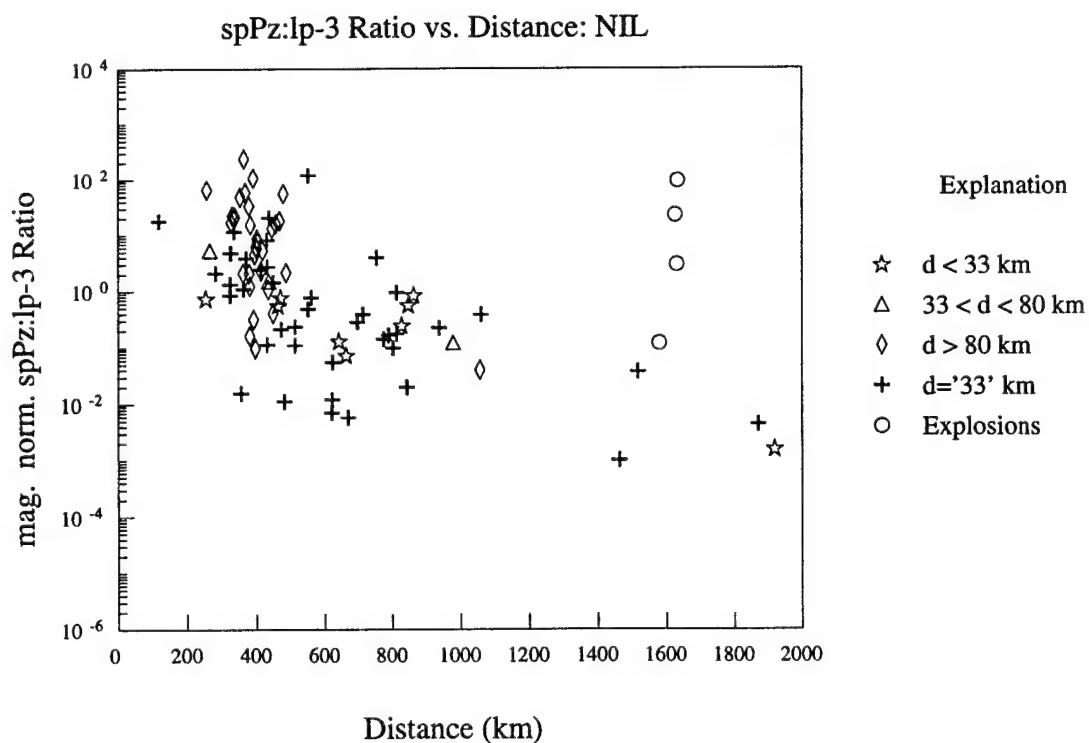
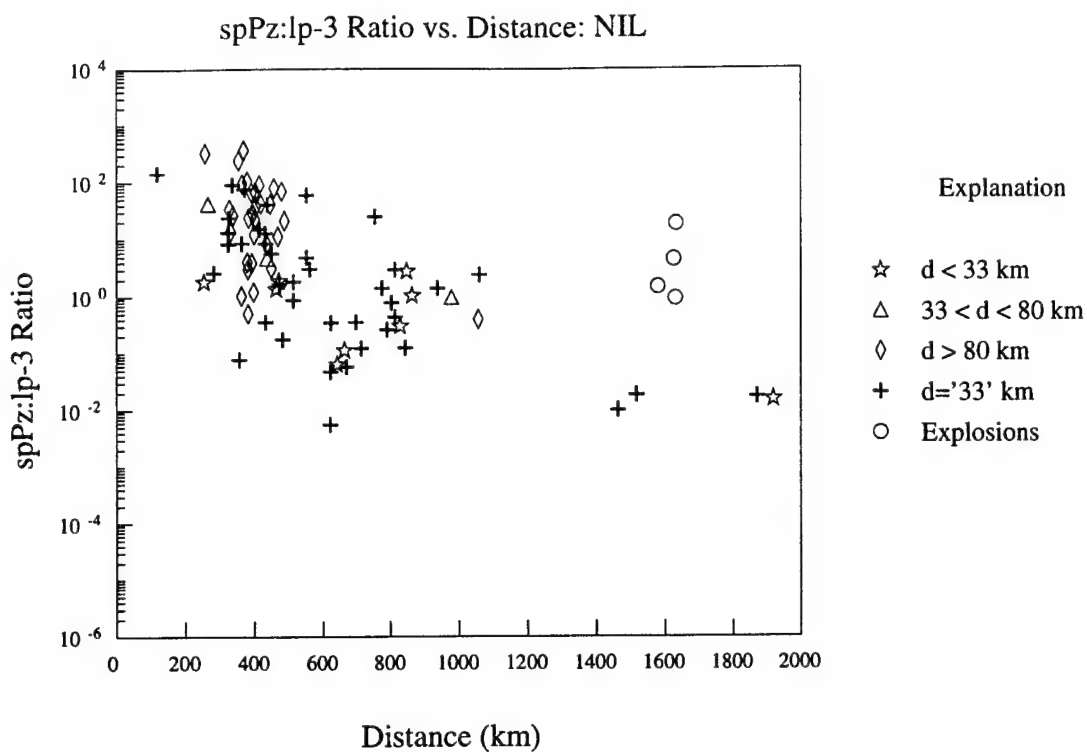


Figure 37. (a) Short-period:long-period energy ratio vs. distance for shallow (stars), intermediate-depth (triangles), and deep (diamonds) earthquakes (stars), and explosions (circles) recorded by NIL. Crosses denote earthquakes with PDE depths of 33 km. (b) Magnitude-normalized short-period:long-period energy ratio vs. distance for the same data.

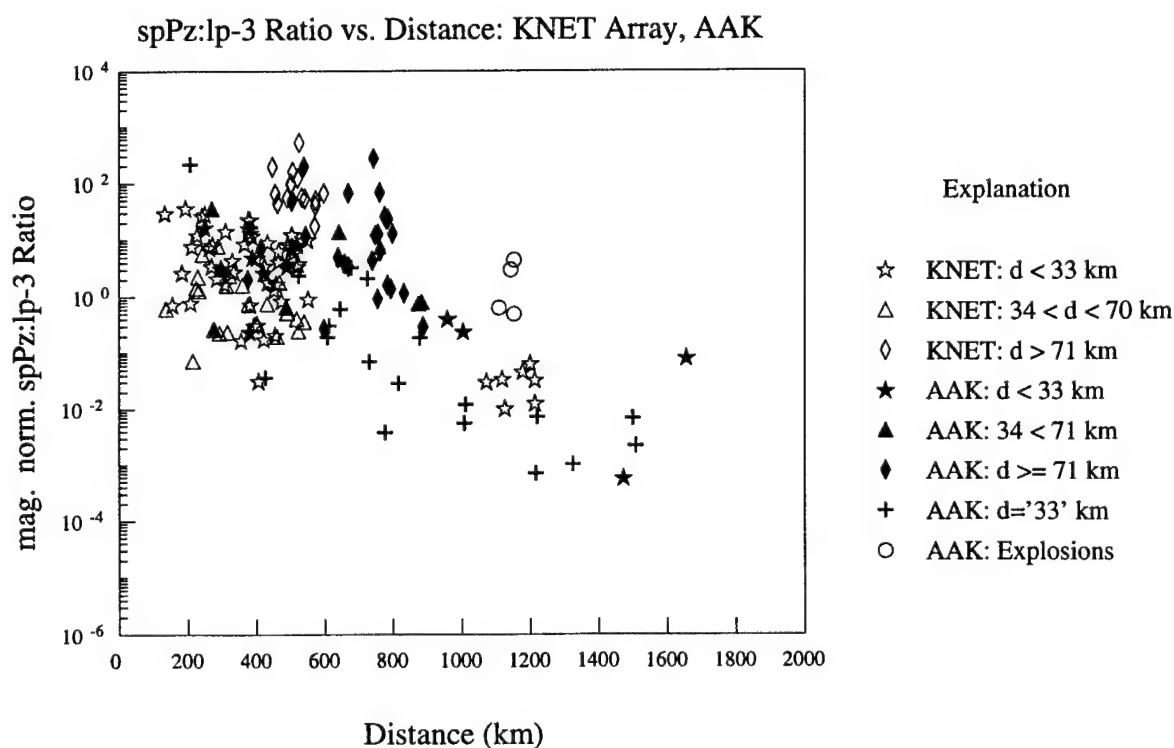
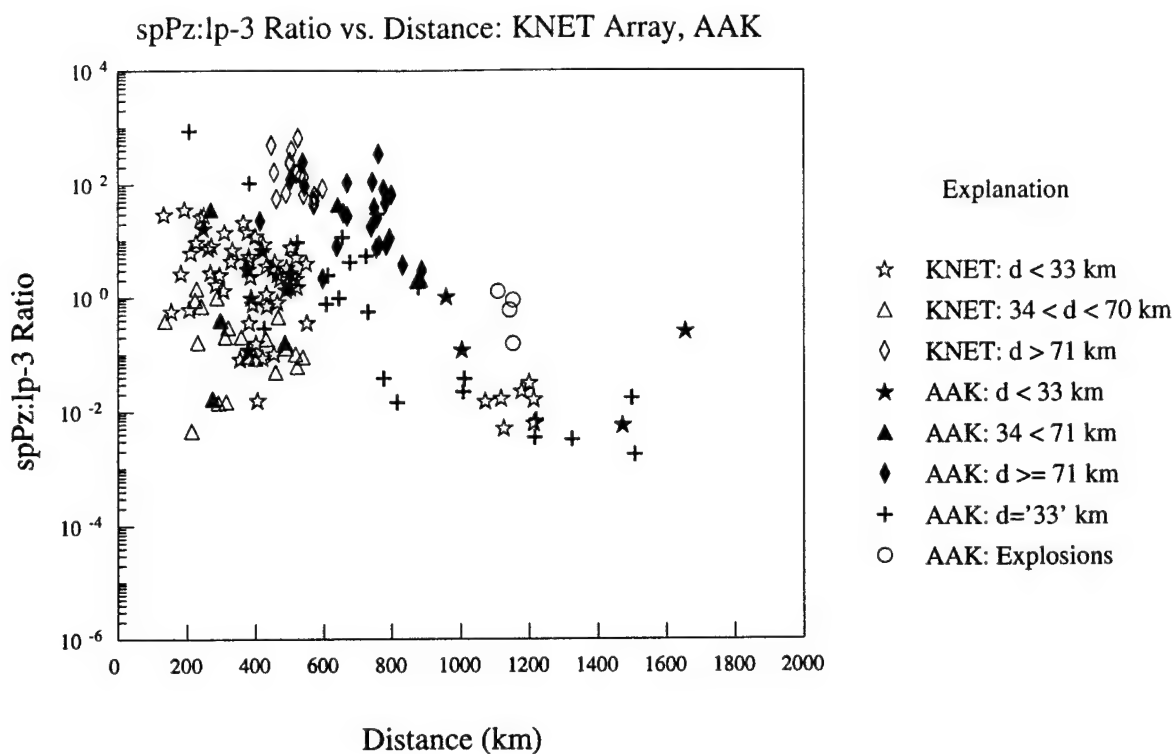


Figure 38. (a) Short-period:long-period energy ratio vs. distance for shallow (stars), intermediate-depth (triangles), and deep (diamonds) earthquakes (stars) recorded by the KNET Array (open symbols) and AAK (filled symbols). Crosses denote earthquakes with PDE depths of 33 km. Lop Nor explosions (circles) were all recorded by AAK only. (b) Magnitude-normalized short-period:long-period energy ratio vs. distance for the same data.

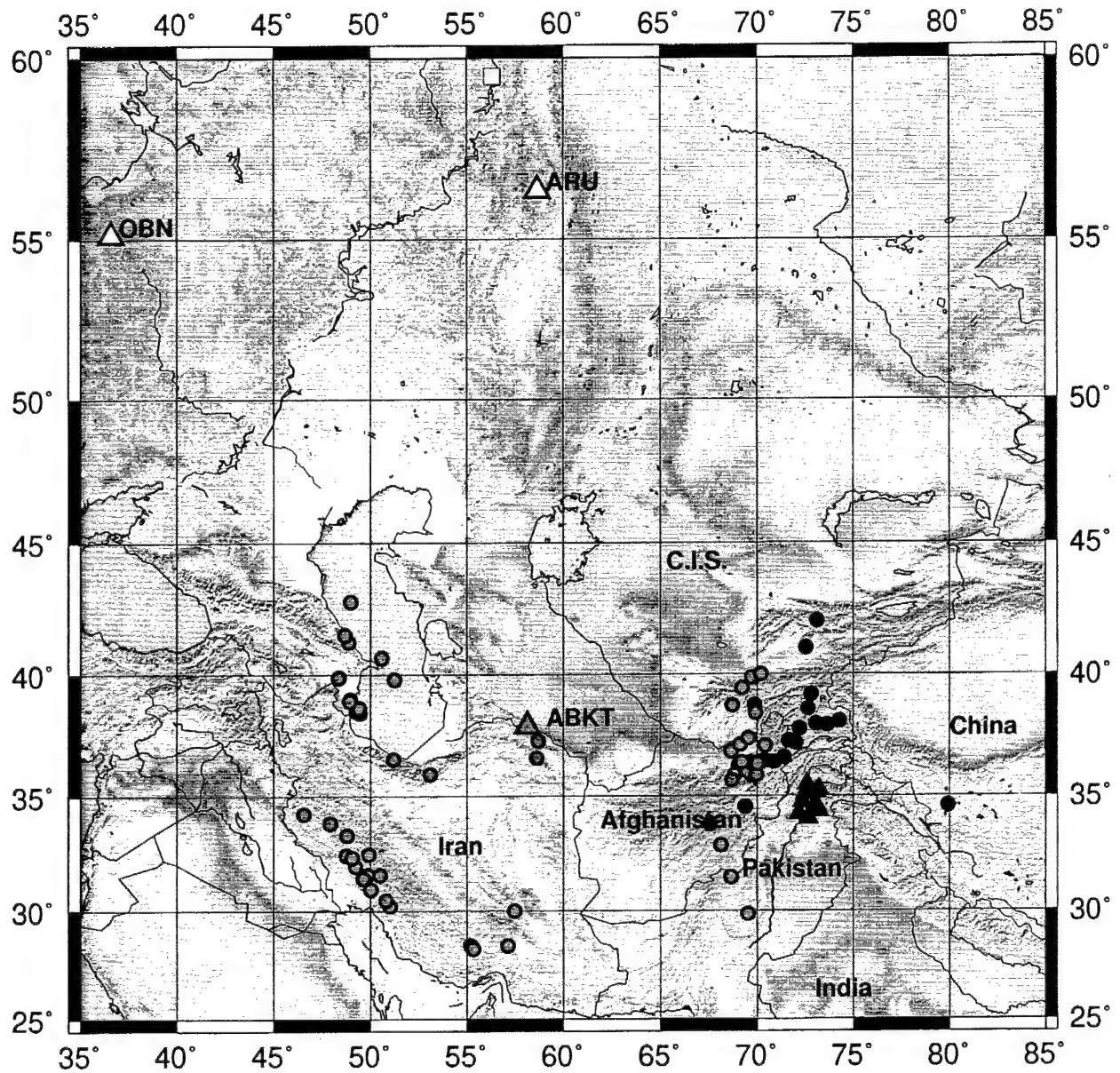


Figure 39. Map of Southwest Asia/Middle East study area showing earthquakes (small circles) analyzed and seismic stations used. Earthquakes are color-coded with the station by which they were recorded. The Ural mine collapse (square) is also shown.

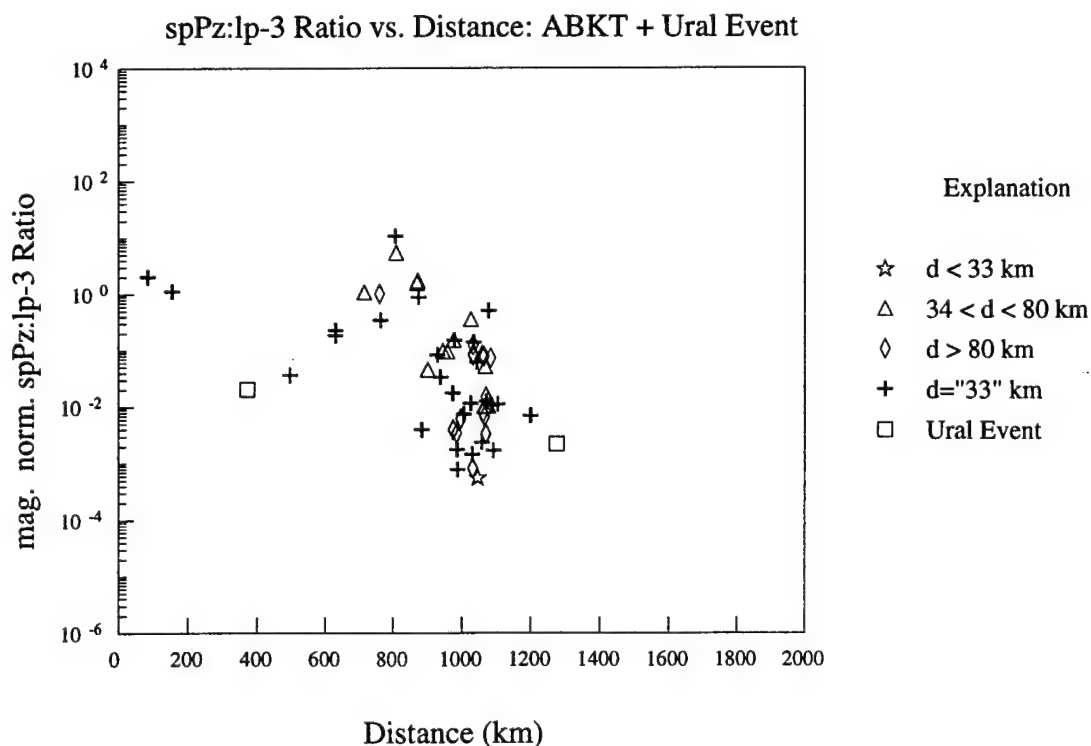
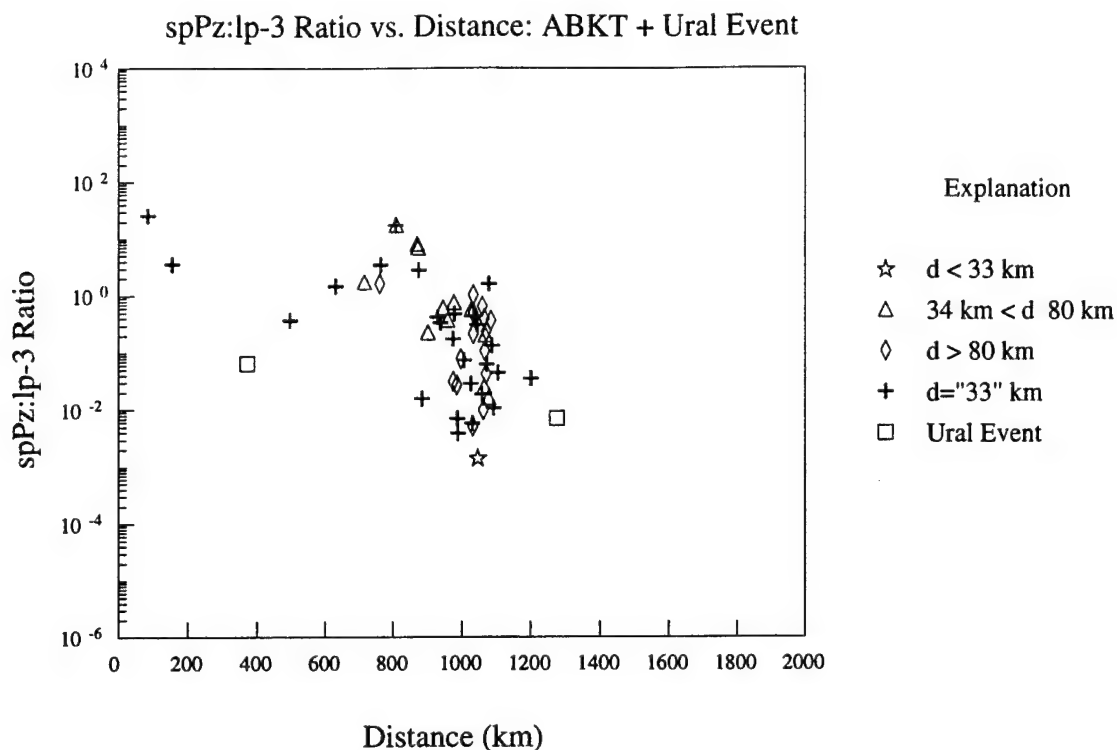


Figure 40. (a) Short-period:long-period energy ratio vs. distance for shallow (stars), intermediate-depth (triangles), and deep (diamonds) earthquakes (stars) recorded by ABKT. Crosses denote earthquakes with PDE depths of 33 km. Included is the Ural mine collapse (squares) recorded at ARU and OBN (See figure 39). (b) Magnitude-normalized short-period:long-period energy ratio vs. distance for the same data.

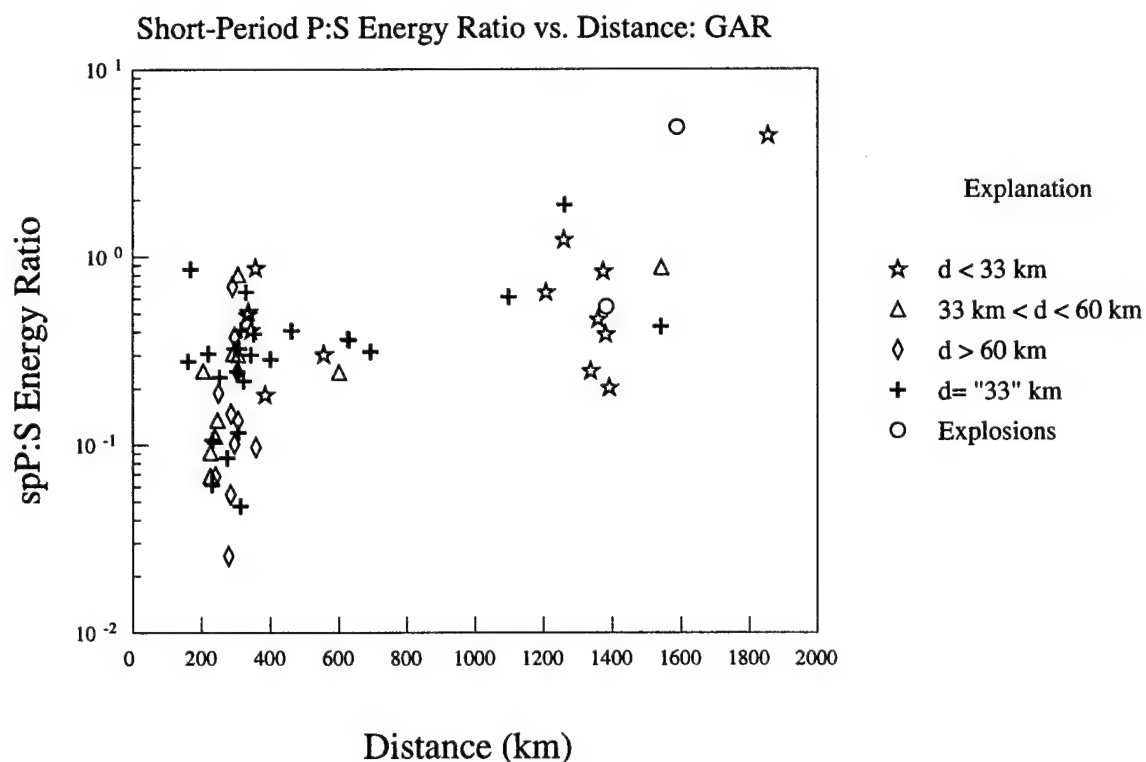
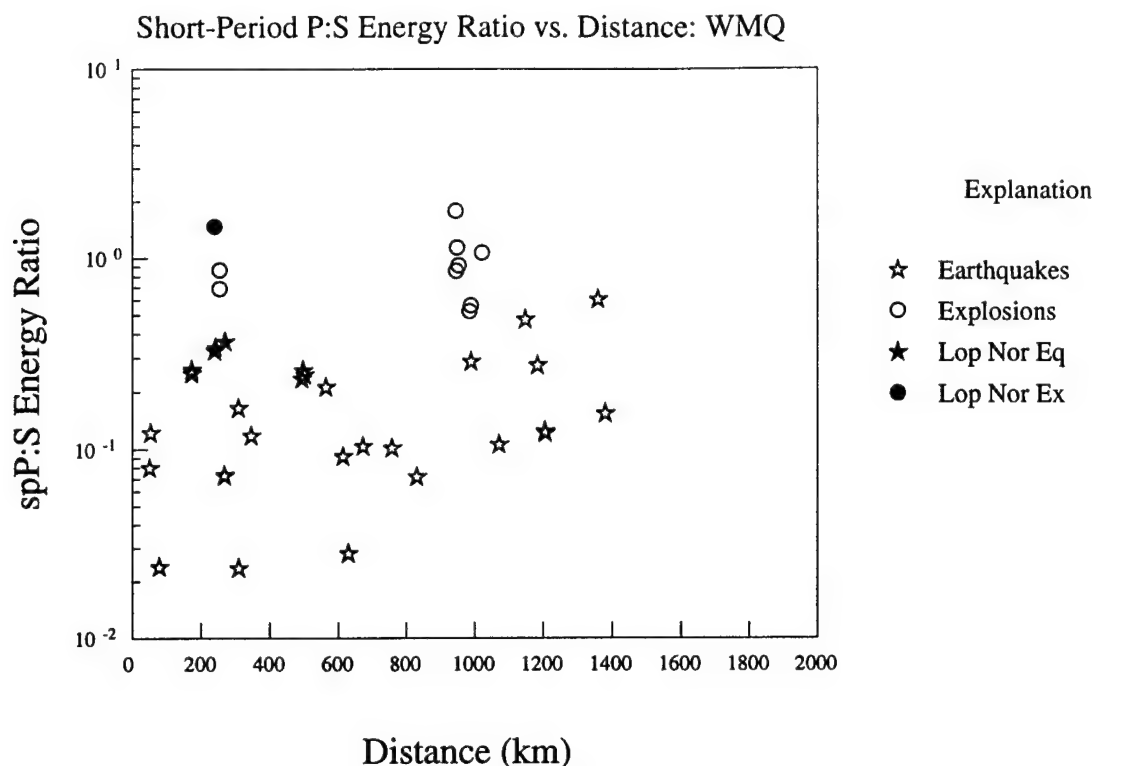


Figure 41. (a) Short-period P:S energy ratio vs. distance for earthquakes (stars) and explosions (circles) recorded by WMQ, as well as the JVE recorded by BAY and KKL. (b) Short-period P:S energy ratio vs. distance for shallow (stars), intermediate-depth (triangles), and deep (diamonds) earthquakes, and explosions (circles) recorded by GAR. Crosses denote earthquakes with PDE depths of 33 km.

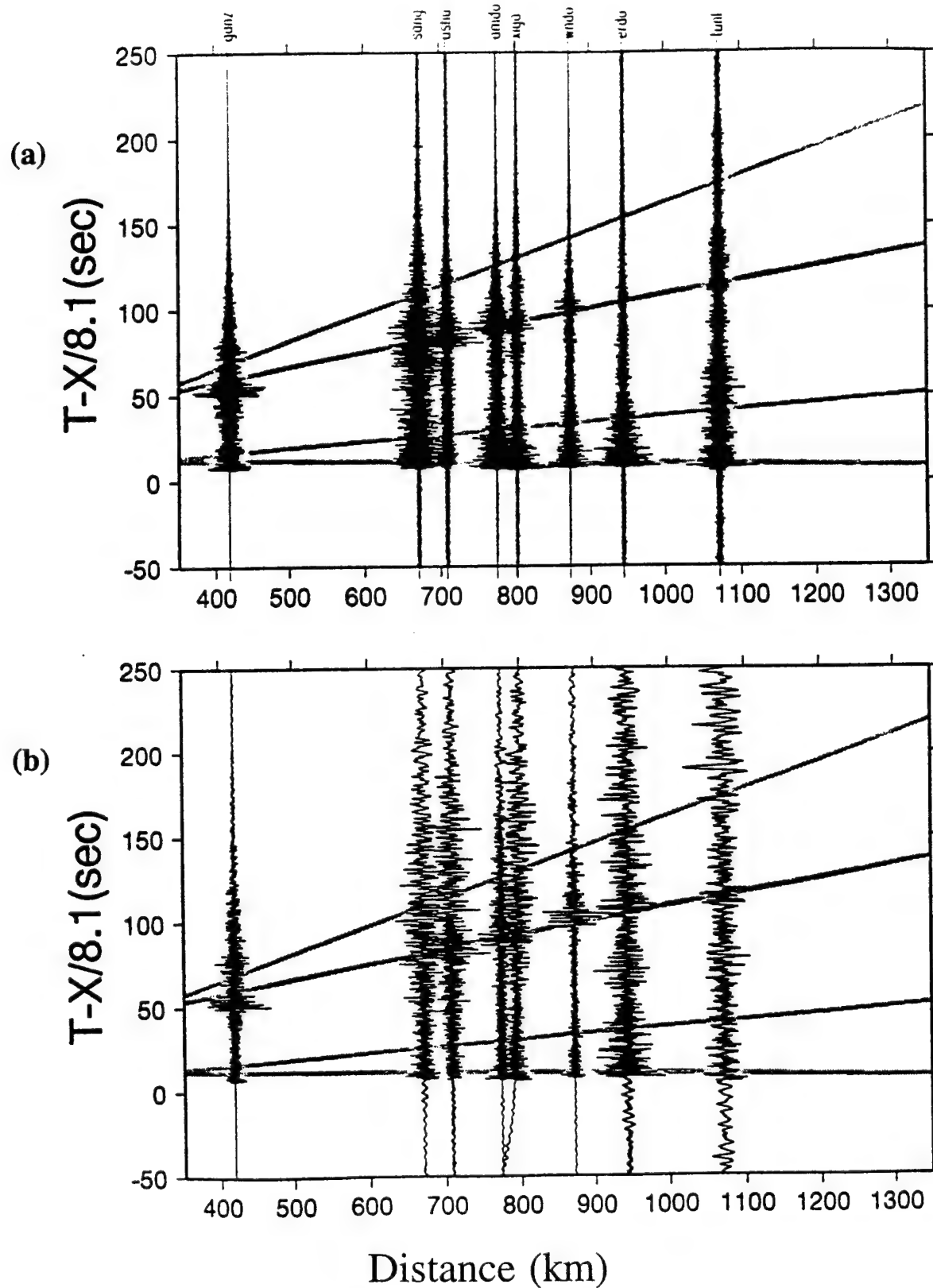


Figure 42. High-pass (a), and broadband, (b) velocity record-sections of a regional earthquake crossing the Tibetan PASCAL Array from the Northeast.

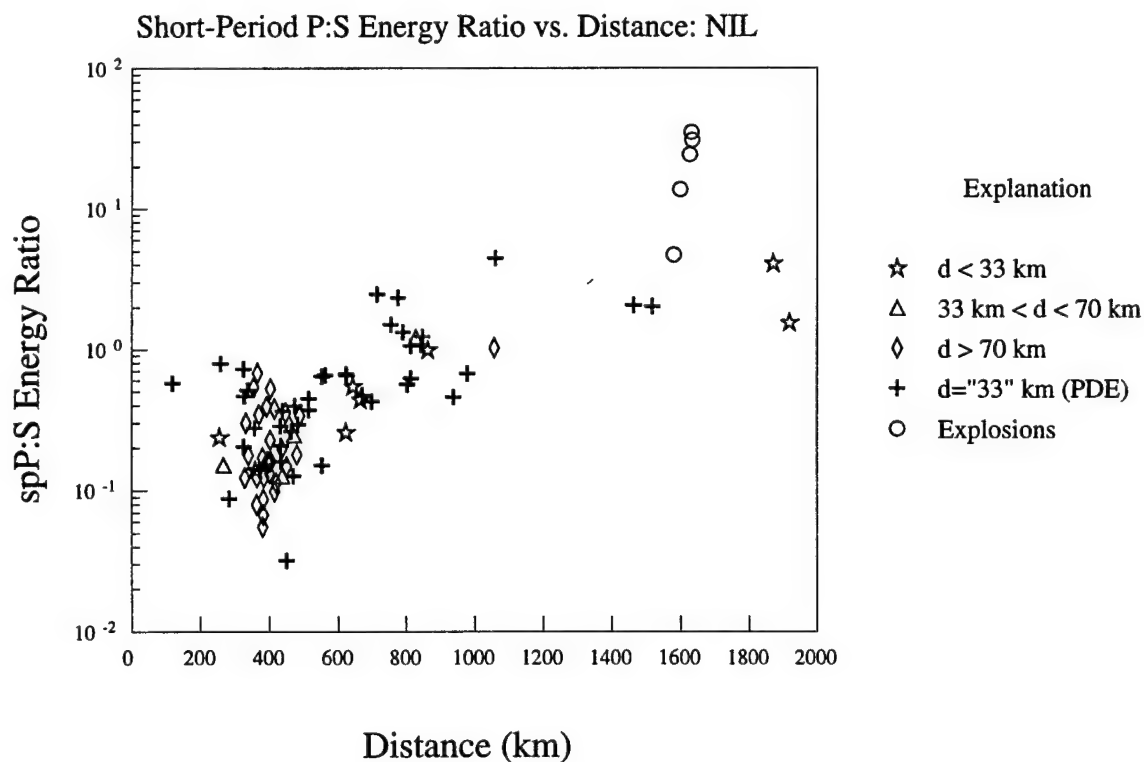
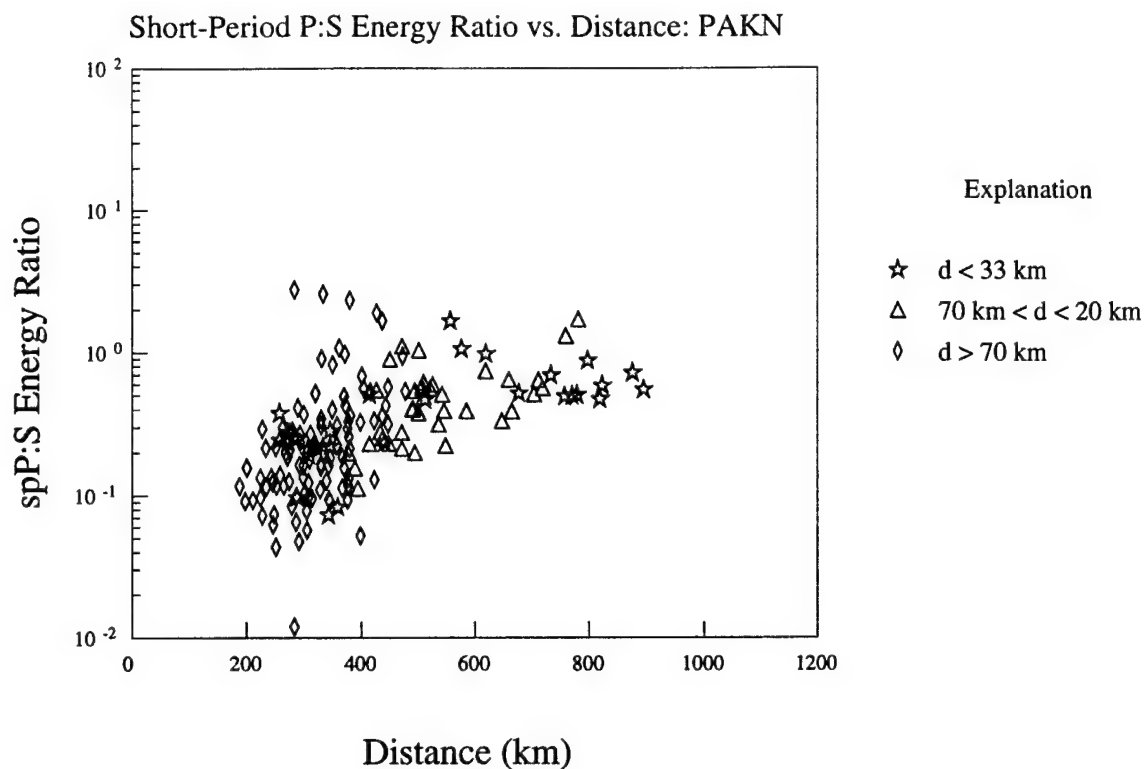


Figure 43. (a) Short-period P:S energy ratio vs. distance for shallow (stars), intermediate-depth (triangles), and deep (diamonds) earthquakes, recorded by the PAKN Array. (b) Short-period P:S energy ratio vs. distance for shallow (stars), intermediate-depth (triangles), and deep (diamonds) earthquakes, and explosions (circles) recorded by NIL. Crosses denote earthquakes with PDE depths of 33 km.

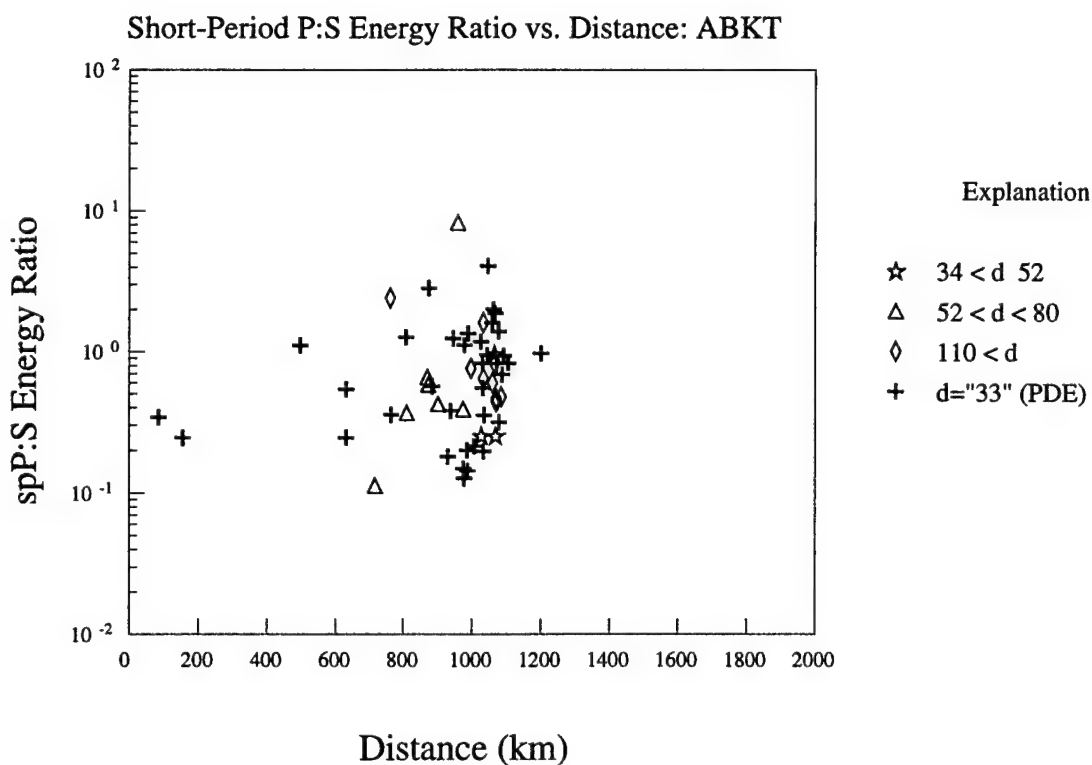
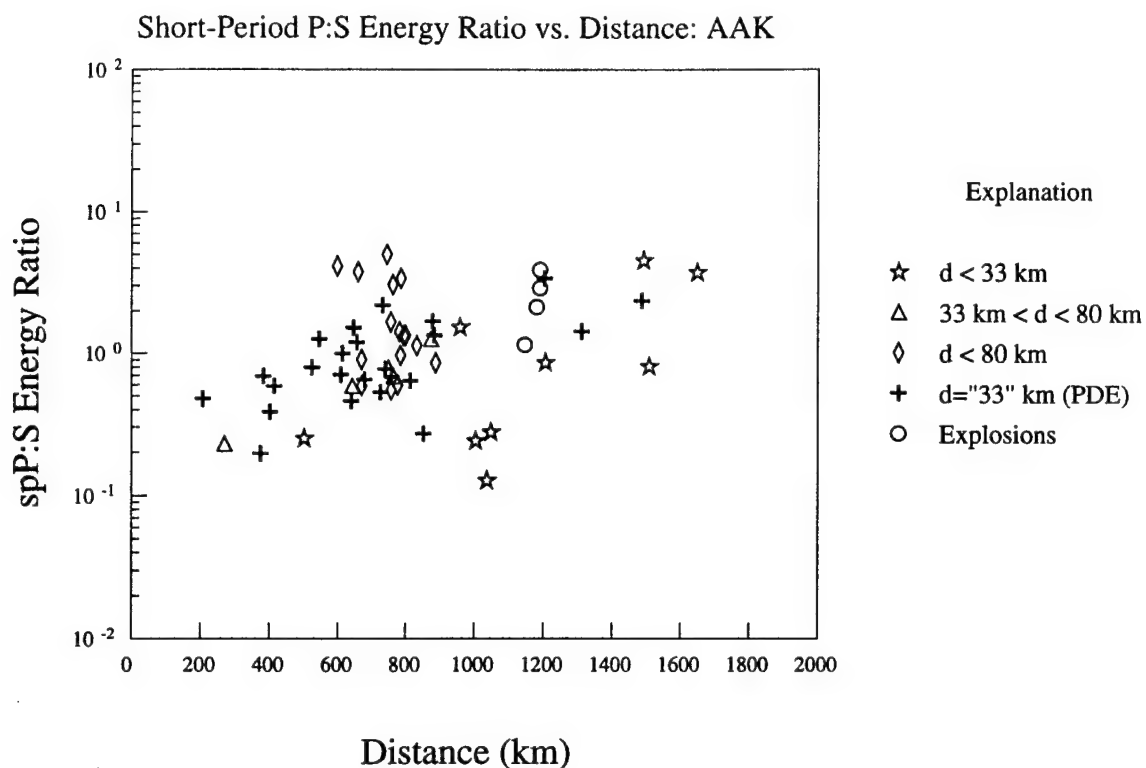


Figure 44. (a) Short-period P:S energy ratio vs. distance for shallow (stars), intermediate-depth (triangles), and deep (diamonds) earthquakes, and explosions (circles) recorded by AAK. Crosses denote earthquakes with PDE depths of 33 km. (b) Analogous plot for station ABKT.

m_b vs. $\text{Log} (M_0)$: Central and Southwestern Asia

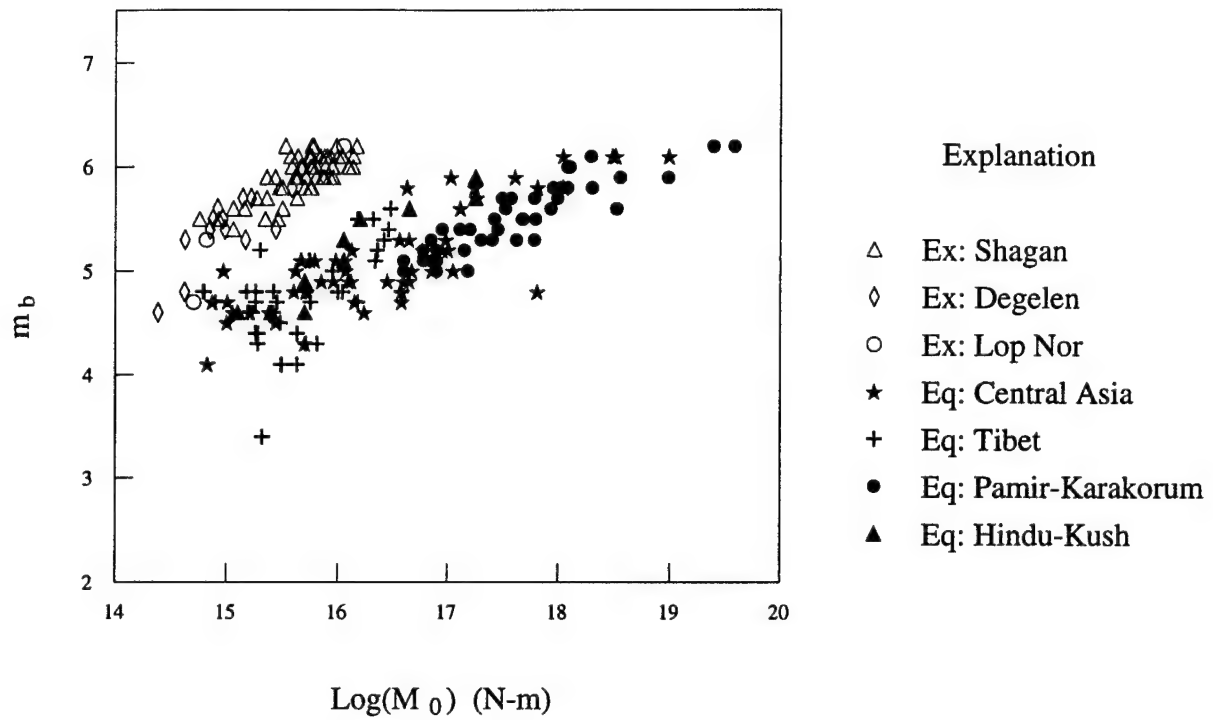


Figure 45. M_L vs. M_0 for Eurasian events.

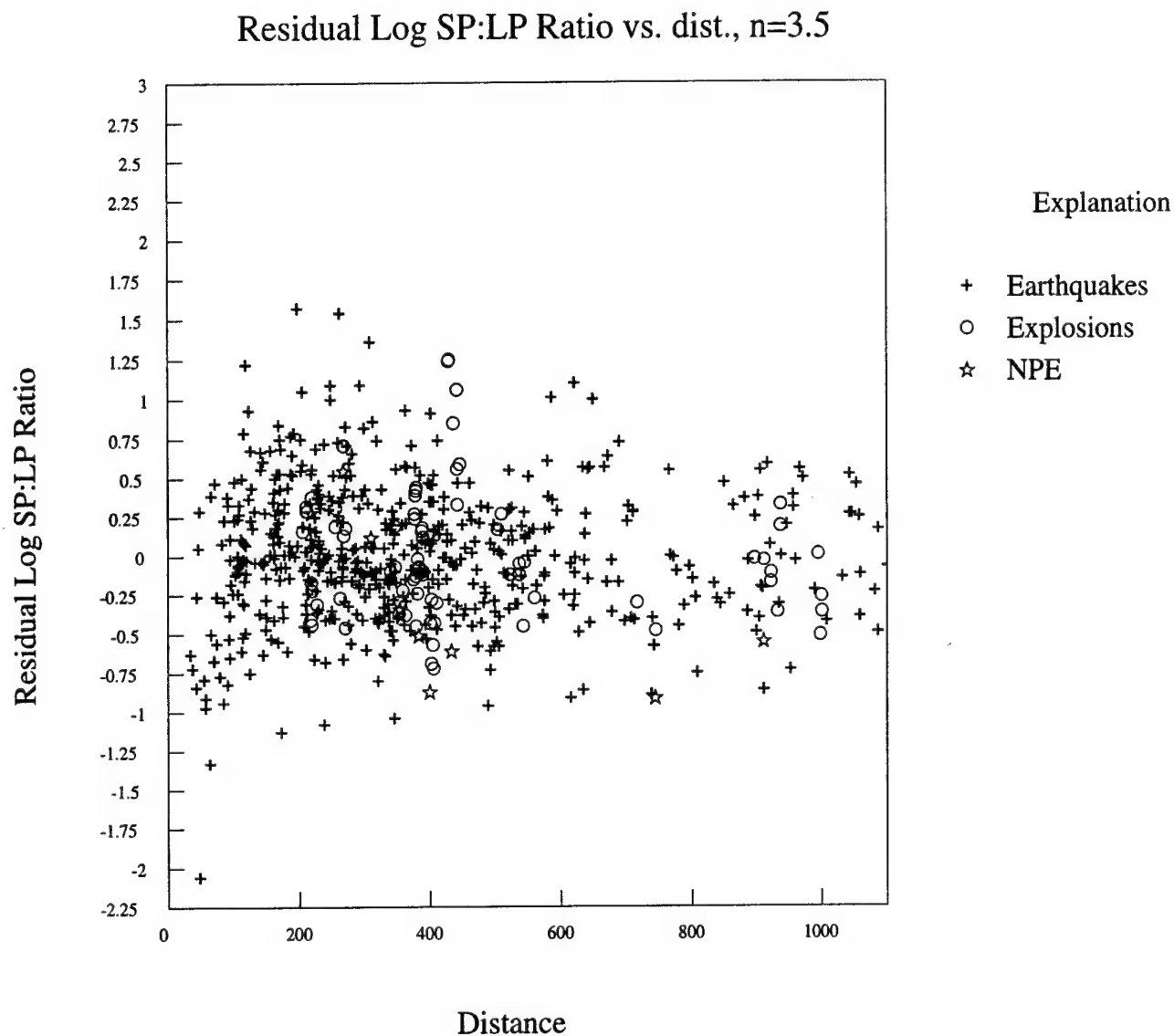


Figure 46. Residual distance-corrected ($n = 3.5$), short-period:long-period energy ratio vs. distance for all multiply recorded events; crosses represent earthquakes, circles are nuclear explosions, and stars denote the NPE.

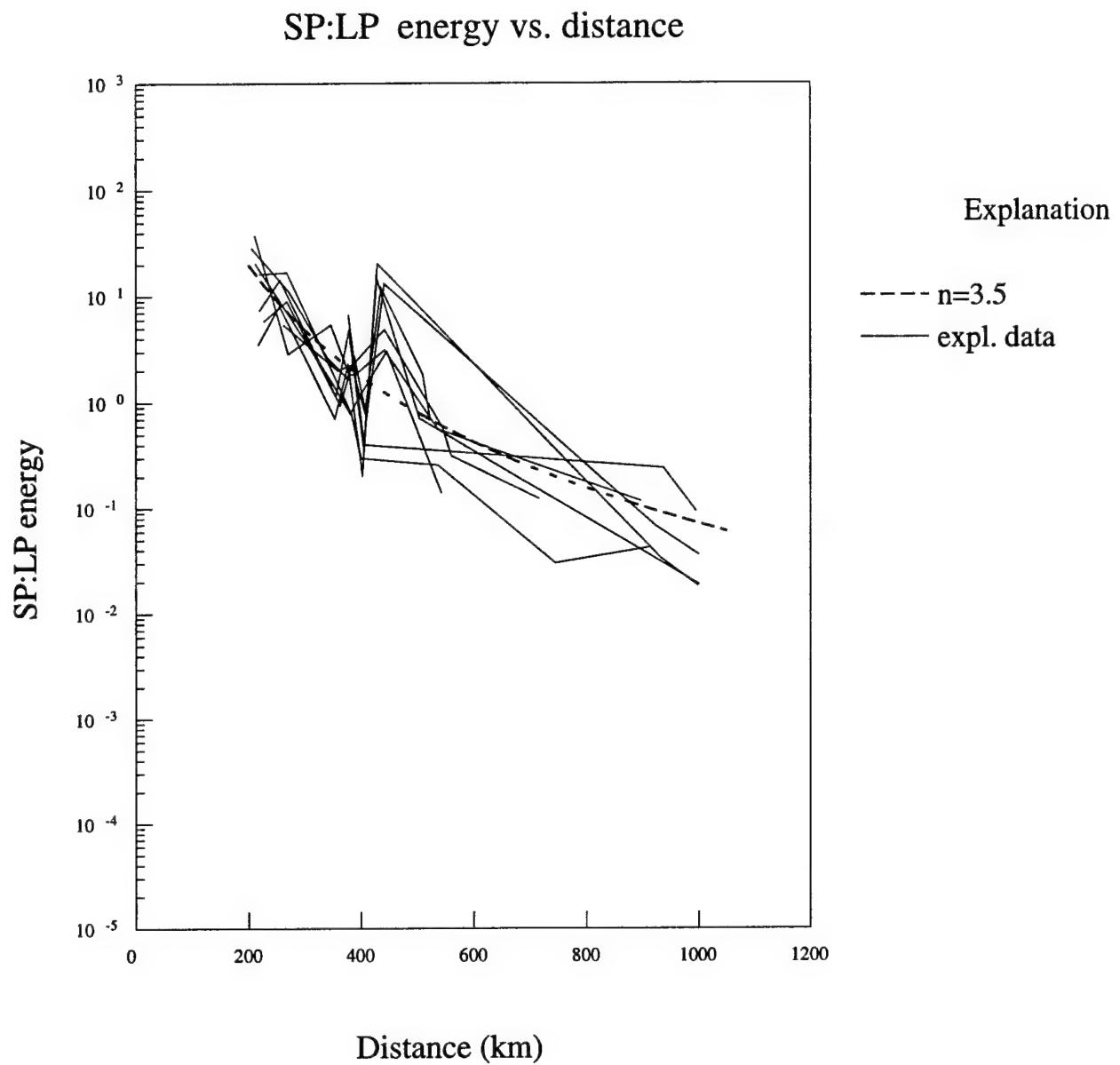


Figure 47. Distance-corrected ($n = 3.5$), short-period:long-period energy ratio vs. distance for explosion data (solid lines) and for synthetic curve $n = 3.5$ (dashed line).

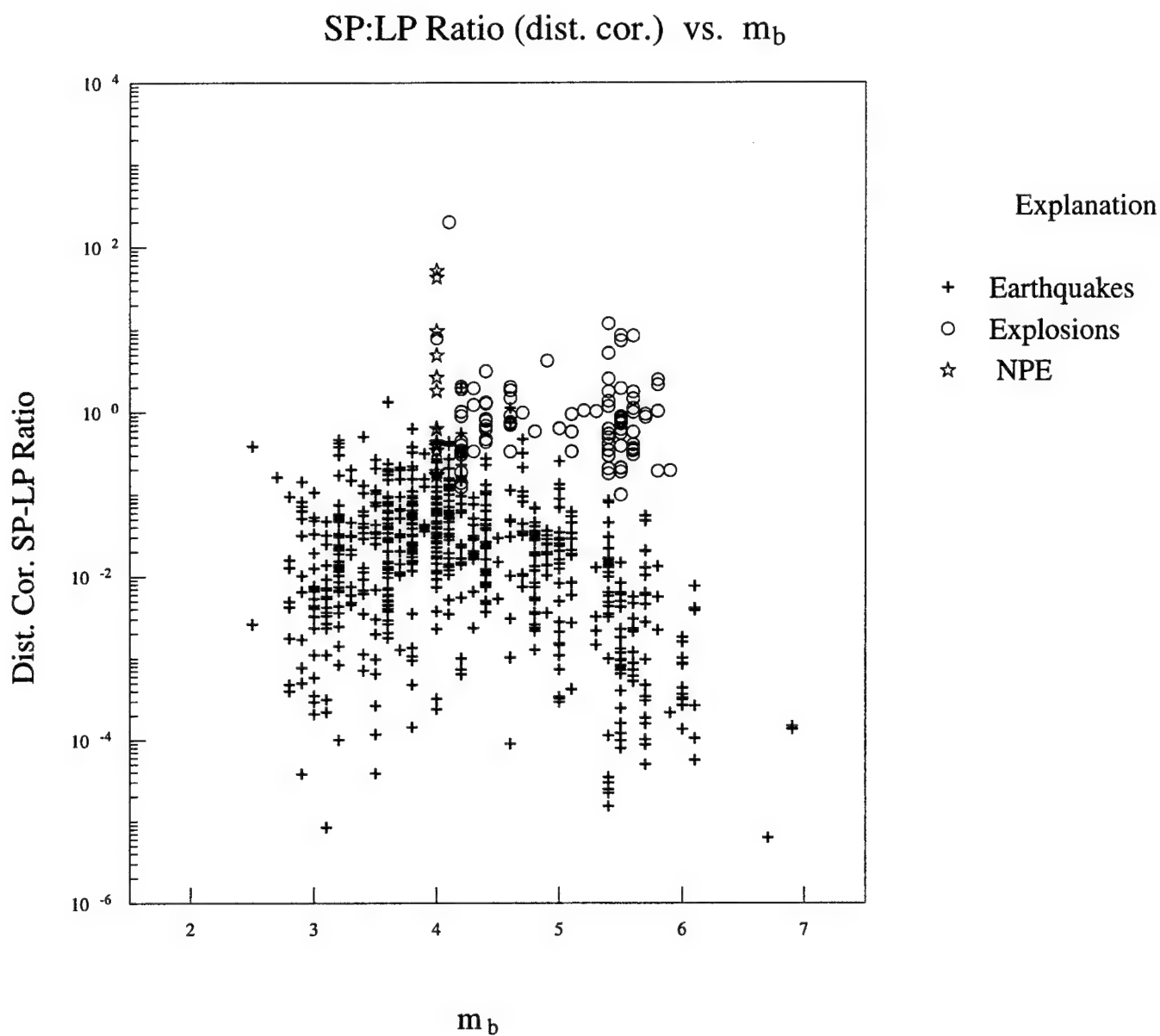


Figure 48. Plot of the short-period:long-period energy ratio (SP:LP) vs. magnitude for TERRAscope data. The values have been distance corrected. Each datum point represents one source-receiver pair.

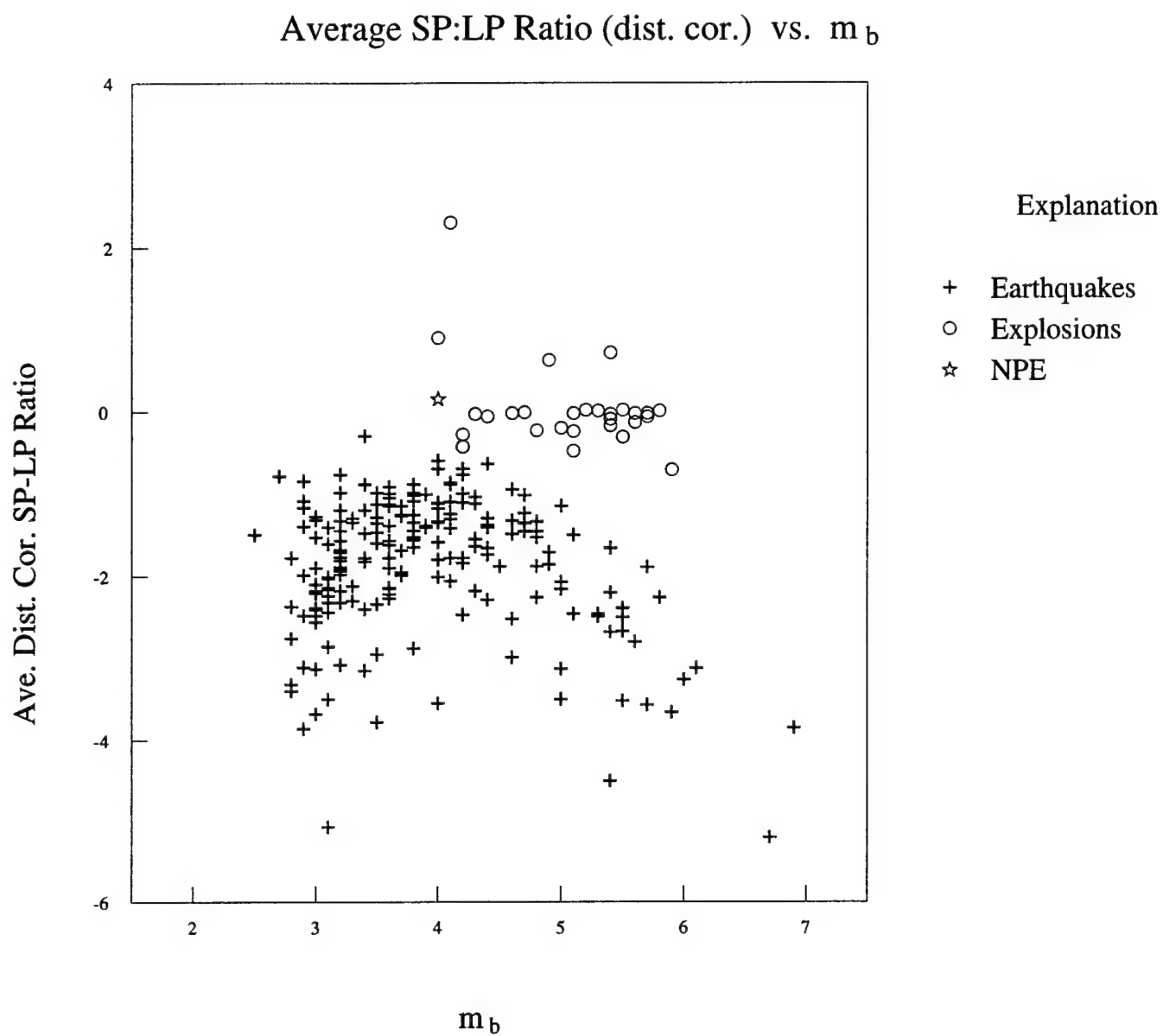


Figure 49. Plot of network-averaged, distance corrected, SP:LP energy ratio vs. magnitude for TERRAScope data.

SP:LP Ratio (dist. cor.) vs. m_b , WMQ

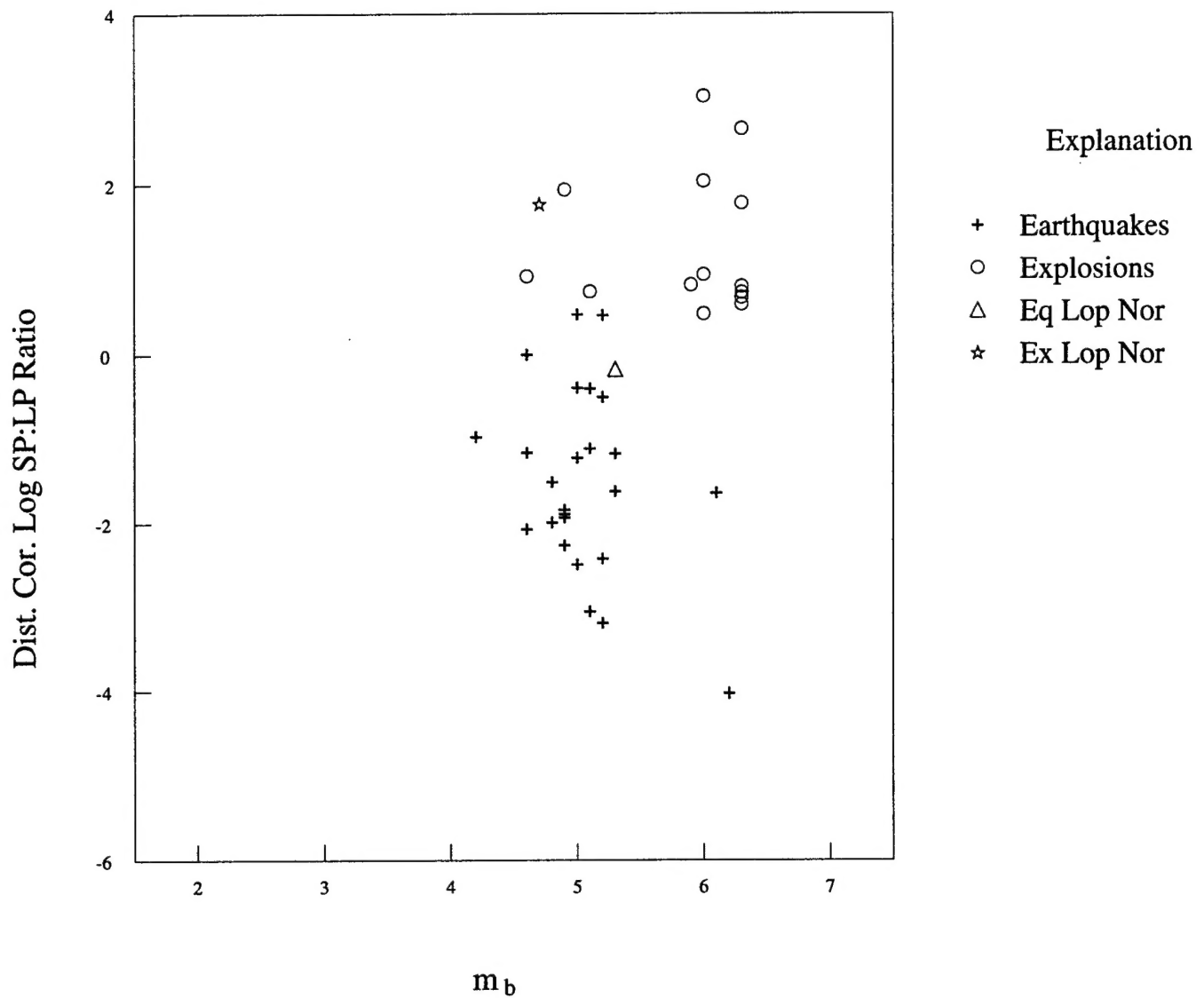


Figure 50. Plot of the short-period:long-period energy ratio (SP:LP) vs. magnitude for WMQ. The values have been distance corrected. Each datum point represents one source-receiver pair.

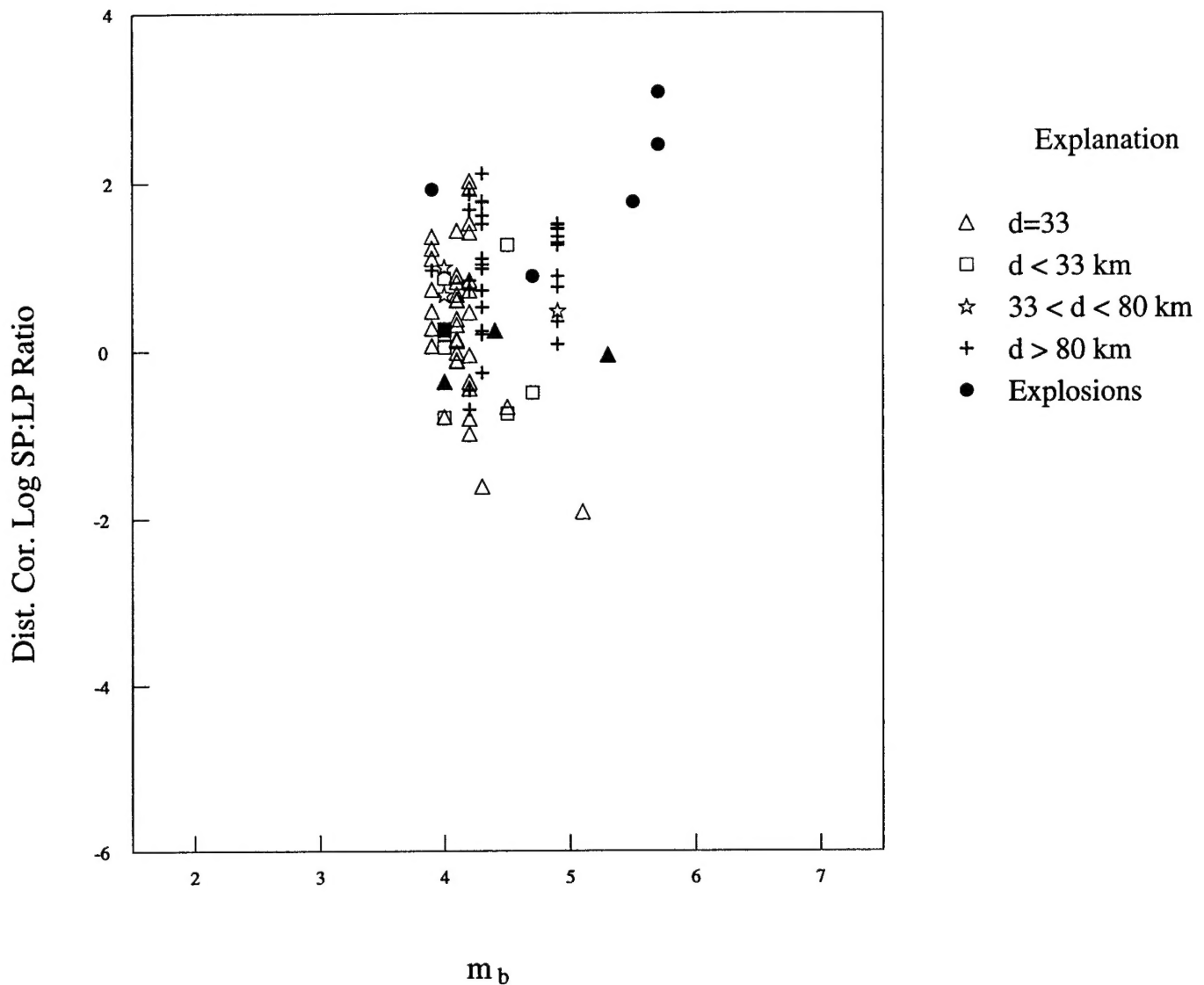
SP:LP Ratio (dist. cor.) vs. m_b , NIL

Figure 51. Plot of the short-period:long-period energy ratio (SP:LP) vs. magnitude for NIL. The values have been distance corrected. Each datum point represents one source-receiver pair. Earthquakes have been sorted by depth. The filled symbols, earthquakes and explosions, represent distant sources near Lop Nor.

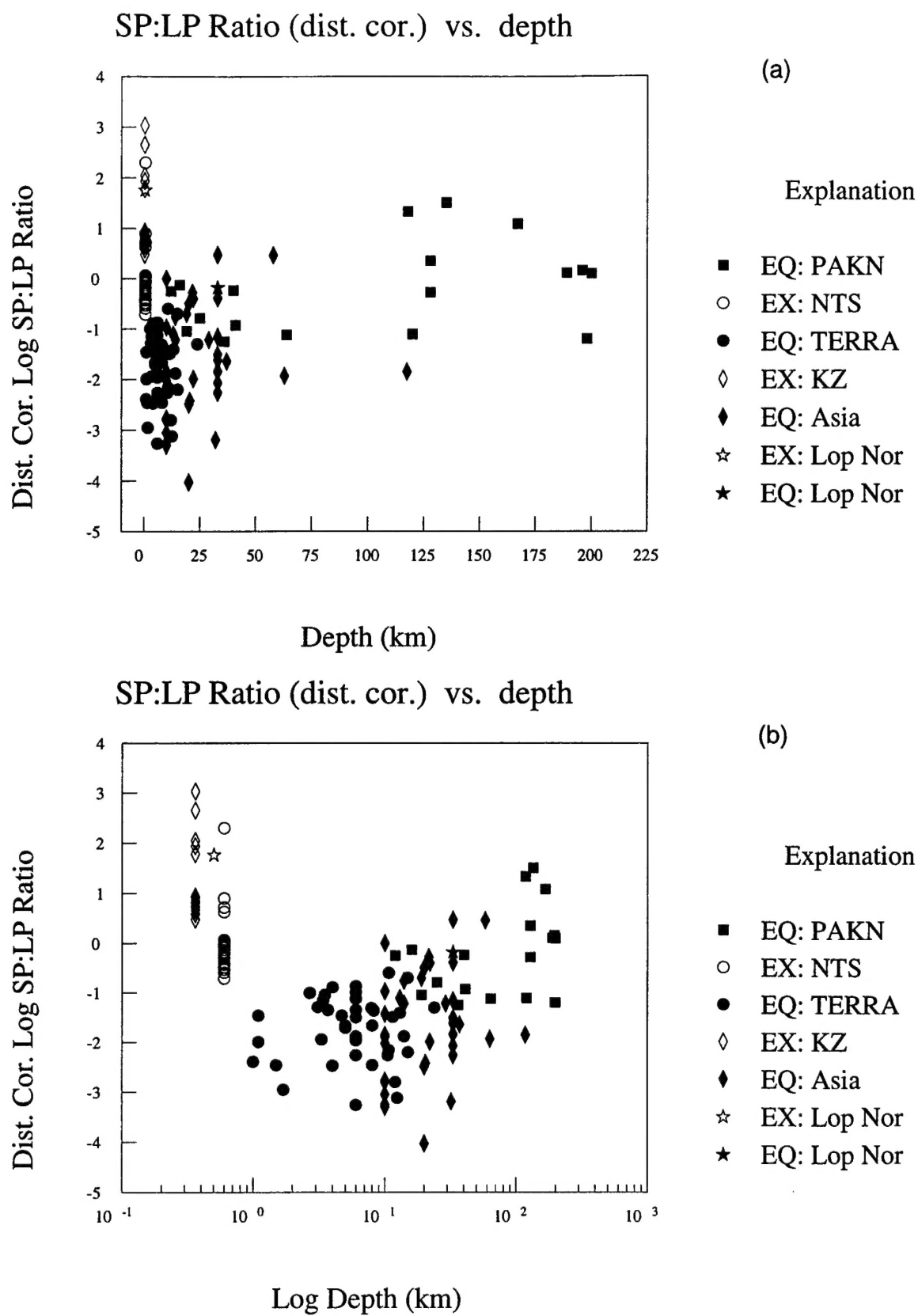


Figure 52. Distance-corrected, network-averaged SP:LP Ratio vs. linear (a) and log (b) depth.

Comparison of Vertical Seismograms from Lop Nor, CIS and NTS Test Sites

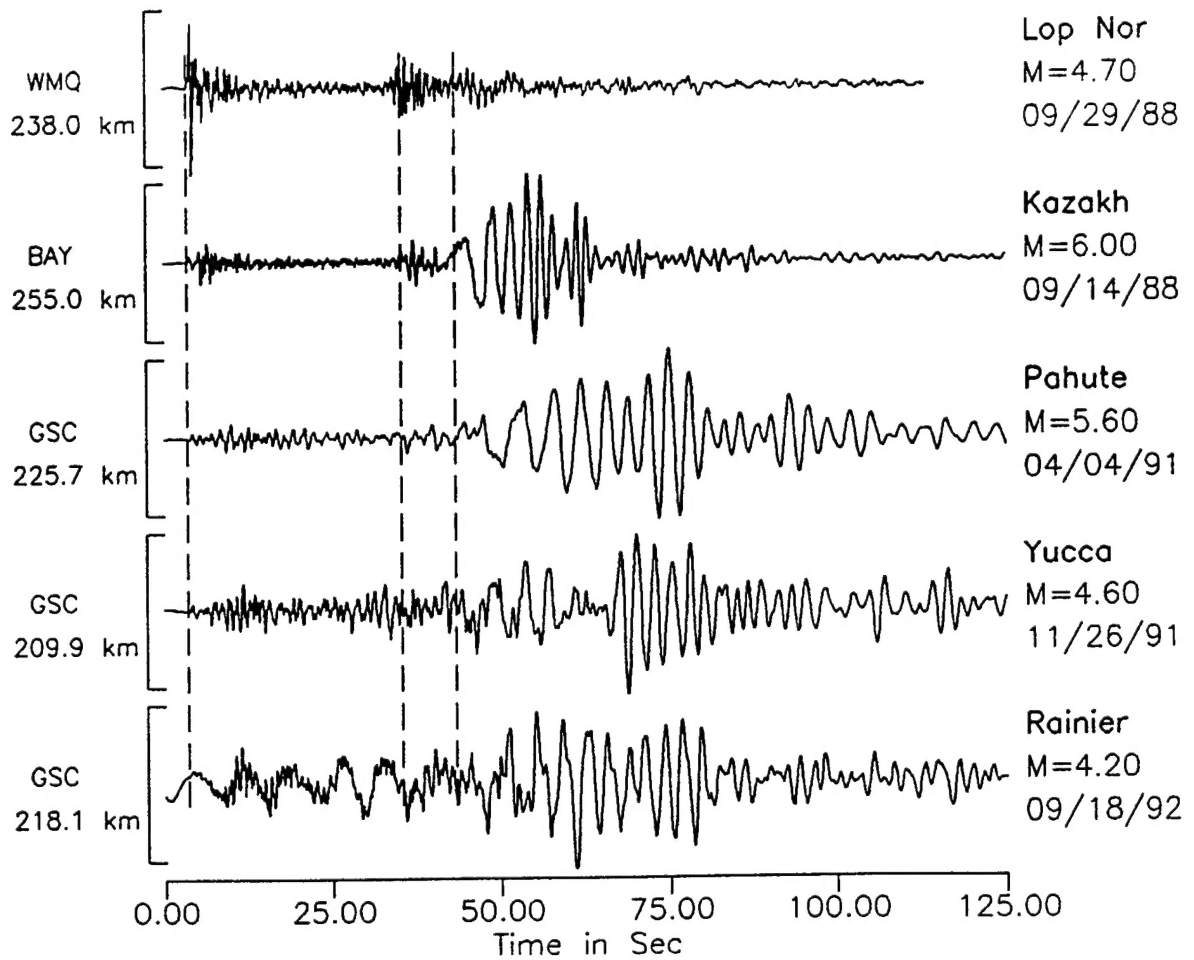


Figure 53. Displacement waveform variation between the various nuclear test sites. The seismograms are aligned according to the onset arrival marked by the first dotted line. The second dotted line shows arrival of pSmS followed by the Rayleigh waves.